BIO-INSPIRED FRACTAL ELECTRODES INTERFACING WITH RETINAL CELLS

by

SABA MOSLEHI

A DISSERTATION

Presented to the Department of Physics
and the Graduate School of the University of Oregon
in partial fulfillment of the requirements
for the degree of
Doctor of Philosophy

March 2020

DISSERTATION APPROVAL PAGE

Student: Saba Moslehi

Title: Bio-inspired Fractal Electrodes Interfacing with Retinal Cells

This dissertation has been accepted and approved in partial fulfillment of the requirements for the Doctor of Philosophy degree in the Department of Physics by:

Dr. Benjamín Alemán	Chairperson
Dr. Richard Taylor	Advisor
Dr. Benjamin McMorran	Core Member
Dr. Cristopher Neill	Institutional Representative

and

Kate Mondloch	Interim Vice Provost and Dean of the Graduate School

Original approval signatures are on file with the University of Oregon Graduate School.

Degree awarded March 2020

DISSERTATION ABSTRACT

Saba Moslehi

Doctor of Philosophy

Department of Physics

March 2020

Title: Bio-Inspired Fractal Electrodes Interfacing with Retinal Cells

Neurostimulation implantable devices are used extensively in treating a variety of neurodegenerative conditions such as Parkinson's, Alzheimer's and age-related macular degeneration. Current devices fail to provide high enough resolutions due to the lack of understanding of the neuron-implant interface connections and fundamental structural and mechanical differences between the electrodes' material and geometry to those of the targeted tissue. These differences trigger the immune responses of the nervous system that engulf the implant and push away the targeted neurons from the electrodes' surface, therefore causing a further drop in the resolution of the device. As long as this issue is unresolved, other approaches for increasing the resolution, such as providing smaller electrode sizes combined with materials with enhanced electrical stimulation/recording properties are not sufficient. In this thesis, an excellent electrode material candidate combined with geometric patterning approach is tested to guide the immune response against the implant into regions away from the surface of the electrodes as well as enhance neuronal adhesion and outgrowth on the electrodes' surface. First, by introducing a simple Euclidean geometry of rows of vertically aligned carbon nanotube forests separated by rows of silicon, fundamental behavioral trends of retinal neurons and glial cells in encountering two materials with substantial mechanical and topographical differences in neighboring regions are studied. It is shown that the immune response of the glial cells and adhesion and outgrowth of neurons can be controlled and guided by changing the roughness and stiffness of the electrode material vs the substrate. Next, by adopting fractal electrode geometries while using the same materials, it is shown that the driven responses of neurons and glial cells can further be enhanced through fine tuning fractal characteristics of the electrode's geometry. Furthermore, preliminary results from future work on comparison between fractal and several Euclidean geometries are discussed. By adopting the appropriate materials patterned in an optimal geometry, the immune response of the nervous system towards implants can be controlled and guided to reduce the distance between the implant's electrodes surface and targeted tissue and hence increase the resolution.

CURRICULUM VITAE

NAME OF AUTHOR: Saba Moslehi

GRADUATE AND UNDERGRADUATE SCHOOLS ATTENDED:

University of Oregon, Eugene
University of Tehran, Tehran, Iran
Shahid Beheshti University, Tehran, Iran

DEGREES AWARDED:

Doctor of Philosophy, Physics, 2020, University of Oregon
Master of Science, Atomic and Molecular Physics, 2009, University of Tehran,
Bachelor of Science, Physics, 2004, Shahid Beheshti University

AREAS OF SPECIAL INTEREST:

Neural-electrode interfaces
Fractal analysis of neural networks
Retinal implants

PROFESSIONAL EXPERIENCE:

Graduate Research Assistant

Graduate Teaching Assistant

GRANTS, AWARDS, AND HONORS:

Miller Family Graduate Award in Technology & Science, College of Arts and Sciences, University of Oregon, 2016

Weiser Sr Teaching Assistant Award, Department of Physics, University of Oregon, 2015

PUBLICATIONS:

Watterson, W. J., Moslehi, S., Smith, J. H., Montgomery, R. D. and Taylor, R. P. “Fractal Electronics as a Generic Interface to Neurons.” In: The Fractal Geometry of the Brain. Springer. (2016)

Smith, J., Rowland, C., Moslehi, S., Taylor, R., Lesjak, A., Lesjak, M., Stadlober, S., Lee, L., Dettmar, J., Page, M. and Himes, J. Relaxing Floors: Fractal Fluency in the Built Environment. Nonlinear dynamics, psychology, and life sciences. 24 (2020): 127-141.

Smith, J.H., Rowland, C., Harland, B., Moslehi, S., Montgomery, R.D., Schobert, K., Watterson, W.J., Dalrymple-Alford, J. and Taylor, R.P. How Neurons Exploit Fractal Geometry to Maximize Physical Connectivity. (2020) In publication.

ACKNOWLEDGMENTS

Every person's path in life is shaped by the decisions they make and people they have or meet through the course of their lives. I wouldn't have been here if it were not for the unconditional love, full support and the sacrifices of my parents, Sedigheh and Mohammad Hasan Moslehi. From the day you bought me a series of books about the universe when I was ten, to the day I told you that I wanted to move across the world to follow my passion, through the ups and downs of living a life far away from home, you have always been there for me. To my brother, Salim, my sister, Nasim and my sister in law Maryam, thank you for believing in me.

I would like to express my sincere gratitude to my advisor, Dr Richard Taylor for providing me with the opportunity for working on this research. Your mentorship, full support and understanding was most valuable through the years. I'd also like to thank Drs. Maria-Thereza Perez, Benjamín Alemán, Cris Neill and Ben McMorran. Dr. Maria-Thereza Perez, you taught me how to look at and analyze a biological system. Dr. Benjamín Alemán, your guidance and advise to help forming the questions behind this research is much appreciated. Drs. Cris Neill and Ben McMorran, thank you for the most helpful and illuminating discussions.

I'd like to thank my senior and current labmates and friends. Bill Watterson, Rick Montgomery and Ian Pilgrim, you welcomed me to the Taylor group. You taught and equipped me with the tools I needed to move forward in my scientific path. Julian Smith, Conor Rowland and Kara Zappitelli, we were an incredible team, working together so hard to take this project one step ahead at a time. I’ve enjoyed every step of the way developing personal and professional relations with you all and can’t wait to hear about your accomplishments in your careers and in life.

The research in this thesis was funded by W M Keck foundation.

TABLE OF CONTENTS

Chapter Page

LIST OF FIGURES

Figure Page

Figure Page

LIST OF TABLES

Table Page

CHAPTER I

INTRODUCTION

Worldwide, millions of people are affected by neurodegenerative disorders such as Alzheimer’s, Parkinson’s, motor neuron diseases, age-related macular degeneration and many more conditions. Neurodegenerative disorders are the second cause of death after heart diseases and the leading cause of disability.[1] Global statistics show that 50 million people have Alzheimer’s or some form of dementia[2], with an estimated 5.8 million of those living in the US.[3] More that 10 million people worldwide are living with Parkinson’s disease.[4] Add to these statistics the staggering number of people affected by some form of limb loss - more than 1 million annual amputations globally.[5] The emotional and financial costs and the global rise in the number of people affected by these conditions calls for more definitive solutions. Neurostimulation devices using both invasive (in the case of an implant) or noninvasive (a prosthetic device) approaches are frequently employed to induce therapeutic neuromodulation responses in neurons to restore natural nerve functions in the damaged tissue. The global market size of neurostimulation devices was $4.99 million in 2018 and is estimated to increase with a compound annual growth rate (CAGR) of about 12.5% by 2026.[6]

Retinitis pigmentosa and age-related macular degeneration are two of the neurodegenerative conditions that gradually cause vision loss in patients affected by them. This type of vision loss can potentially be treated with retinal implants, a sub-category of invasive neurostimulation devices. The global market size of retinal implant devices was $30 million in 2017 and expected an increasing CAGR of 10.6% by 2026.[7]

Generally speaking, implantable neurostimulation devices suffer from shortcomings due to a number of reasons. As an example, current retinal implants do not restore vision to a resolution high enough for functioning in daily life. The most basic problem is that they are rigid foreign objects inserted into the nervous system triggering an immune response in the form of a thick layer of glial cells engulfing the implant. This layer increases the distance between the implant's electrodes and targeted neurons and therefore hinders the stimulating power of the implant. The question addressed in this thesis is: 'How can the gliotic response be controlled and guided such that the connection between the electrode surface in the implant and neurons be improved? The proposed solution is to adopt an appropriate material and geometry system that would potentially trigger and enhance different reactions from various cell types.

Before diving into discussing the results, certain background information will provide a more insightful understanding of the nature of the existing problems and the solutions offered. With the focus being on retinal implants, a review of retinal degenerative conditions potentially treatable by implants, implant types, their existing commercial devices and prototypes is given. Next, different retinal cells and their roles in the retina are reviewed. The reactive gliosis problem that current devices face, the potential solutions tested and reasons that they fail are discussed. The discussion of proper electrode material properties is followed by a brief review of carbon nanotubes (CNTs) as one of the best candidates for an electrode material along with their unique properties. Fractal geometries are then defined and their potential role in improving the neuron-electrode interface is discussed. Finally, the proposed system of combined material and geometry to improve connectivity and overall performance of the implants is offered.

1-1. Age-Related Macular Degeneration (AMD) and Retinitis Pigmentosa (RP)

AMD is a neurodegenerative disorder that causes gradual loss of photoreceptors in the macula. The macula is the central region of the retina with a high density of photoreceptors that is responsible for central vision. Patients affected by AMD, start losing central vision at early stages of the condition. However, in the majority of the cases, peripheral (side) vison is still intact. AMD is the most common cause of vision loss in people above 60 years old. Two general types of the disease are dry and wet AMD. Dry AMD is the common form affecting 90% of the patients. In this type, parts of the retina will get thinner and allow the diffusion of extracellular proteins into retinal layers. But vision is not lost until the very late stages of the condition. Wet AMD is the more severe form of the disease causing 90% of the legal blindness cases (visual acuity (VA) worse than 20/200) by any form of AMD and is caused by growth of blood vessels into the retinal layers. Currently no treatment exists for advanced dry AMD. The prevalence of AMD is approximately 2.1% of the population. In the US only, about 11 million people have some form of AMD. This number is expected to double by 2050. In 2020, it is estimated that 196 million people worldwide will be affected by the disease.[8,9]

RP refers to a group of genetically inherited diseases that can affect more than 100 different genes related to various retinal functions. Photoreceptors in the outer regions of the retina die predominantly causing loss of peripheral vision especially in low luminescence environments. RP patients have tunnel vision through most of the stages of the condition which progresses into complete blindness in the end. RP is the most common inherited retinal disease affecting ~ 1 in 4000 people.[10]

Existing therapies such as anti-angiogenic drugs[11], laser therapy, photodynamic laser therapy (PTD) (all for wet AMD), and certain vitamins for RP fail to completely treat these conditions. These treatments delay the vision loss through slowing the progression of the disease. Because of the high number of gene mutations causing RP, gene therapy is not considered the best treatment approach.

Lack of effective treatments makes retinal implants an ideal approach especially for dry AMD and RP. Figure 1-1 compares normal vision to typical AMD and RP visions.

Healthy Vision **AMD** **RP**

Figure 1-1. Examples of healthy vision versus AMD and RP (tunnel vision). On the left, normal vision is shown. The middle image shows the peripheral vision of AMD patients and the one to the right indicates the tunnel vision of RP patients at the early to middle stages of the disease.

1-2. Retinal Implants

In RP and AMD, the photoreceptor cells in the back of the retina deteriorate over time and are not able to produce a signal from the incoming light and stimulate the neurons. Retinal implants are an alternative treatment to vision loss caused by these two conditions. The implant consists of an array of metal electrodes that gather the visual information from the surroundings through different means (depending on implant type and placement in the retina) and produce a voltage to stimulate neurons connected to them. Each electrode acts like a pixel. Depending on their positioning with respect to the retina, retinal implants are divided into two groups.

1-2.1. Epiretinal and Subretinal Implants

An epiretinal implant consists of an array of electrodes sitting in front of the retina. It receives signals from an external camera that records images of the surroundings and directly stimulates the ganglion cells according to the pattern recorded. The Argus II epiretinal implant by Second Sight uses such technology. A video camera and an image processing unit are mounted onto a pair of glasses that patients need to wear. The camera takes images, sends them to the processing unit for resolution reduction and conversion into spatial and temporal patterns of stimulating pixels. The patterns are then transferred to the implant to stimulate retinal ganglion cells. These cells then send the signal to the brain through the optic nerve.[12] Epiretinal implants bypass all the functional healthy layers of the retina.

Subretinal implants replace the damaged photoreceptors in the back of the retina and are directly connected to bipolar neurons. Their location with respect to all retinal layers gives them the advantage of using the processing power of the remaining healthy neurons and the full functionality of the neural circuitry instead of relying on an external camera and processor. They consist of an array of micro photodiodes which generate signals directly from the incoming light and transfer them to an array of conducting microelectrodes which then stimulate neurons interfacing with them. This type of implant has a simpler design with the light receiving, processing and stimulation parts all mounted on the same chip. Figure 1-2 shows the position of both implant types with respect to the retina. The inset shows the neuron types that the implants would interact with.

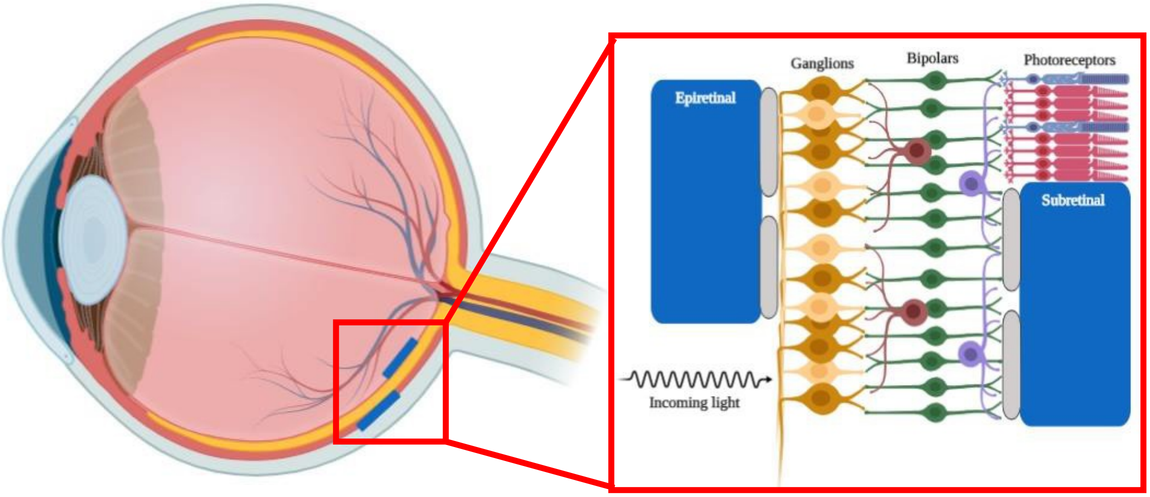

Figure 1-2. Subretinal versus epiretinal implants. Schematic of the eye showing the position of epiretinal and subretinal implants with respect to the retina. The inset is a zoom in of the area, indicating different neuronal layers in the retina. The epiretinal implant is attached to ganglion cells directly and stimulates them. The subretinal implant is in contact with bipolar neurons.

Subretinal implants have some advantages over the epiretinal ones. Since they use the full functionality of the healthy retinal layers, they could potentially provide higher VA since the pattern created by incident light on the microphotodiode array is a direct reflection of the real image and not a low-resolution representation created by a processor. Their simple design of having all units on the implant itself, makes their usage and patients' daily life more convenient since they wouldn't need to wear glasses. They can potentially be powered through the microphotodiodes or wirelessly, therefore no part of the implant would extend out of the eye, keeping it a closed system and reducing chances of infection. In addition, this makes them more compatible with rapid movements of the eye. Epiretinal implants have the advantage of easier insertion and therefore are less risky.[13] Research groups across the world have been working on design and improvement of retinal implants for a few decades now. Table 1-1 is a summary of the groups currently investigating various designs of retinal implants.

1-3. The Retina

The retina is a hierarchical layered structure in the back of the eye and is considered part of the central nervous system (CNS). The light that enters the eye through the lens, passes through all the layers to reach the photoreceptors. The photoreceptors convert the light into an electrical response that stimulates other neurons and is eventually transferred to the brain through the optic nerve.

1-3.1. Retinal Neurons

Neurons are electrical units in the nervous system responsible for communication between different parts of the body. They are highly polarized cells in the sense that there are distinct differences in shape, size, and functionality of different parts within one cell. Their size, shape and connectivity are determined by their functionality. A typical neuron is made of three main morphological parts. The cell body or soma contains the nucleus and is responsible for protein synthesis. Dendrites are branched extensions from the soma and are usually referred to as the dendritic tree. They gather the signals from neighboring neurons via synapses and transfer them to the soma. Accordingly, the dendrites and the soma are the input units of the cell. The axon extends from the soma as a single branch (in most neurons) for much larger distances compared to the dendritic tree. It is the output unit of the cell carrying signals from the soma to the dendrites of other neurons. During neuronal

Device	Research Group	Implant type	Image recording/ processing	Disease	Electrode	Restored VA	FDA /clinical trials
Argus II	Second Sight medical products (US)	Epiretinal	External video camera and processing unit(VPU)	RP and AMD	6 × 10 array of platinum electrodes diameter = 200 µm spacing = 575 µm Individually controlled	~20/1000	FDA & CE Mark (2013) 350 users worldwid[14]
Retina Implant Alpha IMS	Retina Implant AG (Germany)	Subretinal	Internal light-sensitive photodiodes	RP	1500 photodiodes/amplifiers/stimulating TiN electrodes Independent pixels. Electrodes Size = 72 × 72 μm^2. [17]	20/546 (one patient)	CE Mark (2013) 29 patients (2015)[15]
Intelligent Retinal Implant System (IRIS V2)	Pixium Vision (France)	Epiretinal	VPU	RP	49 and 150 electrodes IrOx		10 patients[16]
Prima bionic vision	Pixium Vision (France)	subretinal	VPU	Advanced dry AMD and RP	2 × 2 mm^2 chip 378 Silicon on insulator Electrodes 70 µm pixels, 5 µm trenches Hexagonal electrode [18,19]	Letter recognition	5 patients (2018)[16]
Subretinal Retinal Prosthesis	Boston Retinal Implant Project (US)	Subretinal	VPU	RP and AMD	256 sputtered iron oxide film electrodes independently configurable stimulation channel[20]		Non-human primates
Diamond-based Epiretinal	Bionic Vision Australia	epiretinal			2.4 × 2.4 mm^2 chip 256 diamond electrodes Size = 120 × 120 μm^2, 30 µm trenches[21]		

Table 1-1. Summary of existing retinal implants research groups in the market.

differentiation, axons typically emerge before dendrites. In general, for simplicity, both dendrites and axons are referred to as neuron processes or neurites. Mature neurons can never divide.

There are 5 different types of neurons in the retina. Photoreceptors reside in the outer layer of the retina and exist in two types- the rods and cones. They can be thought of as being analogous to pixels in a camera. Both cell types transform the received light into electrical responses. Rods mostly exist in the peripheral regions and are most sensitive to low luminance conditions. Moving from the peripheral region towards the center of the retina, the density of rods gradually decreases, and cones become the prevalent cells. They are abundant in the center especially in the macula at very high densities. In the fovea, central region of the macula, only cones exist. They function in high luminance conditions and provide high VA and color vision.

Bipolar neurons are responsible for connecting the photoreceptors to the ganglion cells. They respond to light stimuli with graded changes in their membrane potential and not action potentials.[22,23] They are classified into two groups- ‘on’ bipolars respond to light stimuli through depolarization and ‘off’ bipolars through hyperpolarization. In a subretinal implant setting, the bipolars are the target cells that would connect to the implant electrodes.

Horizontal cells are inhibitory neurons contacting the photoreceptors on a much larger horizontal scale compared to bipolar neurons. Their cell bodies are located in the inner nuclear layer. Amacrine cells are lateral interneurons with no axons. Their somas are located in the inner nuclear layer while their dendritic tree extends into the inner plexiform layer. There are various types of amacrine cells exhibiting different morphologies and functionalities that are yet to be understood. In the most general sense, combined with horizontal neurons, they interact with bipolar and retinal ganglion cells.

Ganglion cells are the last neurons in the retina that receive the visual information mostly from bipolars. Different types of ganglion cells have specific image processing roles. Their axons bundle together to form the optic nerve. They are the first neurons that differentiate in the development of the retina. Ganglion cells are the target of epiretinal implants.

1-3.2. Retinal Glial Cells

Glial cells or neuroglia (nerve glue, as named by Rudolph Virchow in 1859) are non-neuronal cells in the nervous system. They are the most abundant cells in the CNS and constitute 90% of the brain. They have a range of functionalities depending on their type. Generally, they are considered the support system of neurons. They control the number and regulate the function of the synapses as well as encapsulating neurons to improve conductivity.[24,25,26,27] Glia also provide scaffolds for neurons to migrate along and grow on. Neurons and glial cells communicate through chemical signals of various types including ion fluxes, neurotransmitters and cell adhesion molecules.[28] Unlike neurons, glial cells can differentiate and proliferate (divide) throughout their life. There are 3 types of glial cells in the retina: astrocytes, Müller cells and microglia.

Astrocytes are the most numerous and diverse glia in the CNS.[29] They support neurons metabolically and remove excessive extracellular neurotransmitter secretions. They provide extra cellular matrix (ECM) proteins and adhesion molecules such as laminin and fibronectin and therefore influence neuronal migration, formation of neuronal aggregates and neural networks. They express glia fibrillary acidic protein (GFAP) and may exist in almost all retinal layers but enter the retina through the optic nerve. Together with the axons of retinal ganglion cells, they play a major role in the development of retinal vascularization.[30]

Müller cells are the predominant glial cells found only in the retina, accounting for 90% of the total glial cells and 20% of the volume of the retina in humans. [29,31] They are radially oriented cells that extend across all retinal layers. They promote synaptic formation, regulate information processing, ensheath somas and processes of retinal neurons, regulate and maintain the retinal blood flow as well as the blood-retinal barrier and maintain the ion and water homeostasis of the retina to name a few of the roles they play. They participate in the regulation of survival and death of neurons and photoreceptors and take part in the immunity of the system.[32] They express GFAP like astrocytes. It has been shown that Müller cells can be thought of as optical fibers that that would guide incoming light to the photoreceptors. This role is supported by their elongated extended funnel shape, orientation in the direction of light propagation and their higher refractive index compared to their surrounding tissue.[33]

Müller cells and astrocytes share many responsibilities and they can act interchangeably in some phenomena. Both glial types maintain the biomechanical scaffolding and biochemical homeostasis of the retina. Müller cells predominantly sheath the somas of retinal ganglion cells while their axons are sheathed by astrocytes.[31]

Microglia, like astrocytes, can reside in all layers of the retina. They play a key role in controlling immune responses of the retina and contribute to neuronal circuit remodeling and cell debris elimination.[31] The layered structure of the retina with all cell types is shown in Figure 1-3 a.

1-3.3. Gliosis

Any trauma or injury to the CNS that perturbs homeostasis could activate the glial cells' immune response leading to reactive gliosis. RP and AMD among other retinal diseases activate Müller cell gliosis that might accelerate the progression of neuronal degeneration.[34,35,36,37,38] Mild reactive gliosis may cause cellular hypertrophy and some changes in the functionality of the cells. Severe forms of reactive gliosis cause loss of cell functionality and form glial scars through extensive proliferation of Müller cells and astrocytes that would inhibit axonal growth and neuronal regeneration. Upregulation of GFAP is another sign of reactive gliosis. Müller cells survive most retinal injuries and become activated when facing any pathological condition in the retina.[32] Microglia also respond to injury by changing their morphology and expressing antigens.

Insertion of a rigid implant as a foreign object into any part of the nervous system combined with micron-scale motions, would impose severe trauma to the tissue causing a reactive gliosis response from glial cells that eventually would create a thick glial scar layer surrounding the implant[39,40] [Figure 1-3 b]. This layer would increase the distance between the electrode surface and targeted neurons and therefore inhibit the stimulation or the recording capability of the electrodes. The thickness of the glial scar layer depends on the size of the implant.[41] Preventing this immune response and achieving close contact between neurons and electrodes is crucial for maximum performance of the implants.[39,40,42,43,44]

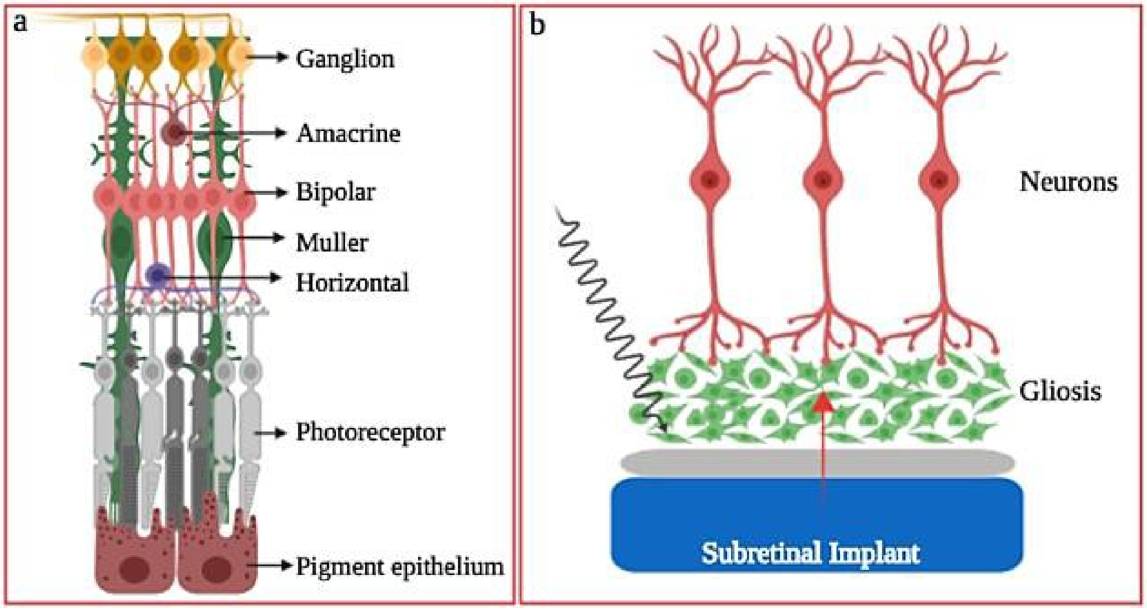

Figure 1-3. Schematic of the retina and glial scar on the surface of an implant. a) Various retinal cell types shown in the different layers. b) A glial scar layer forming on the implant surface, creates a gap between the electrode and the targeted neurons and pushes them away, out of reach of the generated signal (red arrow).

Microfluidics and chemical patterning have been extensively researched to limit glial proliferation to certain areas of the substrate and enhance axonal growth on other parts.[45,46,47,48] Antimitotic drugs have also been used to inhibit glial proliferation, but they also seem to affect neuronal survival and growth.[49,50] In general, chemical approaches are not a permanent solution due to their instability over time and microfluidics would limit access to the cells.

Other solutions to the glial scar problem include decreasing the implant size, using flexible and soft materials and micro patterning.

Decreasing the implant size could potentially reduce the trauma and therefore cause less glial cell response. Takashi et al. developed a composite electrode consisting of a carbon-fiber core an order of magnitude smaller than traditional recording electrodes and observed that glial inflammation response was reduced. [41,51] This solution has its own negative side effects as the reduction in electrode size would fail to provide a strong enough field for neuron stimulation. Providing higher charge densities could also damage either the tissue or the electrode.

The inflammation response induced by current implants is due to the mismatch between mechanical properties of the electrode to those of the biological tissue. The rigidity of current implants is about 6 times greater than the biological tissue in contact with them. [39,52,53] One approach to inhibiting glial cell response would be to match the stiffness of the implant to that of the targeted tissue.[54,55,56] Doan et al. showed that insertion of soft hydrogels into the CNS can reduce glial scar formation.[57] Georges et al. investigated promotion of either neuronal or glial growth by altering the stiffness of the substrate to above and below physiological values.[58]

Micron-scale geometric patterning has been extensively used to spatially separate neurons and glia on an implant surface. Butterwick et al. demonstrated that 65 nm tall nanopillars on a subretinal implant penetrate the inner nuclear layer of the retina without causing any major disruption, achieving better proximity to targeted neurons while Müller cells proliferated on the substrate in spaces between the pillars.[59] In another study, Piret et al. used dense arrays of GaP nanopillars separated by smooth GaP areas to guide retinal neurons and glial cells into different neighboring regions.[60] The micro-patterning method has the advantage of being more stable compared to chemical patterning over long periods of implant-tissue exposure in addition to providing both neuron and glial cell survival. These factors make this approach a more promising solution compared to the other methods.

1-4. Carbon Nanotubes Interfacing with Neurons

An appropriate electrode material needs to be biocompatible and nonbiodegradable to maintain its mechanical and electrical properties over long exposure times to the tissue, mechanically strong to provide enough support for cells[61], and at the same time flexible enough to be compliant with the target tissue and chemically modifiable to make it hydrophilic.[62] Materials that have similar mechanical characteristics to the biological tissue and that are purely capacitive with a large enough double layer capacitance and minimal impedance would be preferable.[54] Typical electrode materials are silicon, platinum[63], iridium oxide[64], titanium nitride[17] and gallium phosphide[65] to name a few.

Carbon nanotubes (CNTs) potentially meet all the requirements for an implantable electrode material. They are cylindrical structures made of rolled graphene sheets. Single walled CNTs (SWCNT) consist of one cylinder with a typical diameter of 0.4 to 2.5 nm and lengths of up to a few millimeters[66] and have either metallic or semiconducting properties.[67] Their mechanical and electrical properties depend on their chirality. Multi-walled CNTs (MWCNTs) are coaxial SWCNTs with diameters ranging from 2 to 100 nm and are metallic. They can be synthesized with lengths from a micron to a few hundred microns.[67] CNTs are flexible yet mechanically robust and not biodegradable[68,69], chemically inert and highly capacitive with low impedance.[70] Their fractal-like nanoroughness creates a large effective surface area and hence significantly improves the charge injection capacity and decreases electrode impedance.[71,72,73] In addition, their roughness, diameter and length to width aspect ratios match small neuron processes.[74,75] CNTs are intrinsically hydrophobic but can be made hydrophilic through various functionalization techniques to improve their biocompatibility.[76,77] CNT biocompatibility is still a debatable matter that depends on the existence of impurities and catalyst materials[78], along with the diameter, number of layers and length of the tubes[79,80,81] , as well as the degree of agglomeration in solution.[82,83]

Due to their unique characteristics, CNTs are excellent material candidates for both stimulating and recording electrodes. In fact, only 9 years after their discovery in 1991, their interaction with embryonic rat hippocampal neurons was studied for the first time.[84] Depending on the synthesis and preparation methods, the CNT density, topography and stiffness can change[85,86,87], which in turn can affect cell adhesion and growth. [61,62,88] CNT synthesis can also be combined with nano and micro fabrication techniques to create multielectrode arrays for controlling and guiding neuronal adhesion and migration into forming desired neural networks.[89] They can either be directly synthesized or transferred into flexible substrates to reduce inflammatory response.[90,91] Interactions of many cell types including neurons with various preparation of pristine and functionalized CNTs, such as horizontal CNT mats, randomly oriented and vertically aligned electrodes, or as coating on other materials, have been studied in the past two decades.[92,93] For an extensive review of CNT applications in neuronal devices, see references[70,94,95] Briefly, CNT electrodes promote neuronal adhesion and process growth, elongation and branching, increase number of neuron processes per cell, influence neuronal morphology, facilitate signal transmission, support and boost neuronal activity and improve signal to noise ratio. Figure 1-4 shows some previous studies performed by other groups on CNT-neuron interactions.

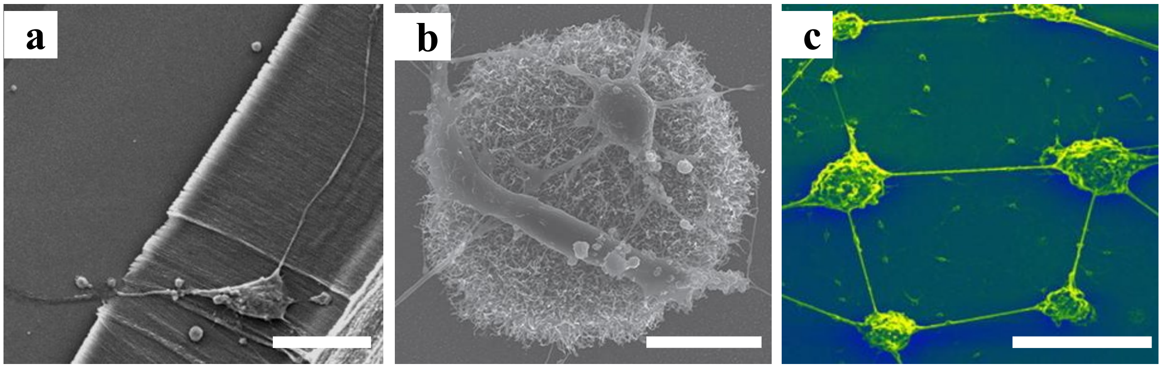

Figure 1-4. Literature examples of neuron interactions with various preparations of CNTs. a) SEM image of primary embryonic rat motor neurons cultured on horizontally aligned CNTs at 2 days *in vitro* (DIV). Image taken from Roberts et al. (2014)[96] b) HRSEM image of embryonic cortical rat neurons on top of randomly oriented CNT islands several microns tall. Image taken from Sorkin et al. (2009)[74] c) SEM image of embryonic rat cortical neurons on randomly oriented CNT islands at 21 DIV showing how the neural network adopts the CNT island patterning.[97] Scale bars on (a) and (b) are 10 µm and on (c) is 100 µm.

1-5. Fractals

A fractal is a self-similar mathematical or natural object that repeats itself at different size-scales. An exact or a mathematical fractal can be repeated infinite times whereas a natural fractal is statistically self-similar over a finite range. An exact fractal can be constructed from a scaled repetition of a simple Euclidean shape for example a line (H-tree), a curve (Dragon curve), a triangle (Sierpinski_triangle) or a cube (Menger_sponge). The scaling rate is characterized by D, the fractal dimension. D is a measure of how a fractal would fill the space it is embedded in and it can be a non-integer. For a fractal that scales at a rate α and has N new added objects, N is related to L and D:

$$N \propto \alpha^{-D}$$

An H-tree or a T-branching fractal (referred to as fractal electrode throughout the rest of the text) is constructed from a line segment with length L_0. Two line-segments scaled as

$$L_1 = \frac{L_0}{2^{\frac{1}{D}}}$$

are then added perpendicular to the endpoint of the first segment such that their endpoints coincide with the endpoint of the first segment. D is the fractal dimension of the H-tree that determines how the iterative lengths are scaled with respect to previous ones. This process can be repeated infinite times, scaling the length of the new added lines with the same ratio to the previous ones. The length of the nth segment as a function of the first one is then given by:

$$L_n = L_0/2^{\frac{n}{D}}$$

Figure 1-5 shows how an H-tree with D = 1.5 and 6 levels of scaling is created.

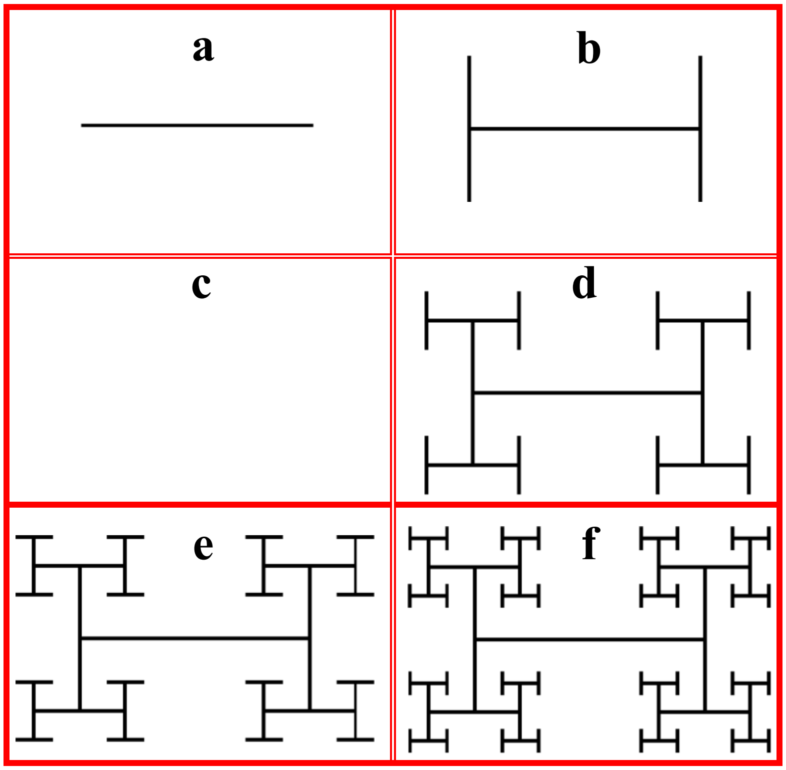

Figure 1-5. Schematic of different stages of an H-tree fractal generation. a) through f) show consecutive stages of generating an H-tree with D = 1.5 and 6 levels of scaling corresponding to 3 iterations.

Statistical fractals are prevalent in nature. Branching structures like trees, rivers, and neurons, and structures with peaks like mountain ranges; all are considered to be fractals over a finite range. These patterns do not look exactly the same at different magnifications, but they share the same general statistical characteristics. Figure 1-6 shows the difference between an exact branched fractal vs a statistical fractal tree in nature.

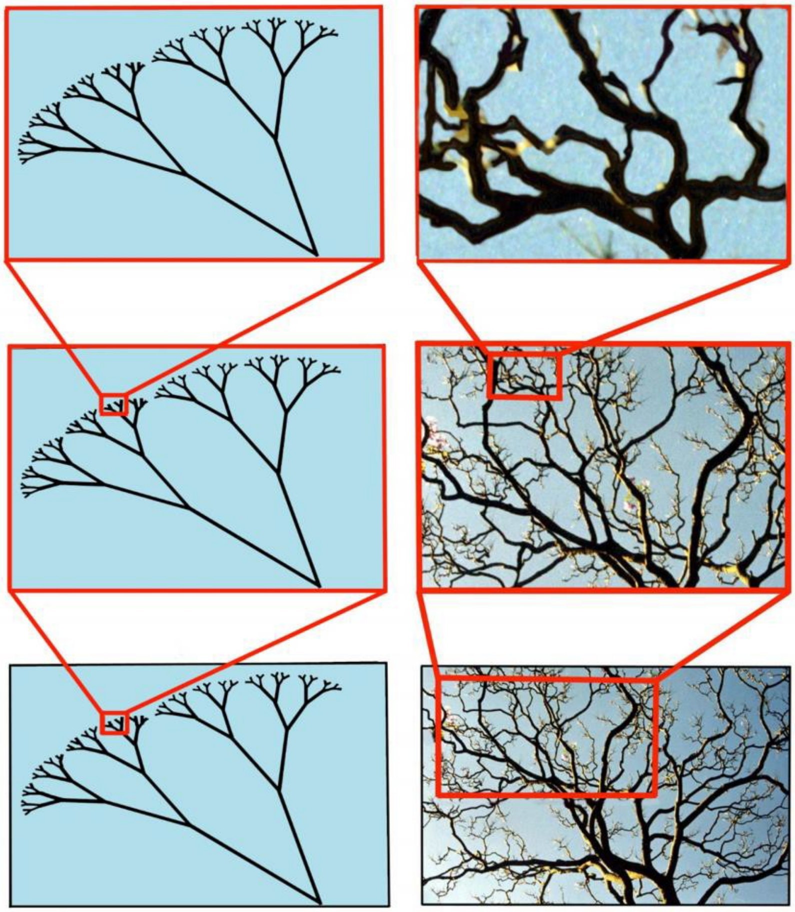

Figure 1-6. Comparison of an exact (left column) with a natural statistical branching fractal (right column). The exact fractal looks the same at finer size scales. The statistical fractal on the other hand, repeats statistically similar characteristics within a certain range at higher magnifications.

1-6. Motivation and Outline of the Thesis

Current retinal implants fail to restore a high enough VA due to the fundamental mechanical and chemical incompatibilities between the electrode material and the biological tissue. The rigid electrode typically has a Young's modulus six times larger than the neural tissue. [55,98] This mismatch in stiffness combined with the mechanical stress due to micromotions of the implant against the soft tissue causes a reactive gliosis response from glial cells, increasing the distance between the electrode and targeted neurons and decreasing the stimulation power of the implant. In addition, in the case of implants powered through photodiodes, the flat Euclidean geometries of electrodes would block most of the light from entering the photodiode further hindering its stimulating power.

In the past few years, studies have focused on the use of materials with nanoporous surface roughness that mimics the characteristics of biological tissue, in combination with implant size reduction and patterning to improve electrode-neuron interactions and hinder glial response while also improving the spatial resolution of the electrodes. Nanorough materials or porous coatings increase the effective surface area of the implant and hence provide more surface charge.[99] Yet, unanswered questions about the nature of interactions between the artificial electrode surface and the neural tissue still exist. Use of materials that mechanically mimic the stiffness and roughness of the tissue does not seem to be a strong enough modification. There is still a fundamental discrepancy between the geometric characteristics of the stimulating/recording electrodes to that of the neurons. As was discussed previously, neurons belong to a group of special geometries called statistical fractals, with characteristics completely different to Euclidean electrodes. This fundamental difference could have a negative impact on the connectivity of the electrode to the tissue.

For developing the bio-inspired implants in this thesis, VACNTs were chosen as the electrode material because of their remarkable properties, high aspect ratios and capability to be patterned into sub-micron scale features. H-tree fractals were chosen as the electrode geometry due to their unique geometrical properties and branching structure. Compared to square electrodes with the same bounding area, they would increase the amount of light entering the photodiode through the existing holes in their structure. They provide more sidewalls and therefore more surface area for charge accumulation, therefore increasing their capacitance and stimulating power compared to conventional electrodes with the same covering area.[100] Figure 1-7 displays simulation results by Watterson et al. showing that 4-iteration H-tree fractals generate higher voltages penetrating the extracellular space compared to grids and squares with the same covering area [Figure 1-7] and therefore stimulate more neurons. Simulations have also shown that the use of a 20 × 20 μm^2 H-tree electrodes would theoretically improve VA to 20/80 vision[101] [Figure 1-8]. For comparison, current implants provide a VA of about 20/500 at best which is not nearly enough since most RP and AMD patients have visions better than 20/200 through the course of the disease until the very late stages.

Combined together, the CNT plus fractal system could provide electrode branches (with many edges) with nanorough surfaces for neuronal adhesion, growth and stimulation while guiding and enhancing glial cell proliferations into the smooth multi-scaled areas in between them and away from the electrode surface. This system does not fully eliminate the presence of glial cells and keeps them close to neurons since they are crucial for neuronal health and survival. Furthermore, electrodes with statistical fractal geometries (specifically with fractal dimensions) that match targeted neurons could be developed to further improve the resemblance of the implant to the biological tissue and ensure its integration into the tissue (fractal resonance hypothesis). Figure 1-9 is a schematic representing current commercial electrodes with Euclidean geometries vs exact and statistical fractal electrodes.

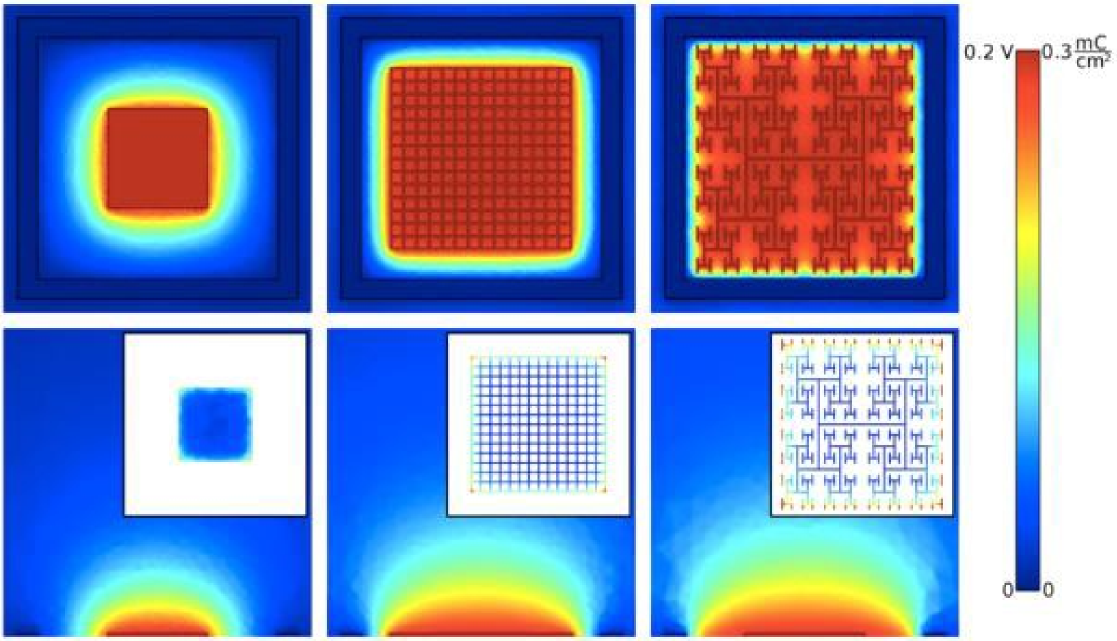

Figure 1-7. Comparison between a square, grid and fractal extracellular voltages. The first row is the horizontal distribution of the voltages generated by a square, grid and fractal with the same covering area. The second row shows the penetration of the voltage into the extracellular space for a vertical slice in the middle of the electrodes. The insets show the charge density distribution for each geometry. The bounding area for all electrodes is 20 × 20 μm^2 and they are 250 nm tall. Image taken from Watterson et al. (2017)[100]

20/20 vision

20/1000 vision

20/80 vision

Figure 1-8. VA improvement by implants that use fractal electrode shapes. 20/20 VA is the normal vision. 20/1000 is the VA current implants typically provide. 20/80 is the theoretical VA that could potentially be restored with fractal electrodes.

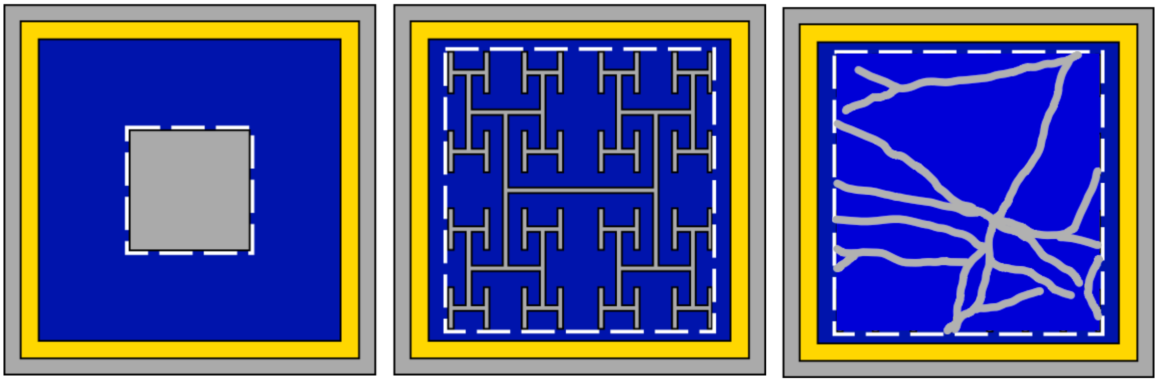

Figure 1-9. Schematic of different electrode types. Commercial electrodes with Euclidean geometry vs exact and statistical fractal electrodes with fractal dimensions matching their targeted neurons is shown. The dark blue is the photodiode, the grey regions are the conductive electrodes and the yellow is the insulating region between them. Left and middle panels in the image taken from Watterson et al. (2017)[100], right panel added. The lines on the statistical electrode on the right are actual traces of neuron processes cultured on a uniform CNT mat.

The work presented in this thesis solves the gliosis dilemma at the neuron-electrode interface by providing micron and nano scale mechanical guidance for both neurons and glial cells. Chapter II describes the design of the electrode geometries, fabrication and characterization, experimental procedures, data acquisition, image processing and statistical analysis of the data. Chapter III focuses on fundamental understanding of retinal cell behavior and mechanical guidance using a simple Euclidean geometry of rows of

CNTs separated by Si regions. The effect of culture time on the final state of the system is also investigated. Chapter IV studies the effect of fractal vs Euclidean geometries on retinal cell behavior, migration and glial proliferation and predicts fractal properties that could potentially enhance neuronal and glial separation into adjacent regions. It is concluded that fractal geometries would enhance neuron and glial cell “herding” into their designated areas compared to Euclidean ones. Chapter V covers some early future studies on fractal comparison with a few more Euclidean geometries such as grids and squares, as well as the fractal resonance concept. The findings of this research are not limited to retinal cell interactions with an electrode surface and can be extended to implants interfacing with any part of the nervous system.

CHAPTER II

MATERIALS AND METHODS

This chapter focuses on sample design, preparation and fabrication, synthesis and characterization of vertically aligned carbon nanotubes (VACNTs) as an electrode material for interfacing with retinal cells. CNT characterization methods, dissociated retinal cell cultures, immunohistochemistry, post-culture fluorescence and SEM imaging, image processing techniques and algorithms, parameter definitions and statistical data analysis are explained.

Two sets of geometries with distinct characteristics, Euclidean rows and H-tree fractals were designed and fabricated. Dissociated retinal cells were cultured on the samples. Immunohistochemistry techniques were used to mark neurons and glial cells with specific markers for fluorescence microscopy imaging. Scanning electron microscopy was used prior and post culture to characterize the nanotubes and the cells on them. Contact angle goniometry was used to measure the degree of hydrophobicity of the CNTs. Image processing algorithms were developed to detect and quantify neuron processes and glial cell areas. And finally, statistical analyses were performed to quantitatively compare the two electrode geometries.

Experimental procedures were performed by graduate students in the Taylor and Alemán labs. Saba Moslehi (SM) fabricated samples. SM, William J. Watterson (WJW), Kara M. Zappitelli (KMZ), Conor Rowland (CR) imaged and characterized CNT samples. David Miller (DM), KMZ, Curtis Colwell, Derek Hallman, and Benjamín Alemán (BA) designed and developed the VACNT synthesis process. DM built the CVD furnace, the gas delivery system, and wrote the CVD control software. SM, WJW, KMZ, Julian H. Smith (JHS) and CR performed cultures, immunohistochemistry and fluorescence imaging procedures. SM, WJW and JHS developed the necessary image processing tools. SM and JHS performed image processing. SM completed statistical analysis of the data and analyzed the results. All students were trained on the culture protocols by Maria-Thereza Perez (MTP). Richard P. Taylor and (BA) were PIs on this project.

2-1. Design and Fabrication

2-1.1. Euclidean Patterns

The Euclidean patterns consisted of rows of CNTs with width W_{CNT} separated by rows of Si with width W_{Si} in a 6 × 6 mm^2 area. They were designed and created in AutoCAD and were printed as physical masks in two general groups. The first group, called R through the rest of the text, had a constant $W_{CNT} = 100$ μm. W_{Si} varied from 25 to 100 μm in 25 μm increments but was constant within a single sample. As an example, R25 refers to samples with $W_{CNT} = 100$ μm and $W_{Si} = 25$ μm. In the second group, called GR, W_{CNT} and W_{Si} were varied together from 25 to 100 μm in 25 μm increments, being constant within individual samples. The Euclidean groups cover the geometric parameter space along the two solid (group R) and dashed (group GR) red lines shown in Figure 2-1.

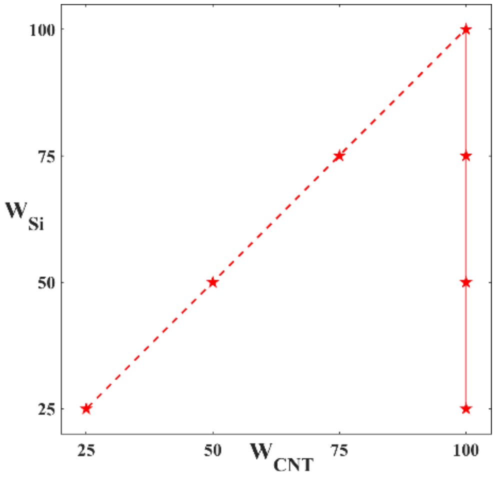

Figure 2-1. Geometric parameter space for two Euclidean groups. The solid red line represents group R and the dashed red line shows group GR. The stars are the different sample measurements in each subgroup.

2-1.2. Fractal Patterns

The H-tree fractal skeletons with no linewidth were first created using a fractal generator program given the fractal dimension and number of branches (or iterations) as inputs. The skeleton was then converted into a 2D pattern using a MATLAB algorithm based on the width of branches and the half-length of first branch of the fractal. Incorporating the fractal dimension D, the number of branches N_f, the width of the branches w_f and the length of the pattern X_L, the following fractal geometric parameters were calculated:

$$L_0(N_f, X_L, \mathrm{D}, w_f) = (X_L - w_f)/2 \sum_{n=0}^{(N_f-1)/2} 1/2^{\frac{2n}{D}}$$

$$L_n(N_f, X_L, \mathrm{D}, w_f) = L_0/2^{\frac{n}{D}}$$

$$L_f(N_f, X_L, \mathrm{D}, w_f) = L_0 \sum_{n=0}^{N_f} 2^{n+1}(1/2^{\frac{1}{D}})^n$$

$$E_f(N_f, X_L, \mathrm{D}, w_f) = \frac{2 * A_f}{w_f} + w_f * 2^{(N_f+1)} - \sum_{n=1}^{N_f} 2^n * w_f$$

$$A_f(N_f, X_L, \mathrm{D}, w_f) = w_f L_f - \sum_{n=1}^{N_f} 2^n \left(\frac{w_f}{2}\right)^2$$

$$\mathrm{A}_{\min}(N_f, X_L, \mathrm{D}, w_f) = L_0^2 \left(\frac{1}{2^{\frac{N_f-2}{D}}} * \frac{1}{2^{\frac{N_f-1}{D}}}\right) - w_f L_0 \left(\frac{1}{2^{\frac{N_f-2}{D}}} + \frac{1}{2^{\frac{N_f-1}{D}}}\right) + w_f^2$$

$$\mathrm{A}_{\max}(N_f, X_L, \mathrm{D}, w_f)$$

$$= 2L_0^2 \left(1 - \sum_{n=1}^{(N_f-1)/2} 1/2^{\frac{2n}{D}}\right) \left(\sum_{n=0}^{(N_f-1)/2} 1/2^{\frac{2n+1}{D}}\right)$$

$$- L_0 w_f \left(\sum_{n=0}^{(N_f-1)/2} 1/2^{\frac{2n+1}{D}}\right) - L_0 w_f \left(1 - \sum_{n=1}^{(N_f-1)/2} 1/2^{\frac{2n}{D}}\right)$$

$$+ (w_f/2)^2$$

$$A(N_f, X_L, \mathrm{D}, w_f)$$

$$= 2L_0^2 \sum_{n=0}^{(N_f-1)/2} 1/2^{\frac{2n+1}{D}} - \sum_{n=1}^{(N_f-1)/2} \sum_{m=n}^{(N_f-1)/2} 1/2^{\frac{2m+2n+1}{D}}$$

$$- L_0 w_f \sum_{n=1}^{(N_f-1)/2} \sum_{m=2n+1}^{N_f} 2^m / 2^{\frac{2n+m}{D}} - L_0 w_f \sum_{n=0}^{N_f} 1/2^{\frac{2n}{D}}$$

L_0, L_n, L_f, E_f, A_f, A_{min}, A_{max} and A are half length of the zeroth order branch, length of the nth branch, total length, total edge length, total covering area, smallest rectangular area, largest rectangular area and maximum connected area of the fractal respectively. These parameters are modified and used to describe certain properties of fractals later in Chapter IV.

Two groups of H-tree fractal patterns were designed and created. The first group consisted of three fractal D-values (1.1, 1.5 and 2) with the same number of branches (N_f=

7), same branch width (w_f= 20 µm) and same X_L. The X_L length was chosen to be roughly the same as the Euclidean (groups R and GR) lengths. For the second group, the D-value was kept at 2 and the number of branches was increased. 4, 5 and 6 iteration patterns (corresponding to N_f = 7, 9 and 11, since the number of iterations is $2N_f$-1) were created. The fractal patterns are referred to as 1.1, 1.5, 2-4, 2-5 and 2-6 throughout the text. X_L for the second group was chosen such that the distance between the tip of the final branch and the direction of the (N_f - 3)th branch in 2-6 fractals, d_v, was 25 µm. Figure 2-2 inset shows how d_v is defined. Considering the values chosen for X_L and w_f, increasing the number of branches beyond 11 would have caused an overlap of the higher iteration branches and resulted in creating closed Si spaces within the fractal pattern and therefore trapping the cells. Each pattern was created separately as a DesignCAD file. AutoCAD was then used to combine all patterns within a 2-inch diameter area as a mask for a whole wafer. The file was then converted to the CiF format for use in the direct laser writer. Figure 2-2 shows the schematic for a 1.5 fractal. The inset is a zoom in of the red box depicting what d_v is.

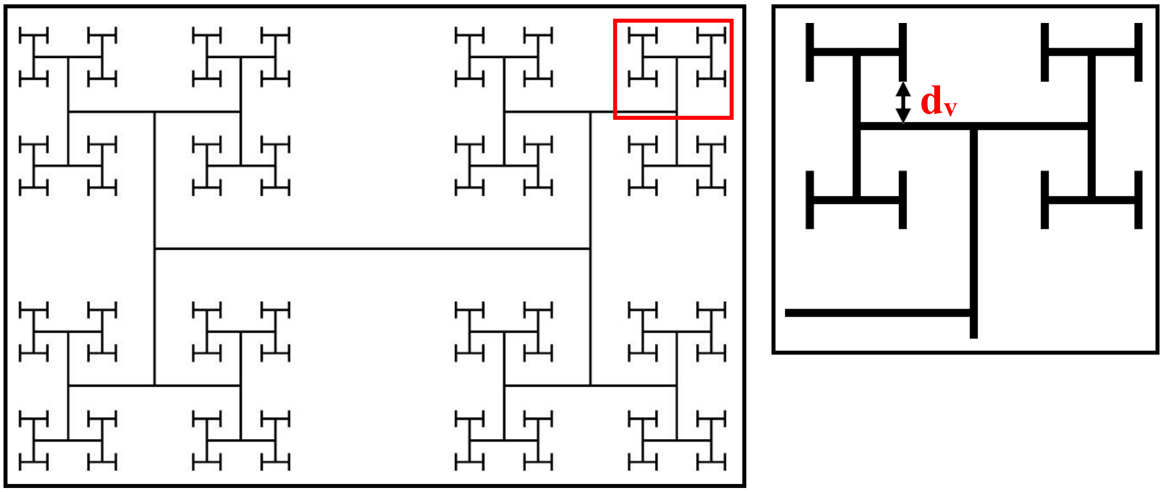

Figure 2-2. Schematic of a fractal with D = 1.5 and 4 iterations. The inset is a zoom in of the red box area representing how d_v is defined.

2-1.3. Sample Cleaning and Photoresist Spin-coating

For all the experiments, 2-inch silicon wafers (P-doped, 500 µm thick with a 300 nm thick thermal oxide layer on top, 100 orientation, purchased from University Wafer) were used. Whole wafers were cleaned in an acetone bath with sonication for 10 minutes, then rinsed with isopropyl alcohol (IPA) and dried with N_2. They were then dehydrated on hot plate at 400°C for 10-15 minutes. To increase photoresist adhesion to the substrate for the Euclidean groups, wafers were exposed to hexamethyldisilazane (HMDS, purchased from Sigma Aldrich) under a trough for 20 minutes. A 2 µm thick layer of AZ1512 photoresist (purchased from Merck KGaA) photoresist was then spin-coated at 4000 rpm for 30 seconds followed by 2 minutes of pre-exposure bake at 105°C on a hot plate.

A bilayer resist technique was used to create the narrower fractal patterns. First, a ~50 nm thick layer of Polydimethylglutarimide (PMGI, purchased from MICROCHEM LABORATORY) was spin-coated at 4000 rpm for 45 seconds and pre-baked at 190°C for 5 minutes. Then the 2 µm thick layer of AZ1512 photoresist was spin-coated on the wafers at 4000 rpm for 30 seconds followed by a 2-minute pre-exposure bake at 105°C on a hot plate.

2-1.4. Photolithography and Post-exposure Development

The Euclidean patterns were transferred to the wafers using the physical masks and an OAI HYBRALIGN Series 200 mask aligner with a collimated UV light source (200 to 2000 watts) providing wavelengths from 220 to 436 nm. The fractal patterns were written on the coated wafers using a direct-write laser lithography system with a mask writing tool.

The following settings were used in the direct laser writer system: lens #5 for small features and narrow linewidths, 3% filter and a gain of 23.8 equivalent to 220 mJ/cm^2.

Wafers were post-exposure baked on a hot plate at 105°C for 1 minute, then developed in AZ300 MIF (purchased from Merck KGaA) for 60 (Euclidean) and 30 (fractal) seconds, rinsed with DI water, blow dried with N_2 and hard-baked at 105°C on a hot plate for 2 minutes.

2-1.5. Catalyst Deposition

Iron (Fe) was chosen as the catalyst for our CNT synthesis since it is an appropriate choice for synthesizing vertically aligned carbon nanotubes compared to other common catalysts such as nickel (Ni). In a previous study by Zhao et al. it was shown that Fe combined with aluminum oxide (Al_2O_3) as a supportive layer gave the best growth efficiency for vertically aligned CNT forests compared to other catalyst-support layer combinations.[87] In another study by Delzeit et al. the addition of an underlayer such as Al_2O_3 between the catalyst and the Si substrate, instead of any form of pretreatment such as treating with ammonia or ion bombardment, increased the surface roughness and provided more active nucleation sites. In addition, in some cases the metal underlayer prevented the excess catalyst layer from rising to the top of the nanotubes and starting secondary growths.[102]

The catalyst and support layer thicknesses were chosen based on the results of a few previous studies. Bronikowski et al. showed that adding about 3 nm of Al_2O_3 between the Si and Fe would result in more reproducible growths of CNT bundles. Thinner layers of Al_2O_3 did not create a thick enough oxide layer and thicker layers were not oxidized completely.[103] In a follow-up study they showed that layers of Fe thinner than 0.5 nm or thicker than 6 nm did not give significant CNT growth.[85] Zhao et al. also showed that a 3 to 5 nm thick Fe layer would produce double and multiwalled CNTs.[87]

For group, R 3-5 nm of Al_2O_3 and 5-7 nm of Fe were thermally deposited on patterned wafers at 10^{-5} Torr using a motorized bell jar hoist model BJH-500. For the GR and fractal groups, a 3-4 nm Al layer was deposited thermally and a 5-6 nm Fe layer through E-beam evaporation (AMOD deposition system /Angstrom engineering).

The photoresist layer was removed in an acetone bath with sonication for the Euclidean samples and in remover PG (purchased from MICROCHEM LABORATORY) with sonication for 1 and 10 minutes respectively. The wafers were rinsed with IPA and dried with N_2. Prior to CNT synthesis, the wafers were cut into individual samples using a diamond scribe pen, rinsed with acetone and IPA and dried with N_2 once again to remove any dust particles.

2-1.6 Carbon Nanotube Synthesis

CNT synthesis was performed through a chemical vapor deposition (CVD) process in a 2-inch quartz tube for 3 minutes at 650 °C in a 2:1 mixture of ethylene (C_2H_4) and hydrogen (H_2) at 200 and 100 standard cubic centimeters per minute (SCCM) respectively at atmospheric pressure. A 600 SCCM flow of argon was maintained during synthesis to keep the tube clean. The temperature and gas mixtures were chosen according to several studies by Bronikowski et al. which showed that temperatures between 650 °C to 750 °C were best for achieving the optimum Fe particle motility to create nucleation sites as well as C_2H_4 decomposition, but at temperatures higher than 650°C growths gave inconsistent CNT growth results. [85,103]

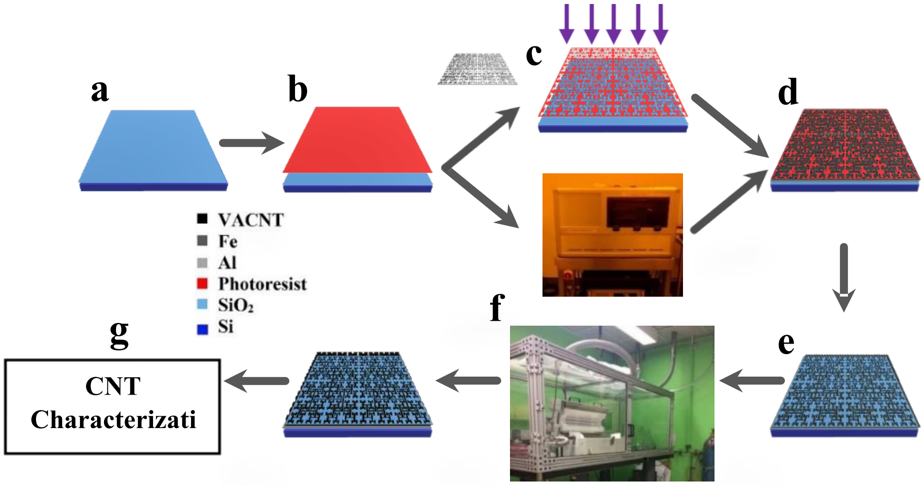

CVD furnace, David Miller, Alemán lab

Figure 2-3. Diagram of all fabrication steps of Euclidean and CNT samples. a) Cleaning wafers, b) Spin-coating photoresists, c) Photolithography with masks and UV light (Euclidean) or direct laser writing tool (Fractal), d) Depositing catalyst layers using thermal and E-beam evaporators, e) lifting off photoresist, f) Synthesizing CNTs in CVD furnace and g) characterizing CNTs via various methods.

2-2. Scanning Electron Microscopy (SEM)

A ZEISS Ultra-55 scanning electron microscopy system located at CAMCORE facility, University of Oregon, was used to measure CNT heights and visually characterize the structure and topography of the top surface and sidewalls of CNTs.

No obvious visual differences in height and top surface topography were detected between samples from different fabrication procedures. CNT heights across all samples for 3-minute growths were between 20 to 45 µm. Figure 2-4 is a collection of some examples of top and angled views of patterned CNT forests.

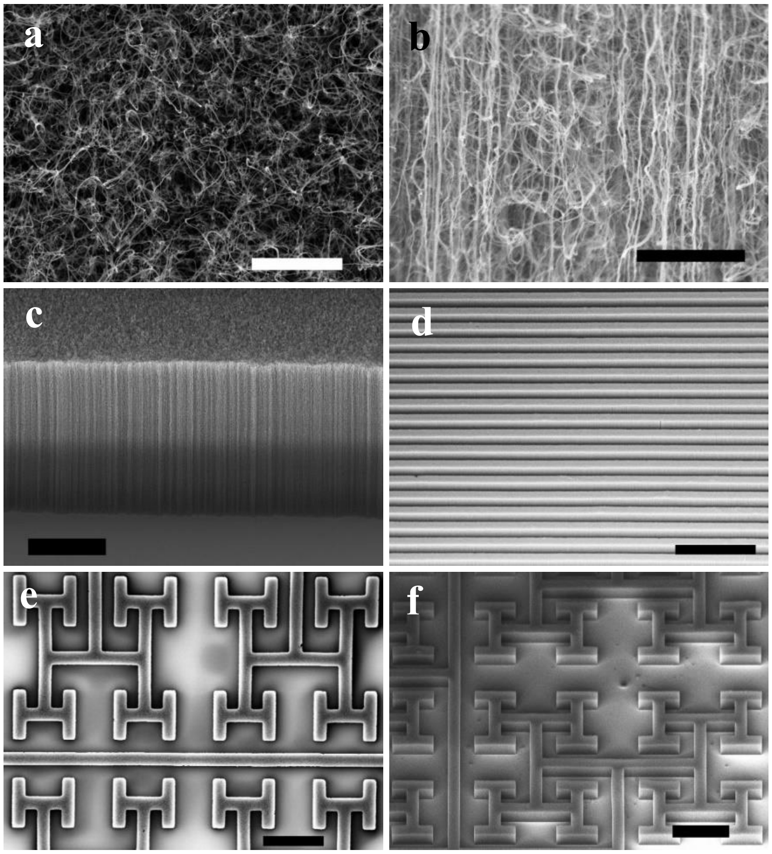

Figure 2-4. SEM images of patterned CNT forests taken before culturing experiments. A) View of entangled CNTs on the top surface of the forest, b) Zoom in on the texture of the sidewall of a CNT row taken at a 40 ° angle, c) View of the sidewall of a CNT row taken at a 40 ° angle giving the CNT height, d) Zoom out of a GR25 sample taken at a 40 ° angle, e) Top-down view of a 2-6 fractal electrode, f) Side view of a 2-6 fractal electrode taken at a 40 ° angle. Scale bars are 2, 1, 10, 200, 200 and 100 μm respectively.

2-3. Contact Angle Goniometry

Wetting contact angle (WCA) is a measurement of wettability or hydrophobicity of a solid surface. A Ramé-Hart Model 290 goniometer was used to determine the hydrophobicity of the top surface of uniform CNT mats by measuring the WCA of a water drop with a diameter of 10 μm immediately after it contacted the top surface [Figure 2- 5]. Wetting angles on the right and left side of the drop were measured a few times for several samples and the average was taken. The WCA for the CNT top surface was 158.3 ± 2.6 ° indicating that our CNT surfaces were super hydrophobic.

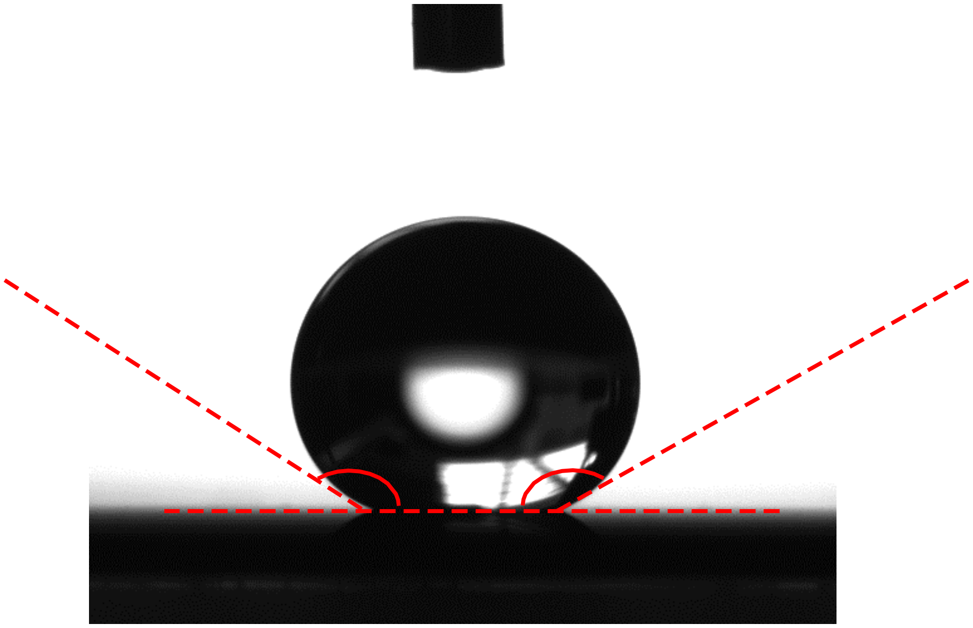

Figure 2-5. Contact angle goniometry of synthesized CNT samples. Image of a 10 µm water drop on the top surface of a CNT mat. The almost spherical shape of the drop indicated how hydrophobic the CNT surface was.

2-4. Culture Procedure

2-4.1 Animals

Wildtype C57BL/6 mice were kept at animal welfare services at University of Oregon according to protocols approved by University of Oregon's Institutional Animal Care and Use Committee (IACUC). The animals had full time access to fresh water and food supplies.

2-4.2. Dissociated Retinal Cell Cultures

Dissociated retinal cells were cultured using protocols as previously described.[65] Briefly, postnatal day 4 mice were euthanized through decapitation, then full retinas were dissected and were kept in Dulbecco's Modified Eagle Medium (DMEM) containing high-glucose, sodium pyruvate, L-glutamine and phenol red (purchased from Thermo Fisher Scientific). 4 full retinas were transferred into an enzyme solution containing 3 mL of DMEM, 3 mg of papain (purchased from Worthington Biochemical Corporation), and 0.9 μg of L-cysteine (purchased from Sigma-Aldrich) filtered through a 0.22 μm filter (purchased from Sarstedt). The solution was mixed gently and was incubated at 37 °C for 22.5 minutes to break cell bonding. The enzyme solution was then removed, and the retinas were rinsed 3 times in 10 ml of warm DMEM. After the last rinse, the DMEM was removed, 2 ml of final culture medium containing 10.67 mL of DMEM, 220 μL of B27 supplement (purchased from Sigma-Aldrich), and 110 μL L-glutamine-penicillin-streptomycin (purchased from Sigma-Aldrich) was added to the digested retinas. To completely dissociate the retinas and remove neuron processes, a rounded Pasteur pipette was used to mechanically agitate the medium plus retinas. Next, 48 ml of DMEM was added to the 2 ml of dissociated retina solution and centrifuged at 900 g for 5 min. The supernatant was then removed carefully. 9 ml of the final culture medium was added to the cell pellet. Using a new rounded Pasteur pipette, the cells were resuspended throughout the solution. The suspension was then passed through a 40 μm cell strainer filter (purchased from Fisher Scientific) to remove large cell clusters. Finally, the patterned CNT samples were placed into 4-well culture plates (purchased from Sarstedt). Each well's area was 1.9 cm^2. Each well was seeded with 500 μL of cell suspension. Samples were incubated for 3, 7 and 17 days *in vitro* (DIV) at 37 °C and 5% CO_2. The average live cell density, as measured by a hemocytometer, was 3.6×10^6 cells/mL.

2-4.3. Fixing

The cells were fixed with 2% and 4% paraformaldehyde for 10 and 20 minutes respectively. They were then rinsed 3 times with 1× phosphate buffered saline with pH 7.3 (PBS, containing chloride (NaCl), Sodium phosphate (Na_2HPO_4), potassium chloride (KCl) and monopotassium phosphate (KH_2PO_4)) each time for 10 minutes and finally were incubated in the last rinse overnight at 4 ^{o}C. The earliest time samples were fixed was after 3 DIV which coincides with a P7 (postnatal day 7) retina. At P7, ganglion, horizontal, cone and amacrine cells are fully differentiated. Rods, bipolars and Müller cells have already started differentiating but are not fully developed [Figure 2-6]. By 17 DIV, equivalent to P21, all retinal cells are fully differentiated.

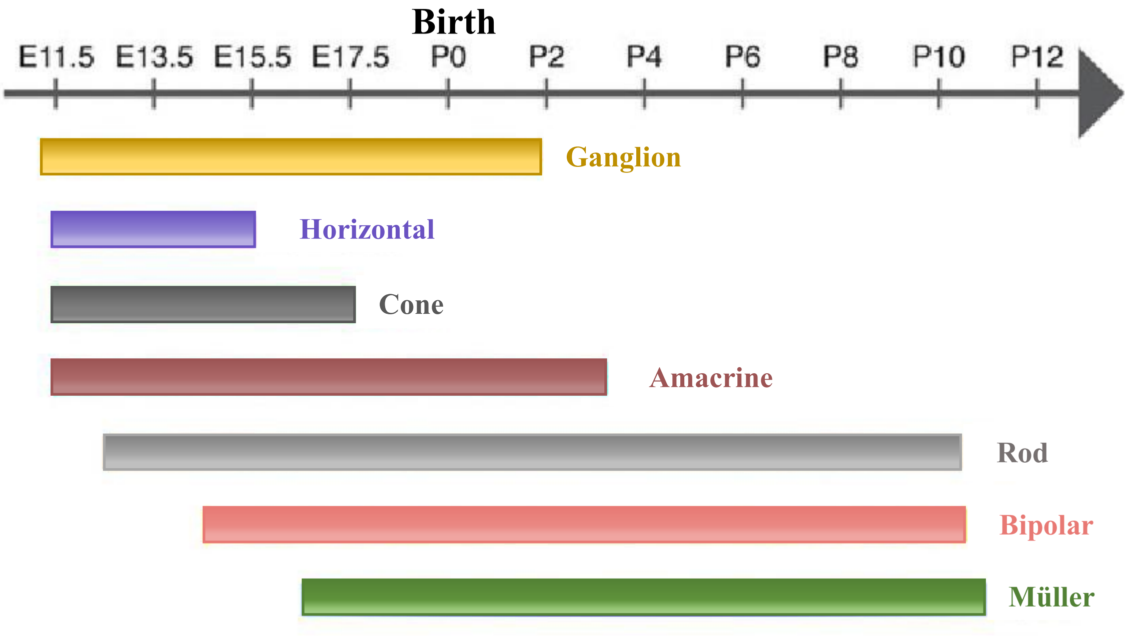

Figure 2-6. Development of mouse retinal cells before and after birth. Image taken from Xiang (2012) and modified.[104]

2-4.4. Immunohistochemistry

After another 10 min 1×PBS rinse, the cells were pre-incubated in PBScomp-NS solution containing 1×PBS, 0.25% Triton-X (purchased from Sigma-Aldrich), 1% bovine serum albumin (BSA) (purchased from Sigma-Aldrich), 2% donkey normal serum (DNS) and 2% goat normal serum (GNS) (purchased from Jackson ImmunoResearch) for 60 minutes at room temperature. After removing the PBScomp-NS solution, the cells were incubated overnight at 4 ^{o}C in primary antibody solution, PBScomp-NS-pAb solution containing PBScomp-NS, 1:1500 rabbit anti-tubulin III (purchased from Sigma-Aldrich) and 1:1500 goat anti-GFAP (glial cell marker) (Dako). Next, cells were rinsed in 1×PBS 3 times, each for 10 minutes. They were then incubated for 45 minutes at room temperature in secondary antibody solution, PBScomp-sAb containing 1×PBS, 0.25% Triton-X, 1% BSA, 1:400 AlexaFluor 488 donkey anti-rabbit IgG and 1:200 Cy3 goat anti-mouse IgG (purchased from Jackson ImmunoResearch). After removal of the secondary antibody solution, the cells were rinsed again 3 times in 1×PBS, were mounted on microscope slides with Vectashield containing DAPI (a DNA marker in the cell nuclei) (purchased from Vector Labs) and covered with coverslips using a double-sided tape between the microscope slide and the coverslip.

Class III β-tubulin is expressed in certain retinal neuron types and their axons and dendrites.[105] Throughout this thesis, all of these different types are referred to under the general term neuron. In addition, the term neuron processes refers to both axons and dendrites without any further specification. In the case of glial cells, the word glia is also a general term referring to both Müller cells and astrocytes.[65]

2-5. Post-Culture Imaging

2-5.1. Fluorescence Imaging

A Leica DMi8 inverted fluorescence microscope was used to take 20× images in the Cy3 (excited at 550 nm, emission peak at 570 nm), GFAP (excited at 493 nm, emission peak at 519 nm) and DAPI (excited at 358 nm, emission peak at 461nm) channels of all samples. The top CNT and bottom Si surfaces were imaged separately with focus being adjusted on each respectively. The 2048 × 2048 pixel^2 field of views (FOVs) in each channel were then stitched together using an automated stitching algorithm with 10% overlap at the edges of neighboring FOVs to create full sample images. Figure 2-7 shows a 40× fluorescent image of the three channels merged at a CNT-Si boundary.

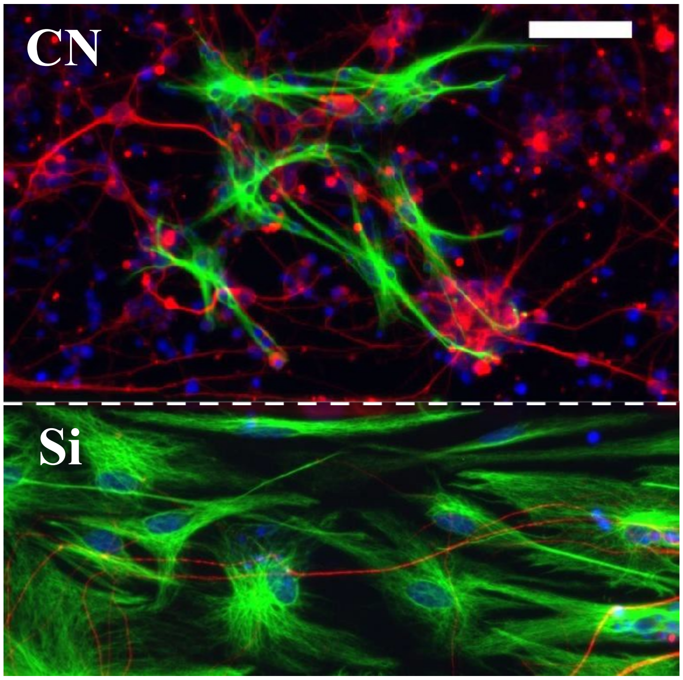

Figure 2-7. Fluorescence image of neurons and glial cells on CNT and Si surfaces. A 40× merged fluorescence image of neurons (red), glia (green) and cell bodies (blue) at a CNT - Si boundary. The part above the white line is taken with the focus adjusted on the CNT surface and the one below with the focus adjusted on the Si surface. The two images were manually combined after merging channels. Scale bar is 50 µm.

2-5.2. SEM Imaging

A different fixing and dehydration protocol combined with gold sputtering was performed on cultured samples to prepare them for SEM imaging. This allowed for viewing and studying CNT and Si surfaces while also viewing cells and processes attached to surfaces at the same time. The cells were fixed with 1.25% and 2% glutaraldehyde for 10 and 20 minutes respectively. The samples were then rinsed 3 times with 1×PBS, each time for 10 minutes. They were then submerged in increasing concentrations of ethanol (50%, 60%, 70%, 80%, 90% and 100%) for 15 minutes each to dehydrate the sample fully. The 100% ethanol was repeated once more. HMDS was used as chemical drying agent to dehydrate samples without exposing them directly to air. Samples were submerged in a solution of HMDS:100% ethanol, followed by 100% HMDS, each for 20 minutes. Once in the second 100% HMDS bath, they were covered and left overnight, during which the HMDS evaporated and the samples were completely dry. A 20 nm layer of gold was sputtered on samples before imaging. Figure 2-8 shows an example SEM image of cell bodies and neuron processes on CNT and Si surfaces. Cells and processes on CNT are false-colored in red.

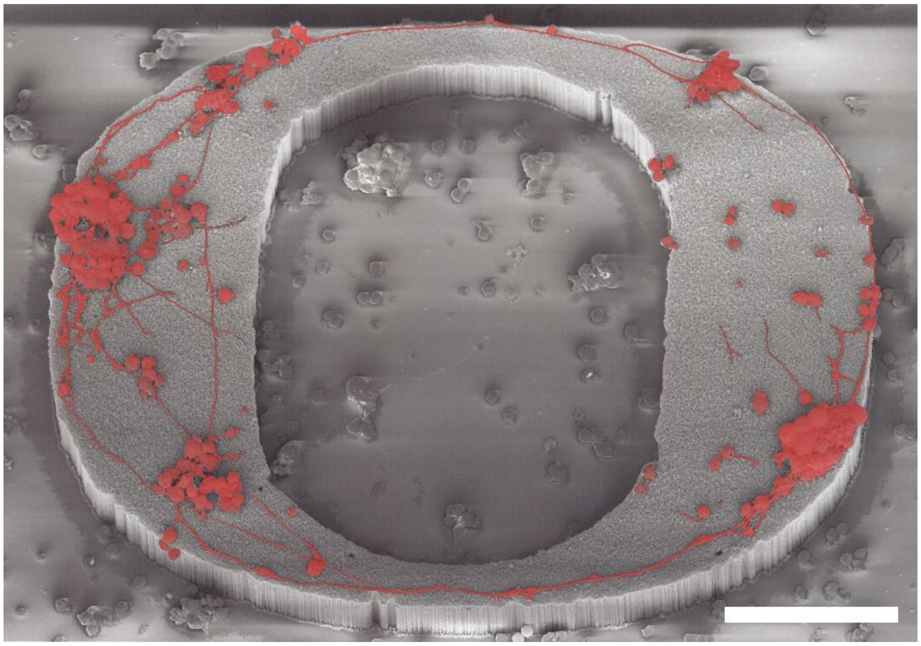

Figure 2-8. SEM image of cells attached to both CNT (shaped as an 'O') and Si surfaces. Cell bodies and processes on the CNT surface are false-colored in red. Scale bar is 50 μm.

2-6. Data Analysis

2-6.1 Mask algorithm

Binary masks with pixels of zeros and ones were created for each Euclidean and fractal sample based on D, number of iterations and width measurements done on the fluorescent images. These masks were then applied to all acceptable FOVs within a sample to distinguish between CNT and Si surfaces. Mask algorithms were developed by JHS.

2-6.2 Neuron Process Length Algorithm

An automated neuron process detection algorithm developed by WJW based on a previously reported one by Wu et al.[106] in combination with the mask algorithm was used to detect and measure total neuron process length in pixels per FOV on the CNT and Si surfaces separately. The interest was on total process length per surface type and not per soma. Total process length on the CNT and Si and total CNT and Si area per sample were calculated by adding those parameters for the accepted FOVs that were included in the analysis for each sample and were converted to µm and µm^2. Those FOVs that had abnormalities were excluded from the analysis. Normalized total neuron process length for Si and CNT per sample was calculated as follows:

$$N_{Si} = \frac{Total\ process\ length\ on\ silicon\ per\ sample}{Total\ silicon\ area\ available\ per\ sample}$$

$$N_{CNT} = \frac{Total\ process\ length\ on\ CNT\ per\ sample}{Total\ CNT\ area\ available\ per\ sample}$$

N_{Si} and N_{CNT} have units of 1/length.

2-6.3 Glial Area Algorithm

A semi-automated thresholding algorithm combined with the binary mask generator developed by JHS was used to detect and measure glial cell area on either CNT or Si surfaces for individual FOVs. This algorithm measured total glial cell area per FOV and not the number of glial cells. Normalized total glial area for Si and CNT surfaces were defined as:

$$G_{Si} = \frac{Total\ glial\ area\ on\ silicon\ per\ sample}{Total\ silicon\ area\ available\ per\ sample}$$

$$G_{CNT} = \frac{Total\ glial\ area\ on\ CNT\ per\ sample}{Total\ CNT\ area\ available\ per\ sample}$$

G_{Si} and G_{CNT} are unitless.

2-6.4 Herding Parameters

In order to quantitatively compare the total neuron process and glial area between CNT and Si surfaces, neuron herding, N, glial herding, G, and total combined herding, GN, were defined as:

$$N = \frac{N_{CNT}}{N_{Si}+N_{CNT}} \qquad G = \frac{G_{Si}}{G_{CNT}+G_{Si}} \qquad GN = G \times N$$

N and G values greater than 0.5 indicate successfulness of a sample in guiding neuron processes and glial cells to the desired CNT or Si areas respectively. This means that for equal CNT and Si areas, more neuron processes existed on the CNT surface and more glial areas on Si surfaces respectively. GN was calculated to compare combined herding powers between various sample groups.

2-6.5 Statistical Analysis

The Kruskal-Wallis test for significance followed by post-hoc Dunn's test was used in MATLAB to compare the medians of neuron and glial parameters among different groups against various null hypotheses. The Kruskal-Wallis test is a nonparametric test with a nominal variable (for example the subgroups of the Euclidean geometry) and a measurement variable (e.g. N_{Si} or G_{Si}). This test unlike ANOVA does not assume normality for the measurement variable. If the Kruskal-Wallis test is performed to compare more than two nominal variables (two groups) and the results show the existence of a statistical significance, it cannot be determined which two variables are significantly different unless a post-hoc test is used to perform the pair-wise comparison. Dunn's multiple comparison test is a non-parametric post-hoc test that can be used after the Kruskal-Wallis on multiple variables to perform the pairwise comparison.

CHAPTER III

RETINAL NEURON AND GLIAL HERDING ON EUCLIDEAN ELECTRODES

Controlling cell behavior *in vitro* with the means of mechanical cues and surface patterning has long been studied.[107,108] This chapter focuses on using simple mechanical cues in the form of Euclidean geometries and understanding neuronal and glial behavior when exposed to those geometries. They consist of two different materials with distinct topography and stiffness properties with a micron-scale patterning. Specifically, the effects of nanoroughness and stiffness of CNT and Si surfaces on the adhesion, survival, growth and proliferation of mouse retinal neurons and glial cells was studied. We hypothesized that the smooth and stiff surface of the Si regions would attract and enhance glial adhesion and proliferation, while the rough and softer surface of CNTs would promote neuron adhesion and process outgrowth. Finally, the effects of culture length and variations in size of CNT and Si areas on the previously defined neuron and glia parameters were studied.

3-1. Visual Observations

Fluorescence microscopy and SEM images taken post-culture were used for qualitative observations of cell behavior on all geometries. This section focuses on describing the observed behavior. The hypotheses for explaining such behavior will be explained in the discussion section.

Neurons grew processes on both CNT electrodes and Si surfaces. The processes on CNT surfaces were longer and formed more complex networks. Neuron processes were more prevalent on CNTs than on Si and followed both the top and the bottom edges of the electrode upon reaching them. Neurons attached directly to the CNT top surface and survived for up to 17 DIV with no need for glial cell underlayers or proximity [Figure 3-1 a, b]. Larger clusters of cells were observed on Si surfaces [Figure 3-1 a]. These clusters were mostly accompanied by glial cell proliferations [Figure 3-1 c]. The processes bridged gaps and extended in 3 dimensions as was observed in other studies[97] [Figures 3-1 d and 3-2 a].

Glial cells preferred the gaps and did not proliferate on CNT surfaces at all culture durations. Glial proliferations did not bridge CNT rows. A variety of glial morphologies was observed [Figure 3-1 c]. A 25 μm Si width did not restrict glial proliferation. Inside narrow Si areas, glial cells assumed an elongated shape and oriented themselves along the rows [Figure 3-2 b]. Glia on CNTs were able to expand to the whole width of the CNT electrodes and were connected to glia and neurons within Si regions [Figure 3-2 c]. Glial cells that accompanied neurons and their processes on Si were located on the Si surface underneath the neurons [Figure 3-2 d].

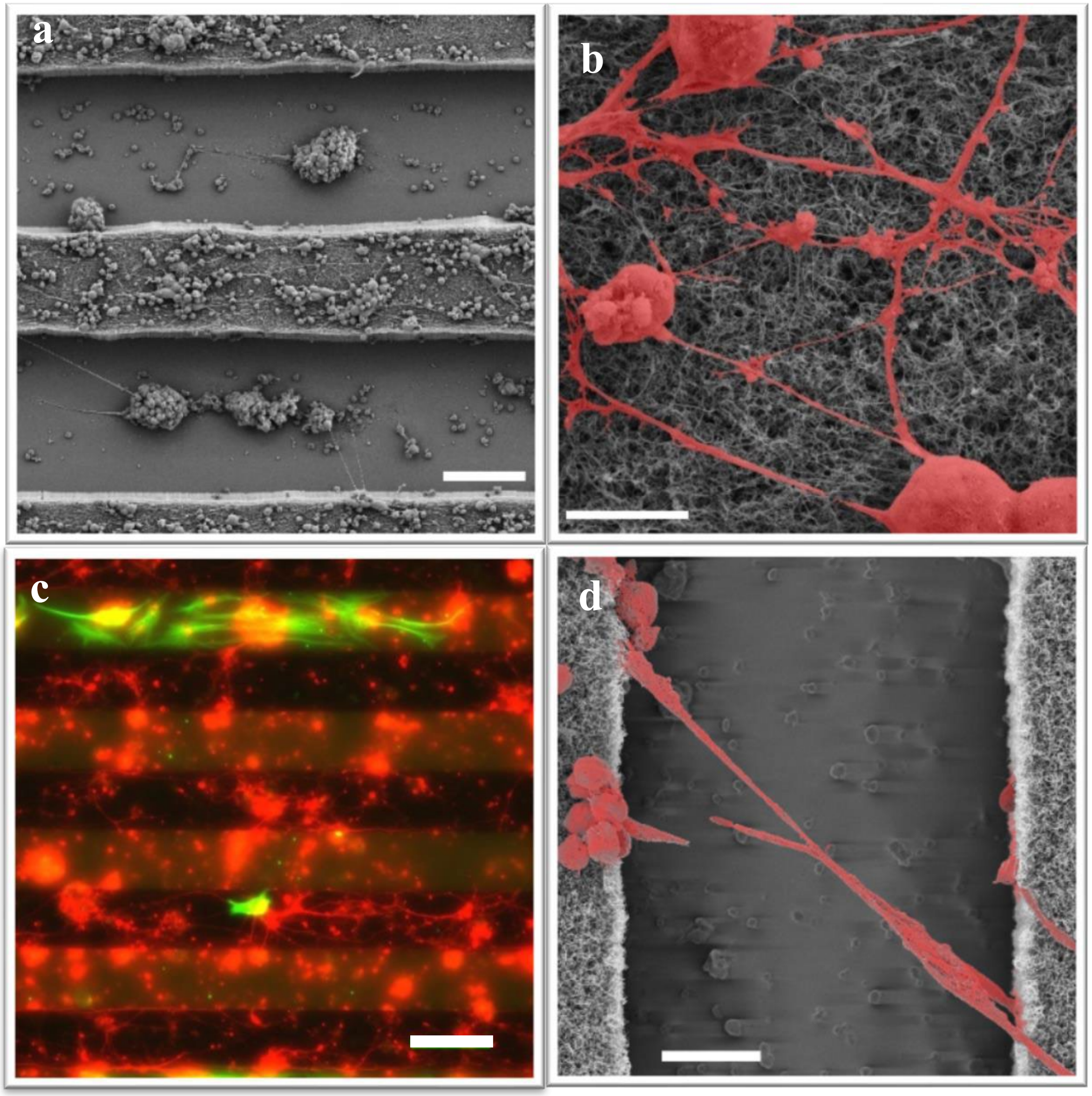

Figure 3-1. Examples of observations on Euclidean samples. a) SEM image of a R75 Euclidean geometry at 7 DIV showing neuron processes and cell clusters on CNTs and inside Si gaps. b) SEM image of a neural network on the top surface of CNTs (false-colored). c) Merged fluorescence images of glia (green) and neurons (red) on the CNT and Si rows of a R75 sample at 17 DIV showing an abundance of processes and smaller clusters on CNT surfaces compared to Si regions. Neuron processes followed the edges of the electrode without the presence of glia nearby inside the gaps. d) SEM image of a R50 sample at 7 DIV showing a neuron process bridging the gap (false-colored). Scale bars are 50, 5, 100 and 10 μm respectively.

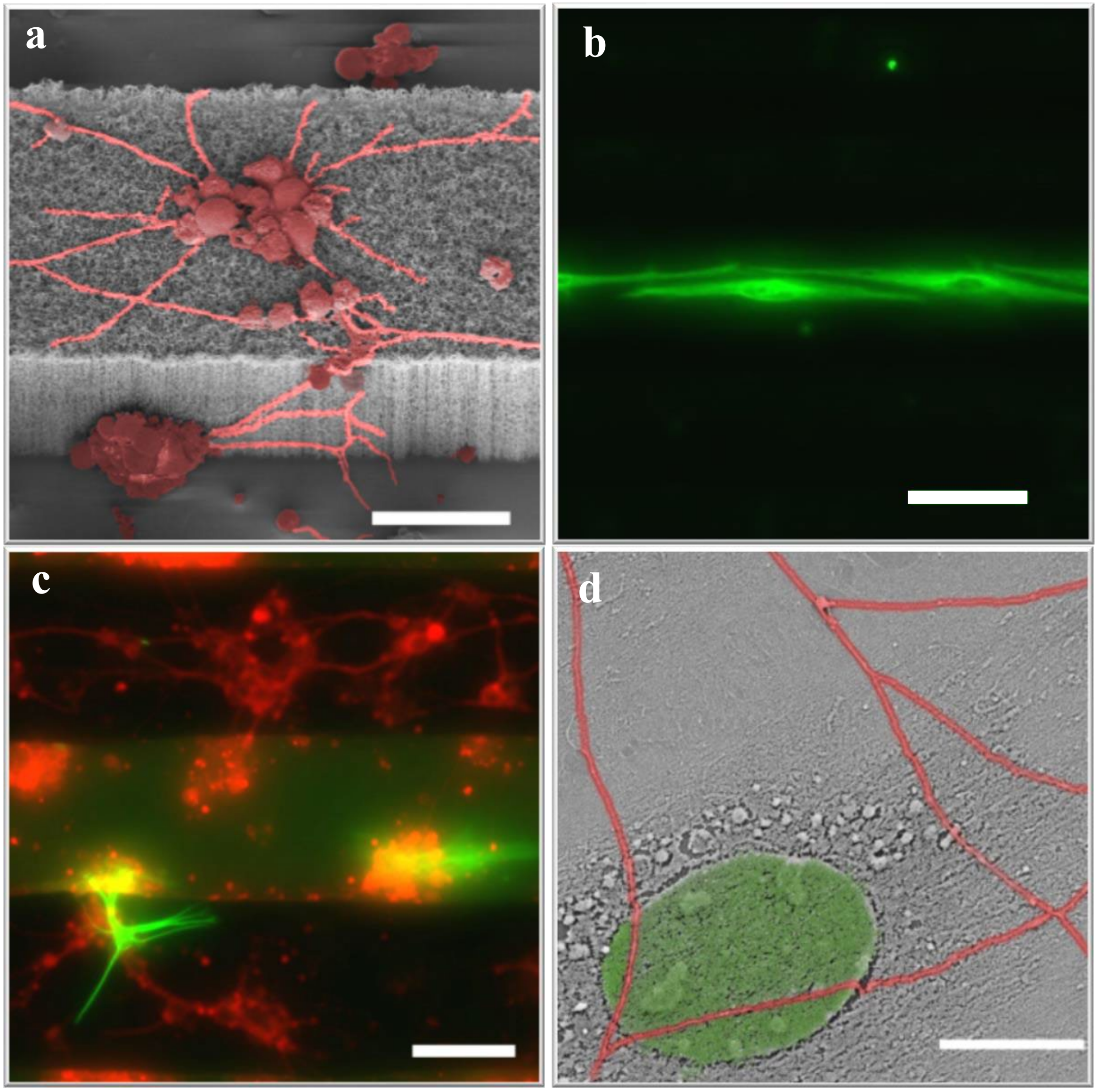

Figure 3-2. Examples of observations on Euclidean samples. a) SEM image of neuron clusters on the top and sidewalls of a 50 µm wide CNT row being connected to each other via several processes extending in 3 dimensions (false-colored). b) Fluorescence image of glial cells inside the gaps of a GR25 sample at 17 DIV. Glial cells proliferated inside the gap and had elongated morphologies. c) Merged fluorescence images of glia (green) and neurons (red) on CNT and Si rows of a R75 sample at 17 DIV showing a glial cell on the CNT top surface connected to another cell attached to the sidewall. d) SEM image of a glial cell body (false-colored green) and neuron processes (false-colored red) on the smooth Si surface. Neuron processes are located on top of the glial cell body. Scale bars are 20, 50, 50, and 10 µm respectively.

Time evolution of both neural networks and glial cells was visually studied. By day 3, neurons had already started aggregating on Si surfaces, forming clusters and growing processes connecting them. On CNT surfaces, mostly individual neurons with few processes expanding from their somas were observed. No glial proliferations were detected [Figure 3-3 a]. At 7 DIV, the number of clusters and their sizes increased on Si surfaces. On the CNT, processes were more prevalent and longer. Neuron aggregation into clusters was observed. Cells and clusters were mostly uniformly distributed. There were more and larger glial cells on both surfaces since more glial precursor cells have differentiated into full glial cells by 7 DIV (corresponding to a P10 retina Figure 2-7), but no glial proliferations were detected [Figure 3-3 b]. By 17 DIV, clusters inside Si were larger compared to 7 DIV. The largest clusters were seen together with glial proliferations. On CNT surfaces, neuron aggregation continued. The cell distribution uniformity was no longer the case. Individual neurons and clusters with processes were seen in regions where glial cells and proliferations on the Si surfaces took place [Figure 3-3 c].

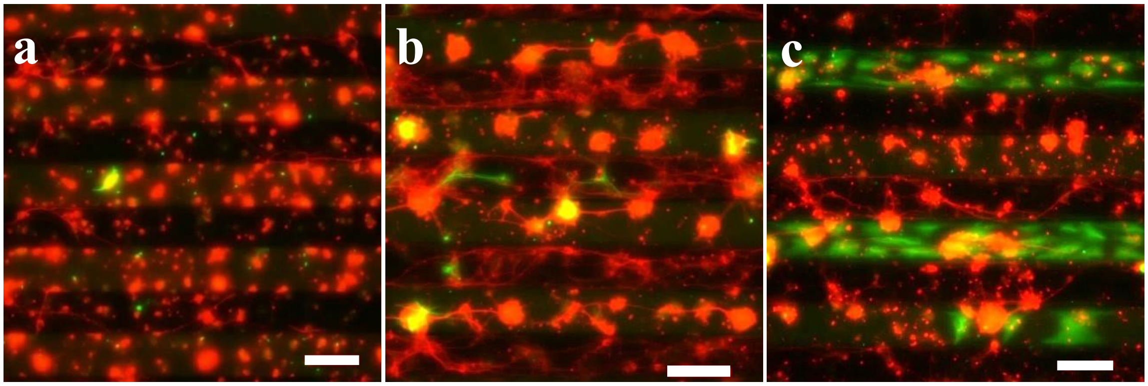

Figure 3-3. Fluorescence images of a R100 sample. Merged fluorescence images of neurons (red) and glial cells (green) at 3 DIV (a), 7 DIV and (b) 17 DIV. Scale bars are 100 μm.

3-2. Results

3-2.1. Neuron Process Edges Detection and Glial Proliferation

In order to quantify neuron processes following the edges of the CNT electrodes and glial cells proliferating inside the Si regions, the neuron process length and the glial area algorithms were applied to the fluorescence images of a few Euclidean samples to trace processes on both surfaces and detect glia inside Si regions [Figure 3-4 b, c]. The glial area and the process lengths were then summed along the direction of the rows [Figure 3-4 a, d] to assess the location of the peaks of the glial area plot with respect to gaps and the peaks of the process length plot with respect to the edges of the analyzed FOV. As an example, shown in Figure 3-4 a and b, the peaks of the glial area plot were located inside the Si gaps. We also observed that the peaks of total process length along the rows in Figure 3-4 d coincided with the edges of the electrode seen in Figure 3-4 c. Figure 3-4 e and f are zoom-in images of the marked areas in Figure 3-4 b and c.

3-2.2. Neuron and Glial Herding

The central intent behind performing dissociated retinal cell cultures on Euclidean geometries was to study and compare the effect of having two surfaces with distinct topographical characteristics on neuronal and glial development. It was predicted that the roughness of CNT surfaces would provide better support for neuronal attachment and process outgrowth compared to Si surfaces at all culture durations, while the smoother nature of the Si regions would enhance glial cell adhesion and proliferation in the vicinity of neurons. Approximately 90% of the samples successfully supported more neuronal growth on the CNTs and more glial proliferations inside the Si regions at all culture

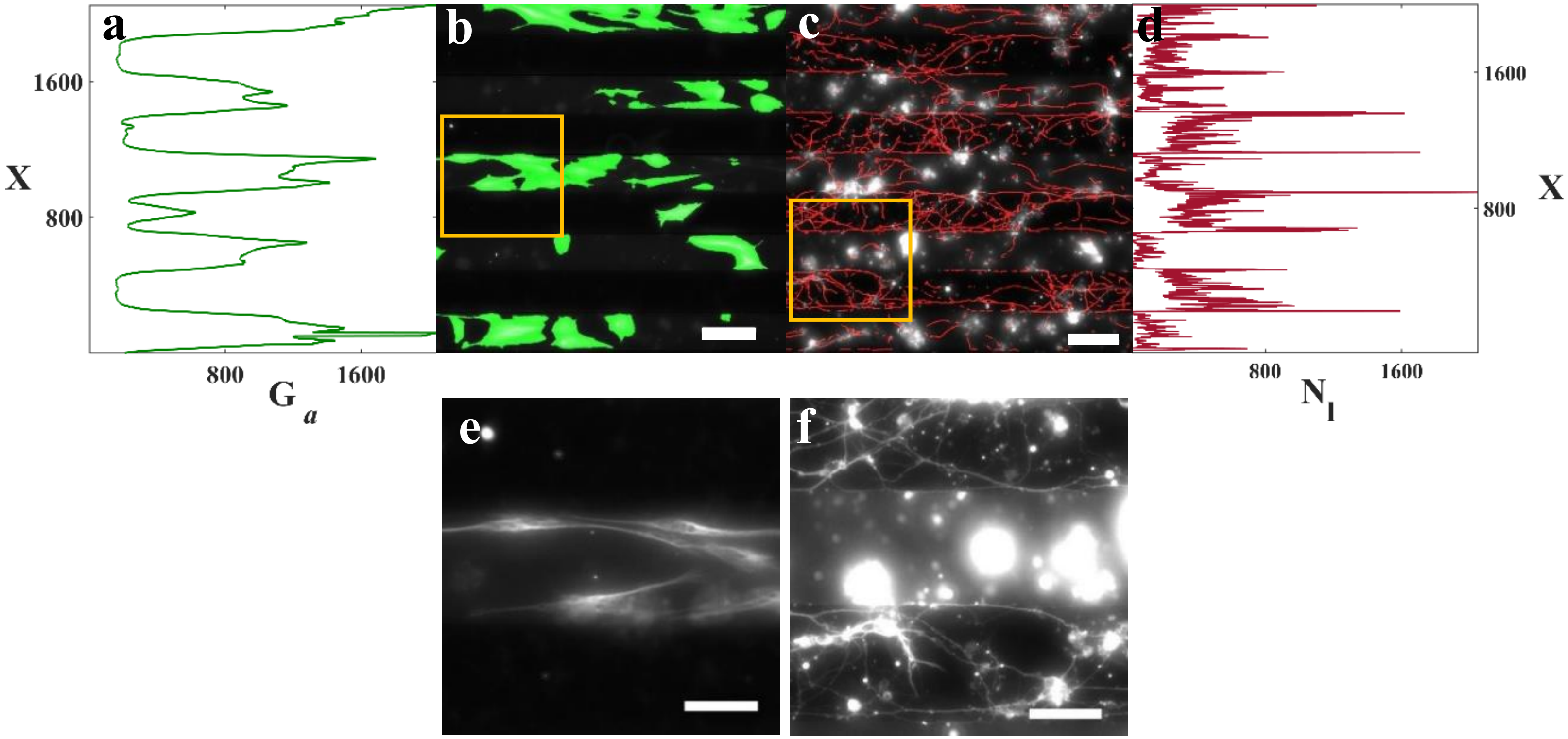

Figure 3-4. Example of quantification of neuron process edge detection and glial proliferation inside Si rows on a Euclidean sample. a) Sum of glial areas on both Si and CNT along the patterned rows seen in panel (b). Peaks representing maximum glial area were located inside the Si regions. b) Fluorescence image of glia (marked with GFAP and fluorescing green) overlapped with glial area algorithm results on Si and CNT surfaces for a GR75 Euclidean sample. c) Fluorescence image of neurons (marked with β-tubulin III) overlapped with the neuron process algorithm result marking processes in red. (b) and (c) show separate glia and neuron channels of the same FOV. d) Sum of process lengths along CNT and Si rows of the FOV seen in panel (c) with peaks coinciding with the edges of the rows. e) Zoom in of the marked area in (b). f) Zoom in of the marked area in (c). Scale bars are 100 µm in (b) and (c) and 50 µm in (e) and (f).

durations. Scatterplots of N_{CNT} vs N_{Si} [Figure 3-5 a] and G_{Si} vs G_{CNT} [Figure 3-5 b] agreed with the predictions. Samples above the solid black line in Figure 3-5 a and b, representing $N_{CNT} = N_{Si}$ and $G_{Si} = G_{CNT}$, were successful in guiding neurons and glial cells to the desired surfaces. The solid green, yellow and red fit lines corresponded to 3, 7 and 17 DIV datapoints respectively. The slopes of the fit lines in Figure 3-5 a were very close and no obvious difference in behavior of datapoints based on DIV was observed. The slope of the fit lines increased gradually from 3 DIV to 17 DIV in Figure 3-5 b showing a clear increase in glial area on Si vs CNT for longer culture times. Neuronal results obtained here confirmed previously observed preference of neurons for CNT rather than Si surfaces.[74,109]

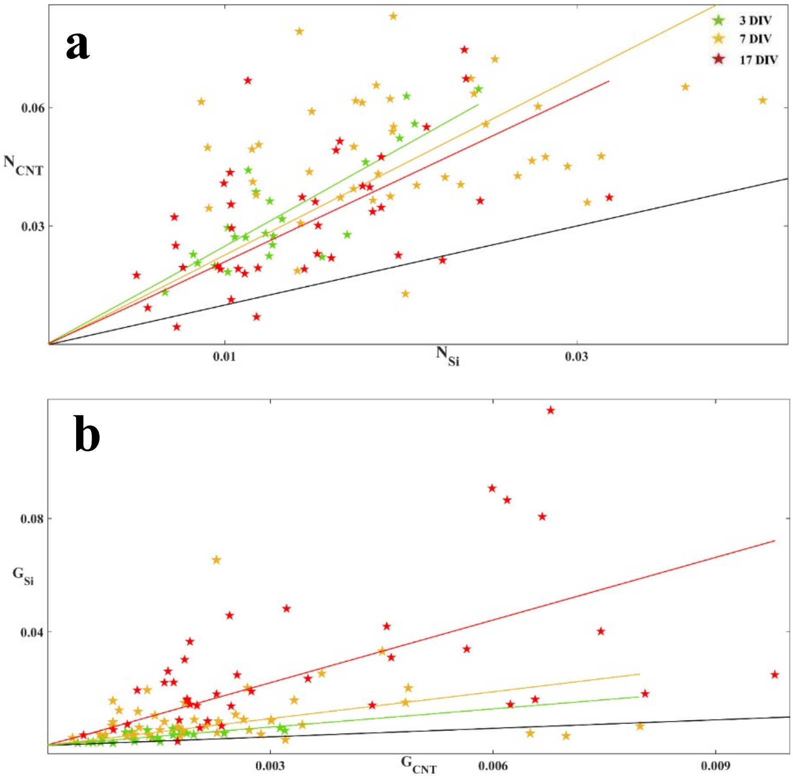

Figure 3-5. Neuron and glial herding onto CNT and Si regions. a) Scatterplot of N_{CNT} vs N_{Si} and b) Scatterplot of G_{Si} vs G_{CNT} for Euclidean samples colored based on culture time. The solid black line represents $N_{CNT} = N_{Si}$ and $G_{Si} = G_{CNT}$ in (a) and (b) respectively. The solid green, yellow and red fit lines are related to the datapoints of 3, 7 and 17 DIV respectively.

3-3. Statistical Analysis of Neuron and Glial Parameters on Euclidean Electrodes

3-3.1. Effect of Culture Time on Neuron and Glial Development

In order to study the effect of culture time on neuron and glial development, medians of neuron and glial parameters, N_{Si}, N_{CNT}, G_{Si} and G_{CNT} were calculated and plotted vs culture duration [Figure 3-5] for R and GR subgroups. Both N_{Si} and N_{CNT} increased from 3 DIV to 7 DIV, then decreased from 7 to 17 DIV for most subgroups [Figure 3-6 a, b]. The G_{Si} vs DIV plot showed a constant increase from 3 DIV to 17 DIV [Figure 3-6 c]. There was no consistent increase or decrease for G_{CNT} vs DIV [Figure 3-6 d].

Various geometries were tested via Kruskal-Wallis followed by Dunn's test against the null hypothesis that the culture duration should not affect N_{Si}, N_{CNT}, G_{Si} and G_{CNT}. For N_{Si}, the only significance was observed in R25 subgroup between 7 and 17 DIV with a P-Value = 0.023. Considering N_{CNT}, the significant pairs were:

R25 between 3 and 17 DIV with P-Value = 0.027

GR25 between 3 and 7 DIV with P-Value = 0.041

R100 between 3 and 7 DIV with P-Value = 0.040

R100 between 7 and 17 DIV with P-Value = 0.004

For G_{Si}, statistical tests showed significance between:

R50 between 3 and 17 DIV with P-Value = 0.008

GR50 between 3 and 17 DIV with P-Value = 0.030

R75 between 3 and 17 DIV with P-Value = 0.016

GR75 between 3 and 17 DIV with P-Value = 0.011

R100 between 3 and 17 DIV with P-Value = 0.003

No significance was observed for G_{CNT} between any of the subgroups.

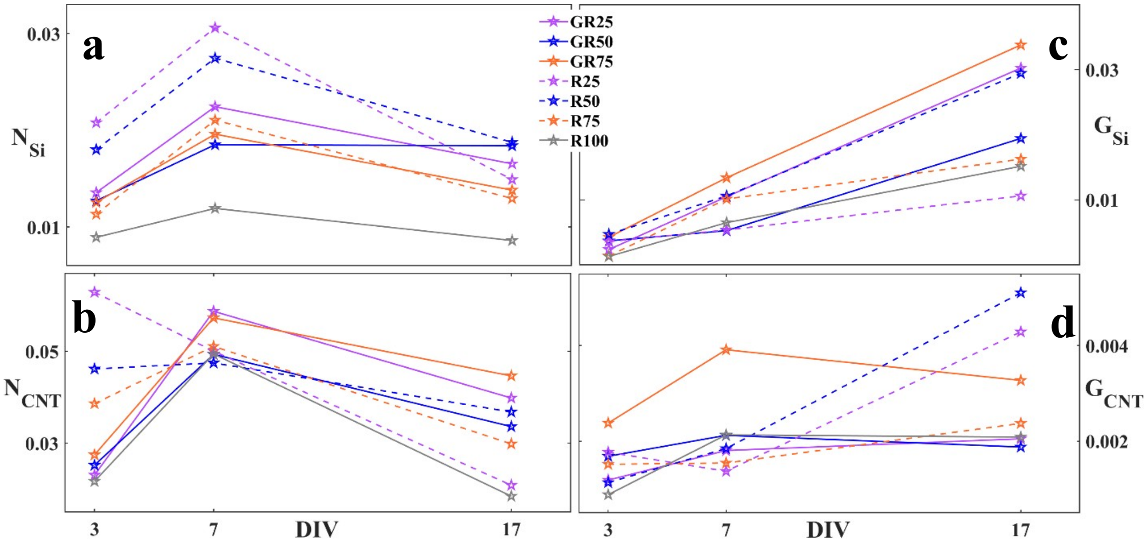

Figure 3-6. Neuron and glial parameters change with culture time. a) N_{Si}, b) N_{CNT}, c) G_{Si}, d) G_{CNT} median trends with DIV for R and GR subgroups. Error bars were not included for visual simplicity. Significant pairs were mentioned in the main text.

Performing longer cultures did increase the total glial area inside Si regions but did not have a significant effect on total process length on CNT and Si surfaces. The hypothesis explaining the rise and fall trend seen in N_{Si} and N_{CNT} vs DIV will be explained in the discussion section.

3-3.2. Effect of CNT and Si Width on Neuron and Glial Development

3-3.2.1. Group R

Samples in this group had the same CNT width and various Si widths. R subgroups were tested against the null hypothesis that Si width (W_{Si}) should not affect N_{CNT} and G_{CNT}. Results showing no statistical significance between any subgroups, confirmed the null hypothesis.

The subgroups were also tested against the null hypothesis that W_{Si} should not affect N_{Si} and G_{Si}. Results confirmed the null hypothesis for G_{Si} but rejected it for N_{Si}. Statistical significance was found between R25 vs R100 at both 3 and 7 DIV with P-Values = 0.013 and 0.006 respectively [Figure 3-7 a, b], and between R50 and R100 at 7 DIV with P-Value = 0.028 [Figure 3-7 b].

3-3.2.2. Group GR

GR subgroups were tested against the same null hypotheses mentioned in section 3-3.2.1. Results for N_{CNT}, G_{CNT} and G_{Si} showed no statistical significance between any GR subgroups compared at the same DIV. For N_{Si}, there was statistical significance between GR25 vs GR100 at 7 DIV with P-Value = 0.046 [Figure 3-7 e].

In summary, changing the CNT width at each DIV did not significantly affect neuronal or glial growth. Changing the Si width made differences in process growth when comparing the largest to the two narrowest W_{Si} subgroups (R100 against GR25, R25 and R50).

Figure 3-7 summarizes the effect of geometrical properties on N_{Si} in the R and GR groups. Although there was no statistical significance between most subgroups at each DIV, a mild declining trend with the increase in W_{Si} was observed at each DIV.

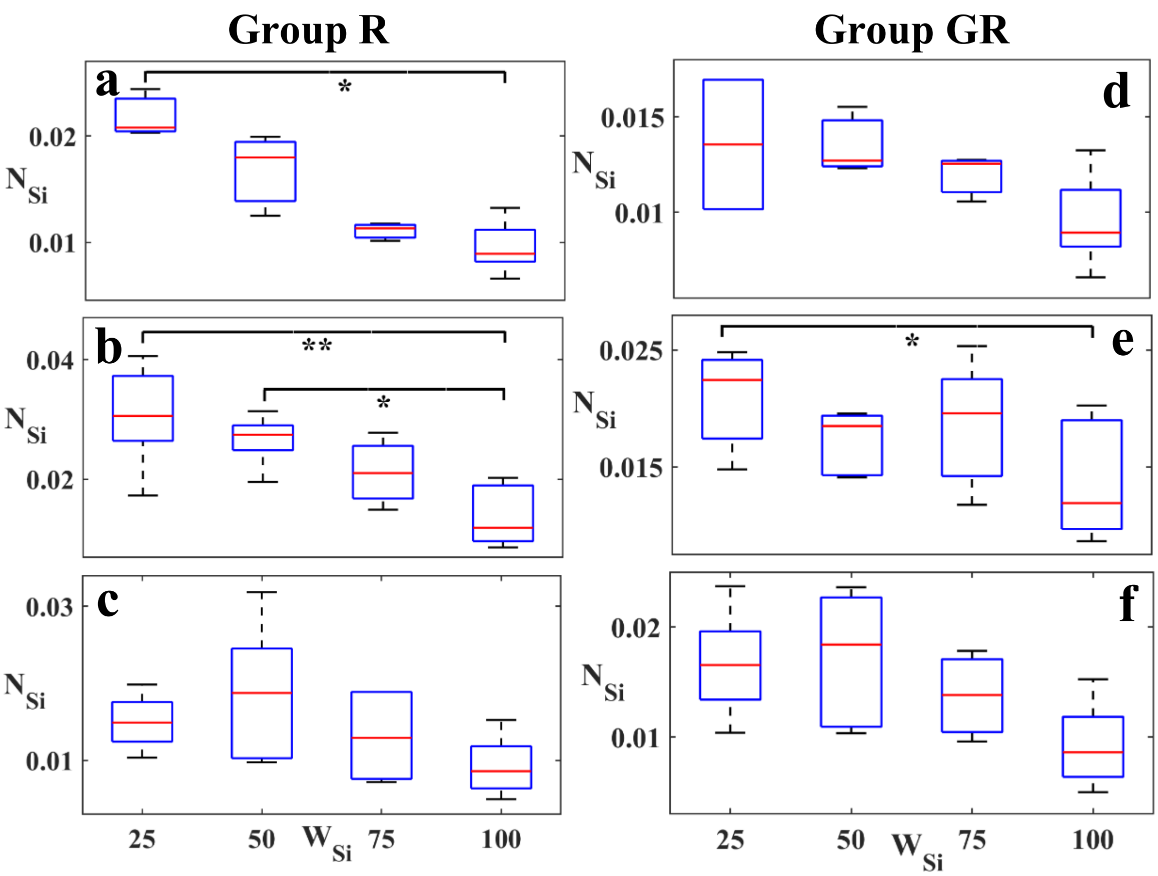

Figure 3-7. Boxplots of N_{Si} vs W_{Si} for groups R (left column) and GR (right column) at a) and d) 3 DIV, b) and e) 7 DIV and c) and f) 17 DIV. The solid black lines point to subgroups that have statistically significant N_{Si} median values. Stars determine degree of significance. * denotes $0.01 < P \leq 0.05$ and ** denotes $0.001 < P \leq 0.01$.

3-4. Discussion

This section is an approach to the explanation of the hypotheses behind the observed behavior of neurons and glia on various surface types and a review of the studies that support those hypotheses.

3-4.1. Neuron Processes Are More Prevalent on CNT Surfaces and Survive Without Glial Cell Proximity

In the past two decades, researchers have used various preparations of CNTs as a substrate for neuronal adhesion and growth.[70] They claimed that the nano-roughness of the CNT surface mimics the properties of the extracellular matrix (ECM)[69] and enhances neurite outgrowth and elongation if the degree of roughness matches the diameter of neuron processes.[74] Figure 3-8 shows a post-culture SEM image of a neuron process entangled with the tubes on the CNT top surface.

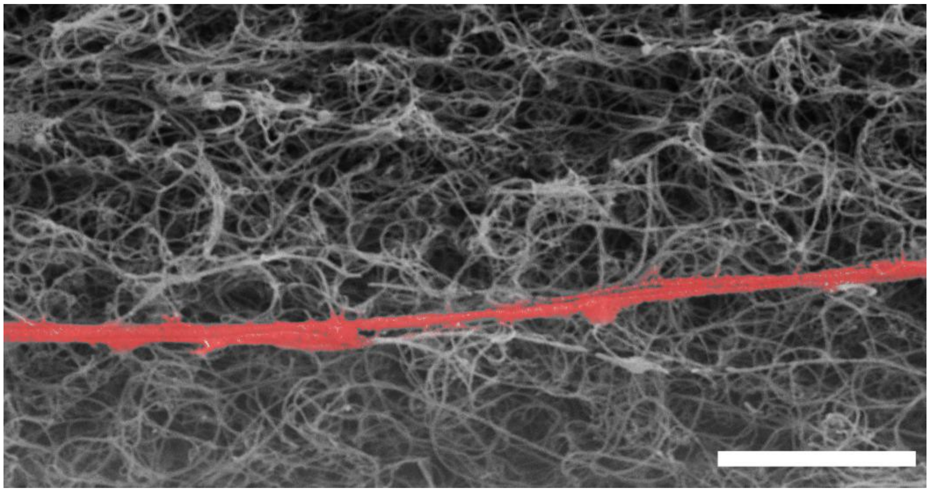

Figure 3-8. Post-culture SEM image of a neuron process on the CNT top surface entangled with the nanotubes. Scale bar is 2 μm.

Neurons are anchorage dependent cells. Their survival and development depend on their adhesion strength to the substrate. Their processes can detect the nano-topography and flexibility of the surface with their growth cones (structures at the tip of the process responsible for navigating the environment and pathfinding) and respond accordingly.[89] Multiple studies have concluded that neurons have the ability to detect differences in geometry, roughness and rigidity of their environment and respond accordingly in different ways such as improved adhesion, directional guidance and outgrowth of processes and accelerated process growth.[110] In addition, substrates with a range of nanoroughness or nanoporosity detectable by the filopodia[111] - finger like structures containing bundles of the protein F-actin in the growth cone that extend for a few microns- would improve neuron adhesion and development through completely mechanical rather than chemical interactions.[62,112,113] Other studies have shown that neurons *in vitro* prefer to adhere and grow more branched processes on soft substrates.[114,115] The CNT surface provided both suitable roughness and appropriate stiffness features. Flexibility of CNTs is a function of their length. Our synthesized CNTs were tall enough to provide a suitable rough and flexible surface similar to *in vivo* conditions for the neurons.[89] CNTs used in these experiments were not functionalized and yet they supported impressive neuronal adhesion and outgrowth. These results contradicted several other early studies that concluded some kind of functionalization would be necessary to increase CNT biocompatibility for neuronal support.[84] However, other studies have confirmed biocompatibility of pristine CNTs for neural network survival and stimulation.[116] The CNT biocompatibility in these experiments has increased due to the encapsulation of toxic catalyst nanoparticles within the tubes and the presence of the Al adhesive layer that prevented CNT delamination from the substrate and its diffusion and agglomeration in the culture medium.

The survival of neurons on CNT surfaces without glial cell mediation observed in our experiments confirms previously obtained results. Several studies showed that neurons were able to survive without glial cells on certain substrate types. Georges et al. showed that neurons from E17-E19 rat embryos survived and grew independently of glial cells on soft substrates[58] In another study by Sorkin et al. , it was observed that cortical neurons from rat embryos attached directly to the CNT top surface without the mediating glial underlayer. [44,74]

3-4.2. There Are Larger Clusters on Si Surfaces

In the dissociated retinal cell cultures sections of chapter II, it was mentioned that the cell suspension was passed through a 40 µm cell strainer to get rid of very large cell clusters before seeding the samples. In SEM and fluorescence images taken at 17 DIV, clusters existed on both CNT and Si surfaces that were larger than 40 µm. This confirmed that cells on both surfaces were motile and aggregated into clusters or joined already existing ones. The phenomenon observed here is the initial step towards the formation of a neural network *in vitro* that is not random and in fact is governed by rules of a small-world network formation to maximize the systems overall efficiency[117,118] and avoid unnecessary costs.

Various previous studies showed that frontal ganglion neurons of adult locusts[119] and retinal ganglion cells (RGCs) from postnatal 7 BALB/c mice[120,121] form small-world networks on a flat surface *in vitro*. RGCs from PN7 mice seeded on tethered lipid bilayers coated with extracellular matrix proteins started extending processes looking for neighboring cells 19 to 23 hours after being seeded. Networks were rarely observed at the beginning. Cells started extending new processes as the culture went on. After 30 to 36 hours, the network reached a maximal complexity state, i.e. it had a maximum number of nodes (clusters and individual cells) and links (neuron processes) between nodes. There was no self-avoidance at this stage. When the maximal complexity stage was completed, network optimization was the dominant process in shaping the connections within the network through the pruning process and the fact that cells gradually preferred neuron-neuron interactions to the initial neuron-substrate interactions.[122] The number of nodes and links connecting them decreased through several procedures. Some processes joined together and formed thick bundles and weaker or unnecessary processes were eliminated to fine tune the wiring of the network.[123] As the network optimization went on, the largest clusters increased their sizes while the second largest started to get absorbed into the largest ones (elimination of nodes). Neuron processes were straightened between the strong focal adhesion points and clusters.[124] The network reached the optimized state after 41 h. The optimization procedure happened at a faster rate for RGC of mice compared to locust ganglion cells [4 to 5 days].

Tension forces generated along the processes that connect neighboring neurons are responsible for cell motility, aggregation and the morphology of the neural network developed.[121] If these tension forces are stronger than cell-substrate adhesion forces, the cells start moving towards each other along the processes connecting them and aggregate into clusters. Flat Si is an atomically smooth surface with no chemical functionalization for enhancing cell adhesion. Tension forces along processes may be stronger than cell-substrate adhesion forces at least at the beginning of the culture. Figure 3-9 schematically shows the evolution of a neural network from maximal complexity to an optimized state. In Figure 3-9 a, all nodes, i.e. cell clusters and individual neurons are connected to each other at the maximal complexity stage around 7 DIV. The smaller cluster consisting of two cells experiences a net force to the right since the cell-cell interactions overcome cell-substrate adhesion. The cell-substrate adhesion acts like a frictional force in the opposite direction to the motion of the cell. In Figure 3-9 b, sometime between 7 and 17 DIV, the small cluster moves in between the individual cell and the large cluster, meanwhile the processes connecting the nodes would straighten between them and therefore become shorter. In the final state observed in Figure 3-9 c at 17 DIV, the small cluster joins the larger one, losing the processes between them. Assuming the individual cell is strongly bound to the substrate, it stays stationary and potentially sends its process in other directions looking for other neighboring cells.

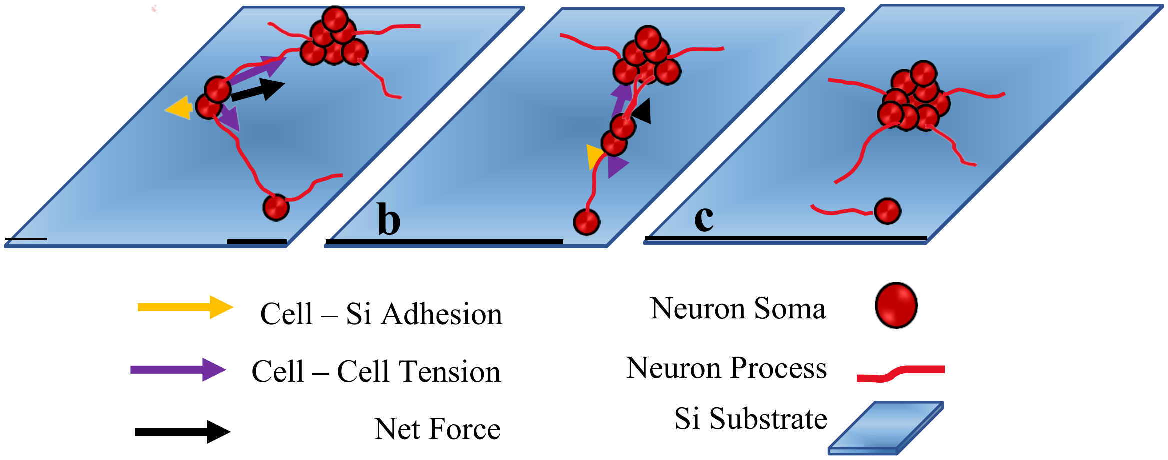

Figure 3-9. Schematic of a small-world network forming on a smooth unpatterned surface. a) Maximal complexity network around 7 DIV. b) Optimization process towards small-world network starts after 7 DIV. c) Small-world network formed.

Although the parameters of a small-world network were never directly studied in these experiments, it was hypothesized that larger clusters observed on Si were the result of the small-world network formation process.

Assuming that the same network formation process occurs on a substrate with some degree of roughness, e.g. the top surface of CNTs[125], and knowing that neurons can also aggregate on CNT surfaces[122], it was observed that the neural networks formed on CNT surfaces had larger numbers of nodes and links between them at the same DIV as the Si surfaces. The hypothesis is that cell-CNT adhesion forces are stronger than cell-Si adhesion forces and resist more against cell-cell interactions through tension forces along the processes connecting them.[126] This would result in lower motility and slower aggregation rates for cells on CNT surfaces. Therefore, the optimization rate of the network would be slower resulting in more medium to small clusters and individual cells and more processes connecting them on CNT surfaces.

Although adhesion forces between retinal cells and Si or CNT surfaces were never directly measured in these experiments, there are multiple studies that support the hypothesis of stronger adhesion forces between CNT surfaces and cells. Chen et al. in their studies of VACNT forests with curly entangled end segments at the top (similar to the CNTs synthesized for these experiments) showed that shear adhesion forces were several times larger than the corresponding normal forces for nanotubes with lengths above 10 μm.[127] In another analysis, Machado et al. claimed that VACNTs soaked in culture medium would prevent cells from slipping and force them to remain in their locations regardless of the hydrophobicity of the surface.[128] The surface roughness would increase the contact area between the cell membrane and the surface and hence increase the adhesion force exerted on the cell.[125] The hypothesis is that tension forces along processes on CNTs had to overcome the large shear adhesion forces of the top entangled CNTs so that the cells would gain enough motility and start aggregating to form larger clusters. In addition to the argument above, multiple studies have directly measured cell migration speeds on surfaces with nano-roughness and showed that cell motility decreases on these surfaces compared to surfaces without the nanoroughness.[129,130,131]

The rise and fall observed in N_{Si} and N_{CNT} vs DIV seen in Figure 3-6 a and b could be explained using the hypothesis derived from small-world network formation. It was previously mentioned that at 3 DIV, retinal cells on both surfaces have extended processes and formed some clusters (equivalent to the timeline of 19-23 hours after culturing PN7 RGCs in previous studies).[120] By 7 DIV, in most of the subgroups, neural networks on both surfaces have reached maximal complexity with no self-avoidance ensuring the largest normalized process lengths. The pruning and network optimization process takes place afterwards. Therefore, the peaks observed at 7 DIV for both N_{Si} and N_{CNT} correspond to the maximal connectivity stage and the depletion seen by 17 DIV is the result of pruning processes explained previously. Due to the fact that retinal cells from mice at younger ages were cultured on patterned materials with two different degrees of roughness and not on uniform unpatterned surfaces, it cannot be assumed that by 17 DIV the neural networks on both CNT and Si have reached their final optimized state. Longer cultures would be needed to confirm or deny this hypothesis.

3-4.3. Neuron Processes Follow the Edges of the Electrodes Upon Reaching Them

It's been known for decades that cells and specifically neurons respond to topographical and mechanical cues present in their environment.[107] Substrates with both small and large feature sizes can provide guidance cues for neuron processes.[132] In one study, Roberts et al. observed that processes of embryonic rat motor neurons follow the edges of horizontally aligned CNTs due to the existence of micron-scale steps between the flat SiO_2 and the CNTs.[96] In another study by Zhang et al., neuron processes from the H19-7 cell line derived from embryonic rat hippocampi, followed the edges of functionalized

VACNTs. They argued that the diffusion and trapping of hydrophilic poly-L-lysine (PLL) into the edges of the tall CNT patterns due to capillary action attracted neuron processes.[89] In addition, preliminary results prior to this research, of culturing mouse P4 retinal neurons on SU8 zigzag line patterns with width and height equal to 2 μm and 70° turning angles functionalized with fibronectin, showed that neuron processes that were generated from somas close to the lines were able to detect, follow and make turns at corners of the patterns. Figure 3-10 shows such an instance. Neuron processes generated from the soma on the pattern follow the lines and make 70° turns while processes from the soma on the flat substrate weave through the 2D space.

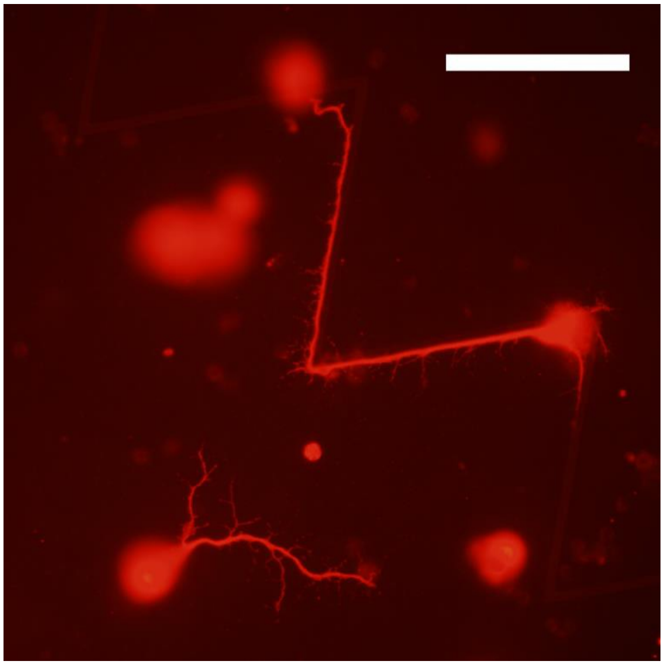

Figure 3-10. Fluorescence microscopy image of two neurons close to and away from SU8 zigzag lines. The process generated from the soma on the pattern follows the line, while the ones from the other cell away from the pattern weave on the substrate. Scale bar is 50 μm.

Despite all the efforts made to explain this behavior, the reasons and mechanisms of neuron processes following mechanical cues is not fully understood. Three hypotheses were represented to explain why neurons follow the edges of the electrodes.

Hypothesis 1: Neuron processes on the CNT top surface would reach the edges and follow them only if they receive chemical cues of the presence of a glial cell inside the Si region in their vicinity.

This hypothesis was declined based on multiple observation of fluorescence images where a process followed the edge of the electrode without the presence of glial cells in the vicinity [Figures 3-1 c and 3-4 f].

Hypothesis 2: Neuron processes follow the edges of the electrodes due to the curvature they face at the edge. Previous studies by Smeal et al. showed that neuron processes from postnatal dorsal root ganglion (DRG) cells align themselves with the direction of minimum principle curvature on substrates and favor paths that would minimize their bending.[133] In a following study, it was shown that the effect of substrate curvature on the direction of neuron processes can vary based on the age or type of the neurons under study.[134] In our studies, it was observed that neuron processes that originated from a soma located on CNT top surface and away from CNT edges, followed the CNT edge upon reaching it. It was hypothesized that when they faced a curvature (a 90° turn) in their path, like DRG cell processes, they favored paths that minimized their bending, and therefore instead of climbing down the sidewalls, they aligned themselves with the edges of the CNTs.

Hypothesis 3: The difference in texture and degree of roughness between the top and sidewalls of the CNTs causes the neuron processes to follow the edges. The top surface rms roughness is closer to the roughness of the ECM. This hypothesis is yet to be tested. Measurements of the rms roughness of the top and side surfaces and comparing them to the roughness of the ECM proteins could either confirm or deny this hypothesis.

In conclusion a combination of these hypotheses besides other factors yet to be discovered may cause this behavior of neuron processes.

3-4.4. Glial Cells Prefer to Adhere and Proliferate Inside Si Regions and Do Not Proliferate on the CNT Electrodes

Glial cells in contrast to neurons can proliferate throughout their lifetime. It has been shown that Si can induce significant glial scar tissue formation.[135,136] Glial cell adhesion, motility and proliferation are dependent on the degree of roughness and stiffness of the environment. Their motility is reduced on the rougher CNT surface compared to the smooth, stiffer Si. Glial proliferation and motility go hand in hand. Glia on CNT surfaces did not proliferate because of their reduced motility. This hypothesis was supported by several previous studies. It was previously shown by Georges et al. that when culturing glial cells from prenatal E17-E18 rat embryos on gels with various degrees of stiffness, glial proliferation was decreased on softer substrates due to weaker adhesions.[58] In another study by McKenzie et al., rat glial cells were cultured on multiwalled carbon nanofiber substrates and it was shown that glial proliferation was decreased on carbon nanofibers.[137] Persson et al. showed that fibroblasts cultured on GaP nanowires had reduced cell motility and proliferation.[131] Additionally, it was shown that PEDOT/MWCNT coated implants reduce inflammatory response compared to platinum implants.[93]

3-4.5. Various Glial Morphologies Were Observed

Different morphologies observed in glial proliferation sites within Si regions could be related to cell type. *In vitro*, both Müller cells and astrocytes express GFAP and they are not easily distinguished from each other.[65] The presence of dispersed CNTs in the medium during culture could also affect the degree of maturation and proliferation state of the cells. It has been shown by Gottipati et al. that adding water-soluble functionalized carbon nanotubes to the culture medium of brain glial cells affected their degree of maturation and morphology.[138]

3-4.6. On Si Surfaces, Glial Cells Were Detected Underneath Neurons and Their Processes

It was previously discussed that neurons have a preference to adhere to and grow on soft substrates. Therefore, the stiff Si surface is not a desirable environment for them. It was also mentioned that glial cells, on the other hand, preferred adhesion to stiffer substrates such as Si.[58,139] In addition, glial cells are twice as soft as neurons[140,141] and softer than the Si substrate. Although glial proliferations appeared much later than neuron clusters and processes in cultures, in order to protect neurons from the stiff Si, they lifted the processes and created a layer between the Si surface and the neurons. As a reminder, one role of glial cells among many others is to ensheath neurons and their processes. This, plus the fact that large clusters of the small-world networks on Si were always accompanied by glial proliferations, clearly showed that they played a crucial role in forming those networks via guiding neuronal migration along glial fibers.[142] In contrast, other studies have shown that clusters in engineered neural networks through substrate patterning were self-preserved without the presence of glial cells for up to 11 weeks in the presence of CNT islands.[109]

3-5. Conclusion

The use of mechanical cues such as micron-scale geometric patterning combined with alterations in nanotopography and stiffness of the materials is a permanent solution for guiding various cell types into separate yet neighboring desired regions on a substrate. Here, using a system of micron-sized patterns of rows of nanorough and flexible CNTs separated by smooth and stiff Si regions, dissociated mouse retinal neurons and glial cells were cultured for up to 17 DIV and were guided to adhere and grow on their desired environments while keeping close contact between them since the presence of glial cells is essential for neuronal survival and synaptic efficacy even *in vitro*.[143,144] By calculating normalized neuron process length and normalized glial area, it was quantitatively shown that neurons and glia would prefer rough CNT surfaces and smooth Si surfaces respectively at all culture durations. It was also discussed that neural networks on both surfaces had visual characteristics similar to a small-world network and were formed following a certain set of rules. Herding results obtained here confirmed previously observed neuron-glia separation on rows of randomly distributed vertical GaP nanowires separated by smooth GaP areas.[60] Although the nanotopography and chemical characteristics of the CNTs were quite different from the nanowires, the same neuronal and glial behavior was observed suggesting that the textured versus smooth surfaces played the main role in cell separation and not the chemical properties of the materials used.

CHAPTER IV

A COMARISON OF FRACTAL AND EUCLIDEAN GEOMETRIES FOR RETINAL NEURON AND GLIAL CELL HERDING

In the previous chapter, it was shown that by patterning two materials with different topographical characteristics using a simple Euclidean geometry, one can achieve spatial separation of the retinal neurons and glial cells. These simple Euclidean electrodes were disconnected from each other, making it difficult for cells that landed on one region to migrate and communicate with cells from other regions. Therefore, designing a geometric pattern that maintains or further improves the separation between neurons and glia and at the same time provides a continuous space for cell interactions is desirable.

Fractal geometries, specifically H-trees in this work, provide the desired features. Besides providing a continuous CNT electrode surrounded by smooth surfaces, they increase the number of CNT edges within a given bounding area for neuron processes to follow and also contain interconnected Si regions that potentially could enhance glial proliferation.

This chapter studies the effect of the geometric properties of fractals on neuron and glial herding that were cultured for 17 DIV. First, fractal electrodes with different D values and numbers of iterations are studied. Second, a comparison between all fractal electrodes and the 17 DIV Euclidean data is made to show that the fractal characteristics enhance the effect of geometry on herding neurons and glial cells. And finally, fractals are compared to all DIV Euclidean data to observe the time evolution of the system.

4-1. Visual Observations on Fractal Electrodes

Qualitative observations of fluorescence microscopy images of the fractal samples confirmed the basic results obtained on the Euclidean ones. Below is a brief summary:

On the CNT branches of the fractal electrodes, individual neurons and clusters grew processes that followed the edges of the electrodes and made 90° turns at branch junctions. In the Si regions close to the electrode branches, small to medium-sized clusters with processes connecting them were observed together with occasional glial proliferations. In the Si regions further away from CNT electrodes, neurons aggregated into large clusters accompanied by glial proliferations. These clusters were connected through thick bundles of processes (i.e. a small-world network as described in chapter III). Furthest away from the electrodes, regions devoid of cell clusters or individual ones with weak processes were seen, similar to previous observations by Piret et al.[145] [Figure 4-1 a]

As the D value and number of iterations of the fractals increased, the small-world neural networks accompanied by glial proliferations were formed closer to the electrodes. These observations agreed with the results of a study performed by Shein et al. showing that neurons and glia migrated towards CNT electrodes and formed clusters around them that were connected through bundles of processes.[44] This phenomenon increased the probability of forming connections between neurons on the Si and those on the CNT surfaces [Figure 4-1 b, c, d]. As seen in Figure 4-1 b, the 1.1 fractal electrode produced minimal connections between the neural network on Si to neurons on CNT was observed for a small-world network on the Si region and the neurons on the CNTs. For the 2-5 and 2-6 fractal electrodes, clusters were observed closer to CNT branches [Figure 4-1 c, d] and extended more processes towards the CNT electrodes.

On lower D fractals, vast areas with minimal to zero cell aggregation and no glial proliferation were observed [Figure 4-2 a]. As D and the number of iterations increased, these areas became smaller and eventually vanished for the 2-5 and 2-6 fractals [Figure 4-1 c, d].

Glial cells on the CNT electrodes elongated themselves along the narrow branches and were not restricted by 90° turning angles [Figure 4-2 b].

A few fractal samples were cultured at 7 DIV. The glial distribution on these samples was uniform and no proliferation was detected [Figure 4-2 c]. At 17 DIV, glial proliferations were observed on all fractal geometries. On the lower D fractals, the glia were located close to the CNT electrode branches. Glial proliferations were able to penetrate the smallest Si regions for all fractal electrodes. As D and the number of iterations increased, the glial proliferation distribution became more uniform. The 2-6 fractals were an exception. Glial proliferations were more restricted on these geometries because of the loss of interconnected Si regions [Figure 4-2 d].

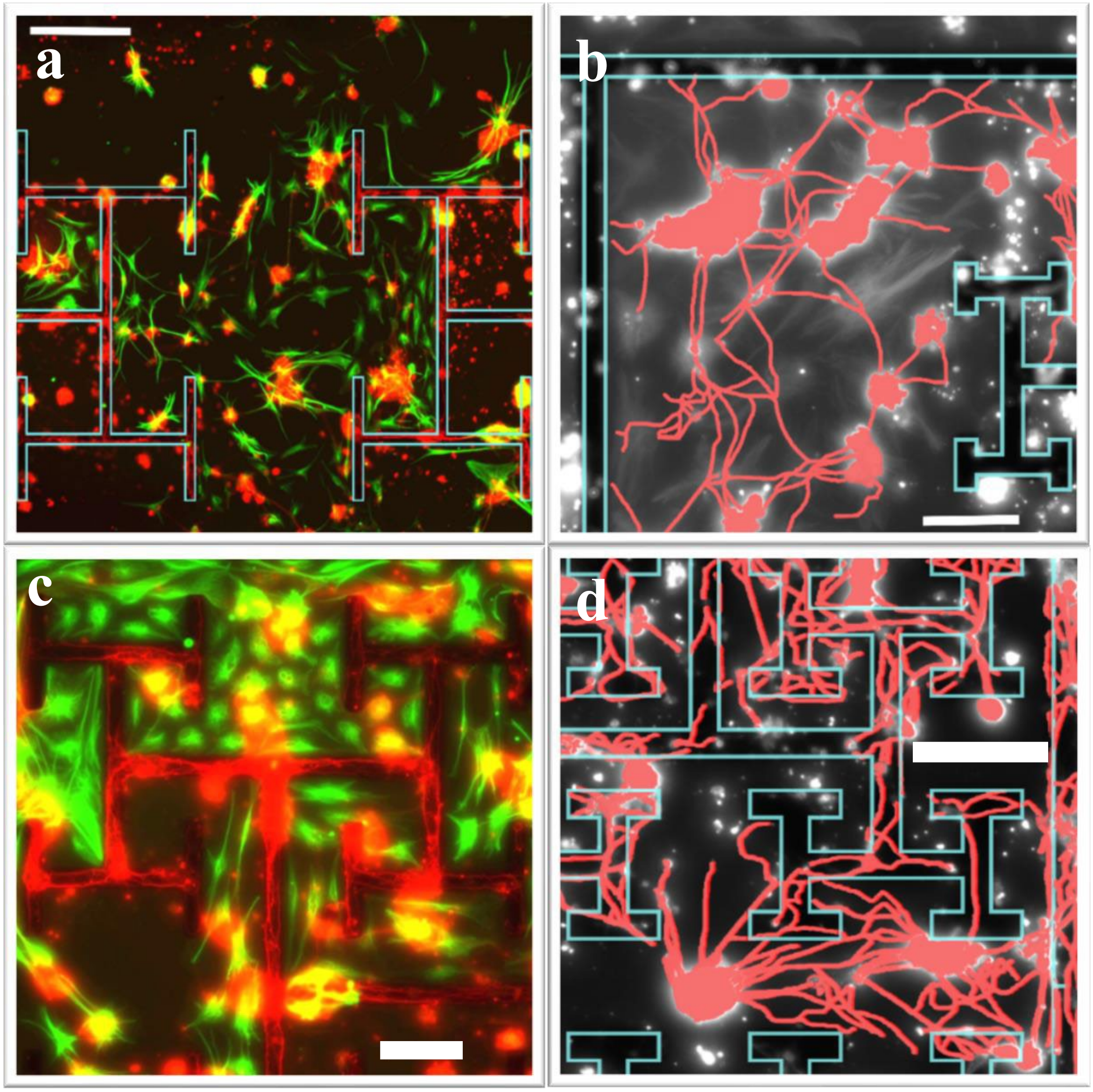

Figure 4-1. Examples of visual observations of fractal samples. (a) Merged fluorescence images of glia (green) and neurons (red) for a region on a 2-4 fractal. b) Fluorescence image of neuron clusters and processes (false-colored in red) showing the existence of a small-world network on Si close to the electrode branches of a 1.1 fractal. c) Merged fluorescence image of (green) glia and neurons (red) for a 2-5 fractal showing the small-world network region on Si close to the electrode branches and its connections to neurons on the electrodes. d) Fluorescence image of neuron clusters and processes (false-colored in red) showing the existence of a small-world network region on Si close to the electrode branches and its interactions with the neural network on CNT electrodes on a 2-6 fractal. Scale bars for (a) and (b) are 200 μm, and on (c) and (d) are 100 μm. The CNT electrode boundaries are shown in blue in (a), (b) and (d).

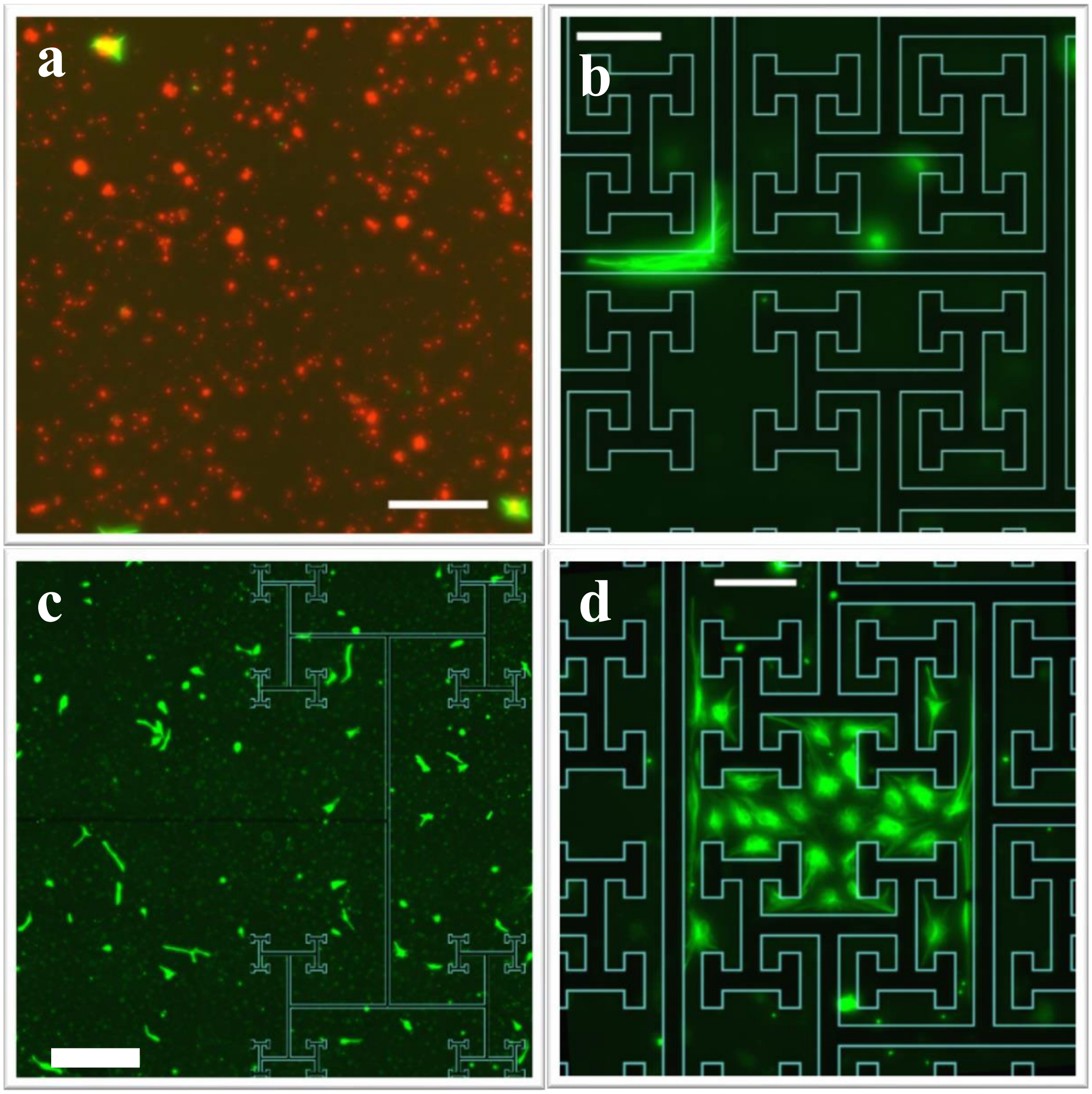

Figure 4-2. Examples of visual observations of fractal samples. a) Merged fluorescence images of glia (green) and neurons (red) showing a region on a 1.1 fractal away from the CNT electrodes supporting few glial cells and few neuron clusters and processes. b) Fluorescence image of a glial cell on the CNT branches of a 2-6 fractal electrode. The individual glia stretched along the branch and made a 90° turn. c) Fluorescence image of a glial cell distribution on a 1.1 fractal at 7 DIV. No glial proliferation and no small-world network were observed. d) Fluorescence image of a glial proliferation site in a Si interconnected area between the branches of a 2-6 fractal electrode. Scale bars on (a) and (c) are 200 µm and 500 µm respectively, and on (b) and (d) are 100 µm. The CNT electrode boundaries were shown in blue in (b), (c) and (d).

Summarizing the above visual observations, the fluorescence images of the fractals revealed the presence of three general types of regions of cell networks on the Si surfaces of the fractal electrodes, the ‘boundary’, ‘small-world’ network and ‘desert’ regions. The existence and extent of these regions were determined by the geometrical properties of the fractals and by abundance of glial proliferation sites.

The ‘boundary’ regions [Figure 4-3 b] were formed in the Si areas closest to CNT electrodes. They contained average and small sized clusters either attached to the CNT sidewalls or close to them. The processes from these clusters were usually extended on both Si and towards CNT electrodes climbing up the sidewalls or extending along the Si-CNT edge at the bottom of the sidewalls. Glial proliferations were observed in some instances.

The ‘small-world’ regions [Figure 4-3 c] were in the areas usually next to the boundary regions and further out from the CNTs. They contained the largest clusters, and these were connected through thick bundles of processes and were almost always accompanied by glial proliferations.

The ‘desert’ regions [Figure 4-3 d] were observed furthest from the CNT electrodes. They contained mostly individual cells and very few small clusters with weak processes extending from them. No neural network was observed, and few individual glial cells existed in these regions.

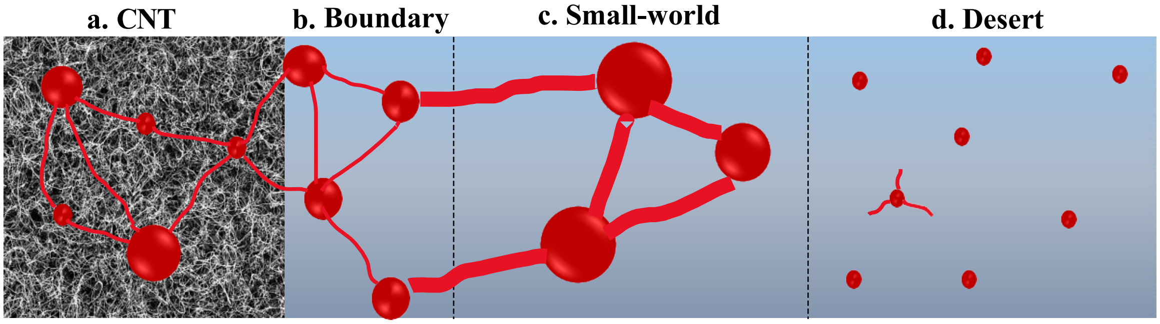

Figure 4-3. Schematic of the neural network regions on neighboring CNT and Si surfaces. a) The neural network on the CNT surface featuring small to medium clusters and individual cells with processes connecting them. b) The 'boundary' region on the Si featuring medium clusters connected to each other and to neurons on the CNT. c) The 'Small-world' region on the Si featuring larger clusters and bundles of processes connecting them. d) The 'desert' regions on Si featuring mostly individual cells and very few processes furthest from CNT electrodes.

4-2. Results

4-2.1. Neuron and Glial Herding on Fractal Electrodes

Fractal samples across all D values and number of iterations were successful in guiding glial proliferations into the Si regions. As seen in Figure 4-4 a, all datapoints in the scatterplot of G_{Si} vs G_{CNT} were located above the solid black herding line. For the neuron herding, 90% of the fractals were successful in guiding neuron processes onto the CNT electrodes as seen in the scatterplot of N_{CNT} vs N_{Si} [Figure 4-4 b].

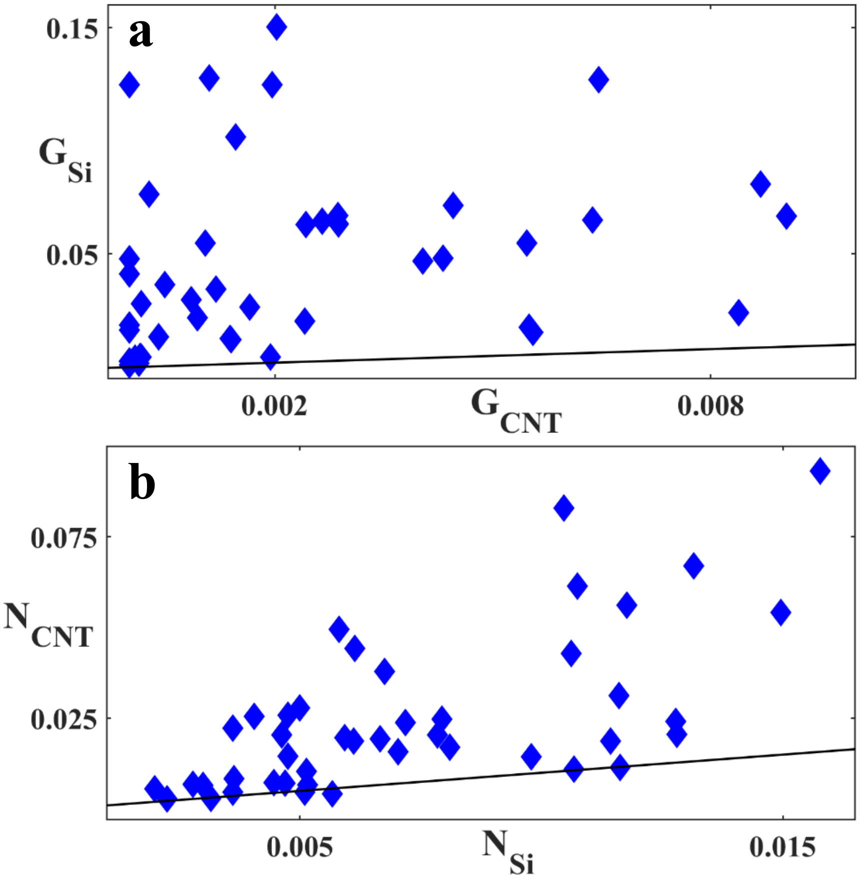

Figure 4-4. Glial and neuron herding for all fractal samples. Scatterplot of a) G_{Si} vs G_{CNT} and b) N_{CNT} vs N_{Si} for fractal samples. The solid black lines represent $G_{Si} = G_{CNT}$ and $N_{CNT} = N_{Si}$ in (a) and (b) respectively.

4-2.2. Statistical Analysis of Neuron and Glial Parameters for the Fractal Electrodes

All fractals were tested against the null hypothesis that changing the electrode's fractal dimension and the number of iterations should not affect N_{CNT}, N_{Si}, G_{CNT} and G_{Si}. The results of the Kruskal-Wallis followed by Dunn's test for N_{Si} showed significance between the following conditions [Figure 4-5 a]:

1.1 and 2-5 with P-Value = 0.001

1.1 and 2-6 with P-Value = 0.030

1.5 and 2-5 with P-Value = 0.040

Considering G_{Si} [Figure 4-5 b], there was significance between the 2-5 and 2-6 fractals with a P-Value = 0.036. No statistical significance in N_{CNT} and G_{CNT} between any fractal groups was detected [Figure 4-5 c, d].

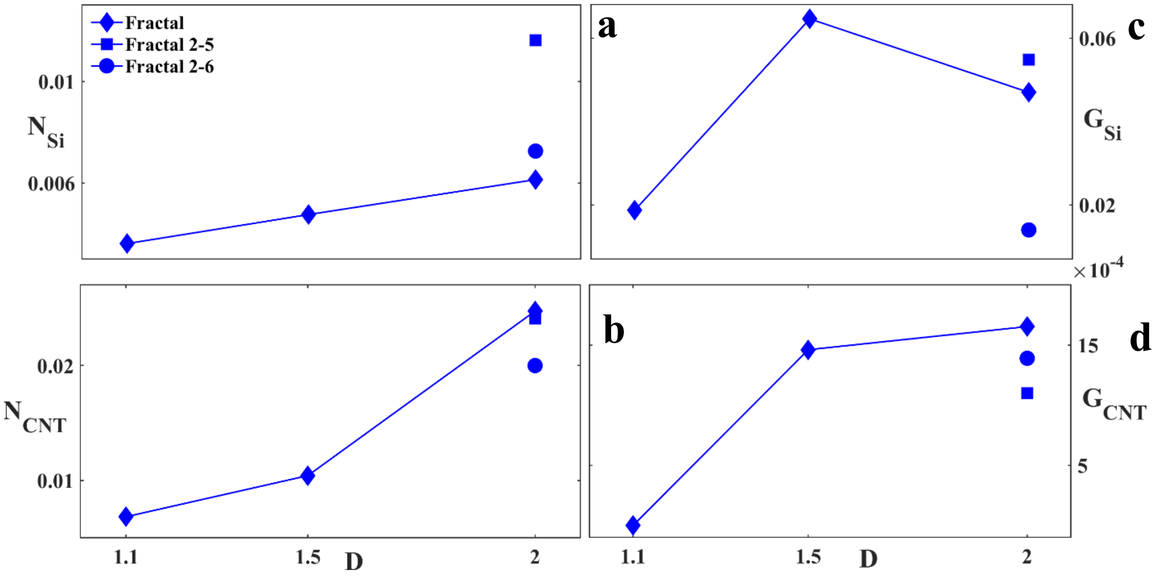

Figure 4-5. The change in neuron and glial parameters with D. a) N_{Si} median trend, b) N_{CNT} median trend, c) G_{Si} median trend and d) G_{CNT} median trend with D for all fractal groups. Error bars were not included for visual simplicity.

As seen in Figure 4-5 a and b, the median of both N_{Si} and N_{CNT} showed an increasing trend with the increase in D, although no significance was detected in the N_{CNT} case. The drop in GSi for the 2-6 fractal electrodes is related to decrease in the size of the Si regions as will be explained later in sections 4-3.2 and 4-3.3.

4-2.3. Comparison Between Fractal and Euclidean Electrodes

The advantage of the H-tree fractals over the simple Euclidean geometries lies in the fact that they provide a connected electrode with an abundance of edges for neurons to follow while glial cells can accumulate and proliferate inside the interconnected multi-scale Si regions. The fractals provide the opportunity for glial cells on the Si to migrate closer to the CNT electrodes to support neurons on both surfaces. In order to quantitatively compare the total “herding” power between the fractal and Euclidean geometries, the parameter GN was defined as glial herding (G) multiplied by neuron herding (N) [chapter II]. All Euclidean and fractal electrodes at each DIV were combined based on the culture times regardless of their different geometrical properties, i.e. 4 nominal variables of 3, 7 and 17 DIV Euclidean plus fractal groups were compared for statistical significance. The results of the Kruskal-Wallis comparison of medians with post-hoc Dunn’s test showed that all of the Euclidean geometries at any DIV had a significantly lower GN performance when compared to the fractal group. The P-Values between 3, 7, 17 DIV Euclidean and fractal groups were 9.2×10^{-10}, 2.2×10^{-5} and 0.005 respectively. These results show that the fractals perform better in the combined guiding of neurons onto the CNT branches and glia into the Si regions compared to all of the Euclidean groups. The histogram of the number of samples (n) with a given total herding value (GN) for 3 and 17 DIV Euclidean and fractal geometries was plotted [Figure 4-6 a]. Results for the 7 DIV Euclidean group were not included in the figure since there was no significance between the 7 and 17 DIV Euclidean GN values. (There was significance between the 3 and 17 DIV Euclidean groups with P-Value = 0.004). Figure 4-6 a indicates that not only does time evolution affect the total herding power within a given geometry, but also that this power could be improved through using fractal rather than Euclidean geometry.

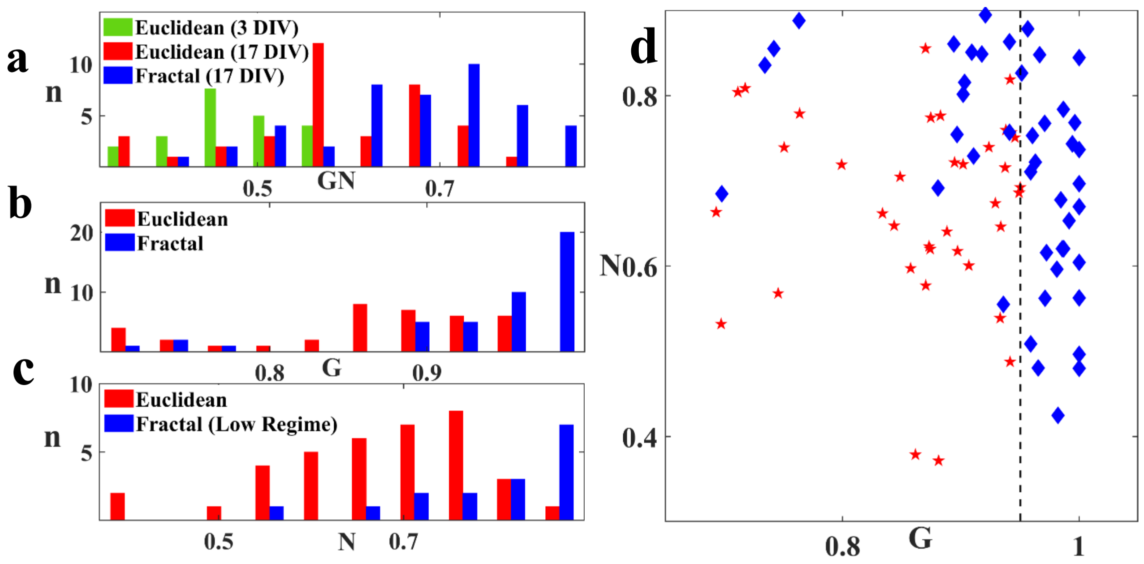

Figure 4-6. General comparison of fractal and Euclidean electrodes. a) Histogram of n, the number of samples with a given GN value for 3 and 17 DIV Euclidean plus 17 DIV fractal geometries. Statistical significance was detected between 17 DIV fractal and 3, 7, 17 DIV Euclidean samples with respective P-Values of 9.2×10^{-10}, 2.2×10^{-5} and 0.005 (7 DIV data not shown). b) Histogram of n, the number of samples with a given G value for 17 DIV Euclidean and fractal geometries. The two groups were statistically significantly different with a P-Value = 1.9×10^{-7}. c) Histogram of n, the number of samples with a given N value for 17 DIV Euclidean and low regime fractals. There was statistical significance between the two groups with a P-Value of 9.2×10^{-5}. d) Scatterplot of N, neuron herding, vs G, glial herding, for 17 DIV Euclidean (red pentagram) and fractal (blue diamond) samples. The dashed line marked the threshold G value above which no Euclidean sample existed.

The fractal samples were then compared with 17 DIV Euclidean samples in terms of their glial herding (G) power. Figure 4-6 b shows the histogram of the number of samples (n) with a given G value for 17 DIV Euclidean and fractal groups. Significance between the two groups was detected with a P-Value of 1.9×10^{-7} stating that fractals performed better at guiding glia into the Si regions compared to the 17 DIV Euclidean groups.

In order to observe the neuron and glial herding behavior of individual samples, the scatterplot of N vs G for the 17 DIV Euclidean and the fractal samples was plotted [Figure 4-6 d]. Each data point represents one sample. All samples from both geometries had G >

0.5 (one Euclidean sample with a G value below 0.5 was excluded from the plot but included in the analysis). The dashed black line in Figure 4-5 d represents a threshold in G ~ 0.95, beyond which no Euclidean samples were observed. The fractal samples on the other hand were able to achieve higher G values. Based on this threshold in G, the fractal samples were divided into two regimes. The ones to the left of the dashed line were labelled the 'low regime' and the ones to the right belonged to the 'high regime'. Both regimes included fractals with all D values and iterations. There was no relationship between fractal dimension or the number of iterations and the regime they belonged to. Considering N, some fractal samples in the high regime region encountered a depletion in N values compared to the ones in the low regime.

The low regime fractal samples were compared to the 17 DIV Euclidean group regarding their neuron herding power. Statistical tests showed a significance result with a P-Value of 9.2×10^{-5} confirming that the low regime fractal samples outperformed the 17 DIV Euclidean group in herding neuron processes. Figure 4-6 c shows the histogram of the number of samples (n) with a given neuron herding value (N) for the 17 DIV Euclidean and the low regime fractal groups. On the contrary, as seen in Figure 4-6 d the Euclidean and high regime fractals shared the same range of N values.

4-2.3.1. Comparison of Glial Cell Behavior for the Fractal and Euclidean Electrodes

To understand why the fractal samples performed better than the Euclidean group in terms of glial herding, the G_{Si} median dependency on fractal dimension D was replotted including the 3, 7 and 17 DIV Euclidean medians for comparison [Figure 4-7 plot]. The blue diamond symbols represent 1.1, 1.5 and 2-4 fractals. The blue square and circle represent the 2-5 and 2-6 fractals respectively. The blue asterisk represents the hypothetical case of a fractal with infinite number of iterations for which all Si regions had vanished and therefore G_{Si} is zero. The 3, 7 and 17 DIV Euclidean groups were shown with the green, yellow and red pentagrams respectively. Statistical tests between the 3, 7, 17 DIV Euclidean groups and the various fractal groups showed significance between the 3 DIV Euclidean and the 7 and 17 DIV Euclidean, 1.5, 2-4, and 2-5 fractals (3.6×10^{-5}, 3.9×10^{-8}, 2.9×10^{-6}, 2.7×10^{-6}, 3.9×10^{-9} respectively) and between the 7 DIV Euclidean and the 2-5 fractals (0.005). Although no significance was detected between the 17 DIV Euclidean group and any of the fractal groups, all fractal G_{Si} medians except 2-6 were higher than the 17 DIV Euclidean groups.

Glia fluorescence images of 1/4th of the full electrodes were included in Figure 4-7 to visually compare the effect of having multi-scaled interconnected Si regions and the closeness of the Si regions to the CNT branches for the fractal electrodes versus the disconnected rows of Si and CNT in Euclidean electrodes on glial proliferation.

The statistical comparison of G_{CNT} also showed no significance between the fractal groups and the 17 DIV Euclidean samples, but the medians for fractals were lower than the 17 DIV Euclidean group. Therefore, the high G values achieved by fractals in Figure 4-6 d were the result of having higher G_{Si} and lower G_{CNT} values.

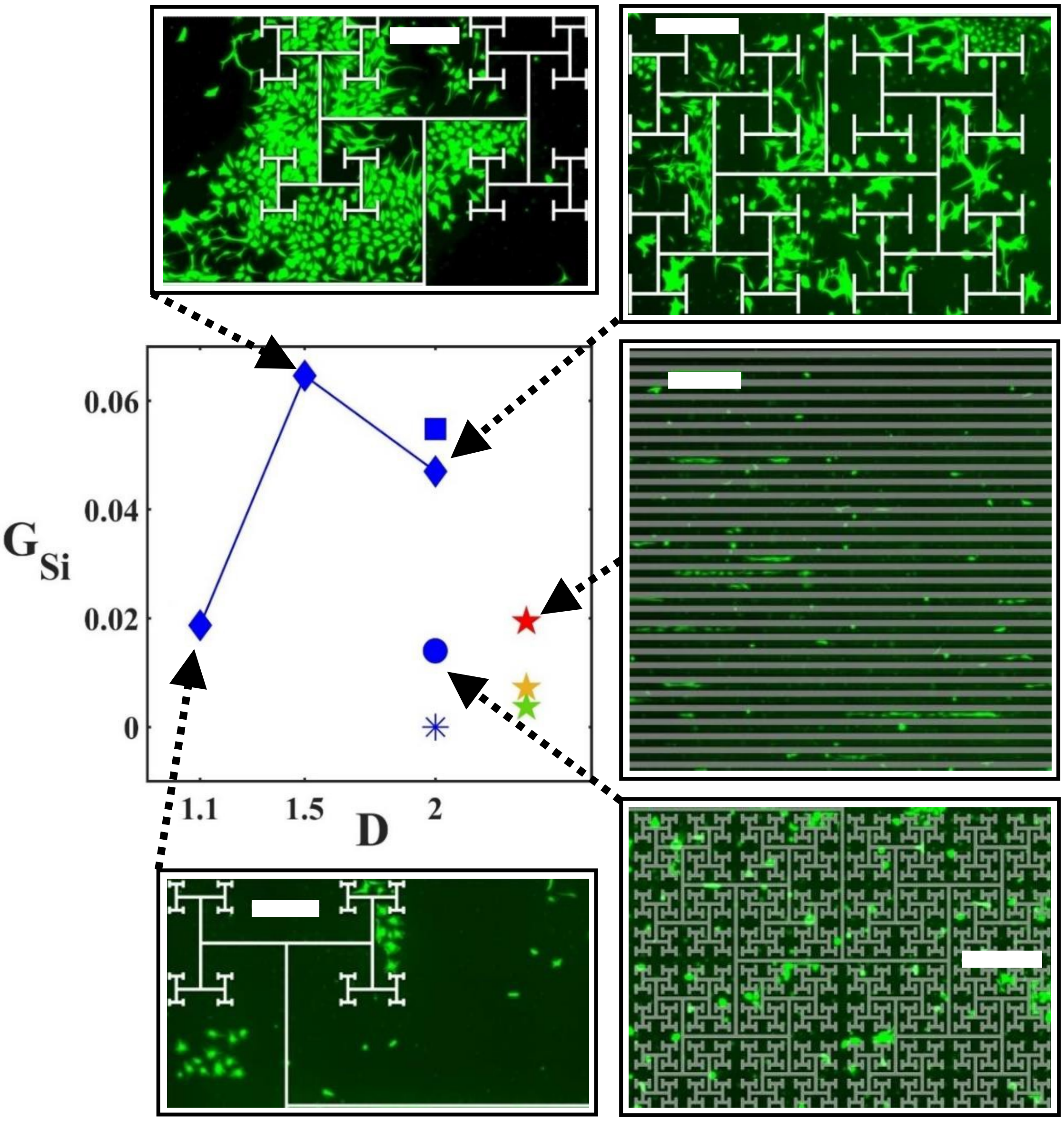

Figure 4-7. G_{Si} median change versus D for the fractal groups. Fluorescence images of glial proliferation instances on 1/4th of the full sample images for the 1.1, 1.5, 2-4 and 2-6 fractals and the GR50 Euclidean group were included for comparison. The markers and colors in the plot are explained above. White masks are imposed with the fluorescence images to emphasize the locations of the electrodes. The arrows connect images to their corresponding datapoints in the plot. Scale bars are 500 μm. Error bars were excluded for visual simplicity.

4-2.3.2. Comparison of Neuron Behavior for the Fractal and Euclidean Electrodes

To quantitatively observe the effect of glial cell behavior on neuron process length on Si surfaces, N_{Si} for individual samples was plotted against G_{Si} in a scatterplot [Figure 4-8 a]. The low and high regime fractal samples were marked with different symbols to account for any possible difference in behavior in N_{Si} or G_{Si}. No differences between the two regimes was observed. This indicated that the higher G values for high regime fractals were not achieved by having higher G_{Si}, but rather by having lower G_{CNT} compared to the fractals in the low regime. Comparing the range of G_{Si} values between the 17 DIV Euclidean group and the two fractal regimes, very few Euclidean samples reached G_{Si} values as high as some fractals. For the fractal samples, having more glial cells on the Si surfaces did not necessarily result in having more neuron processes on the Si surfaces. In the Euclidean case, in contrast, N_{Si} and G_{Si} increased hand in hand. Most of the low regime fractals that had N_{Si} vs G_{Si} trends similar to Euclidean samples belonged to the 2-6 group.

To study the N_{Si} behavior for the fractal samples in more detail, the histogram of the number of samples, n, with a given N_{Si} for the different fractal groups was plotted [Figure 4-8 a inset]. It was observed that higher D and higher iteration fractals gradually produced higher N_{Si} values. As an example, most of the 1.1 fractals were located on the left side of the plot at lower N_{Si} values while the 2-5 fractals were the dominant group on the right side. The exception was the 2-6 group that had samples occupying all ranges of N_{Si} as seen by the location of the orange bars in the plot. The statistical significance between the fractal groups was previously mentioned in section 4-2.2.

Next, the relation between N_{Si} and N_{CNT} was quantitatively studied by plotting a N_{CNT} versus N_{Si} for the three groups, Euclidean, low regime and high regime fractals

[Figure 4-8 b]. The solid black line represents successful herding, i.e. N_{CNT} is larger than N_{Si} for the samples above the line. The solid blue, dashed blue and solid red lines were linear fits through zero corresponding to low regime fractal samples, high regime fractal samples and the Euclidean samples respectively. Both the high and low regime fractal fit lines had higher slopes than the Euclidean group. The slightly higher slope of the high regime fit versus the Euclidean fit was achieved because the high regime fractals supported fewer processes on Si. That is, for a given N_{CNT}, the high regime had smaller N_{Si} values than the Euclidean group. As seen in the histogram of N_{CNT} in Figure 4-8 b inset, the increase in N_{CNT} values with the increase in D and number of iterations of the fractal groups had a similar trend to N_{Si} for the same groups. The exception was the 2-6 group which had a range of N_{CNT} values.

The low regime fractals had the same N_{Si} range as the high regime [Figures 4-8 a and 4-9 a], but reached higher N_{CNT} values, i.e. they supported more neuronal growth on the CNTs. There was a depletion in N_{CNT} going from the low to high regime fractals. Figure 4-9 b shows the boxplot of N_{CNT} values for the low and high regime fractals. A significance with the P-Value = 0.006 was detected between the two groups. Therefore, having lower N_{CNT} was the cause of having lower N values in the high regime fractal group.

Summarizing the observations so far, it is known that fractals generally did reach higher G values by having more glia on Si and less on CNT, i.e. higher G_{Si} and lower G_{CNT}. The low regime fractals won over the high regime and Euclidean groups in terms of neuron herding by supporting the growth of more neuron processes on CNT and less on Si surfaces. The remaining question is why high regime fractals performed better in terms of glial herding compared to the low regime despite the fact that no difference was detected in G_{Si} behavior between the two groups.

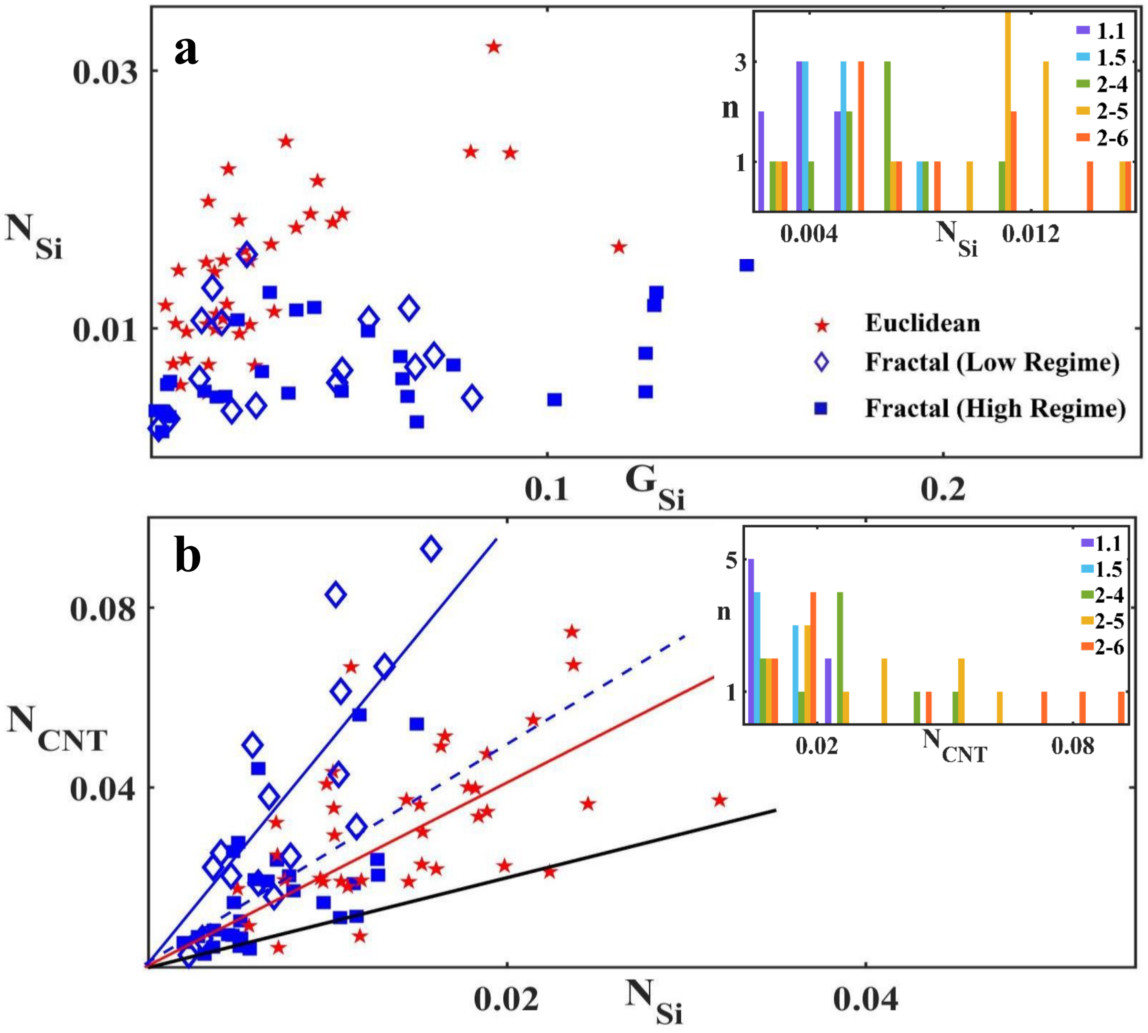

Figure 4-8. Study of the effect of G_{Si} on N_{Si} and N_{CNT} for fractal and Euclidean samples. a) Scatterplot of N_{Si} vs G_{Si} for 17 DIV Euclidean (red pentagram), low (diamond) and high (filled square) regime fractals. a inset) Histogram of n, the number of samples with a given N_{Si} value for all fractals, grouped based on D and number of iterations. b) Scatterplot of N_{CNT} vs N_{Si} for 17 DIV Euclidean, low and high regime fractals. The solid black line represents $N_{CNT} = N_{Si}$, the solid blue, dashed blue and solid red lines are fits through zero for the low regime fractal, high regime fractal and Euclidean groups respectively. b inset) Histogram of n, the number of samples with a given N_{CNT} for all fractals, grouped based on D and number of iterations.

To answer the final question and to confirm the previous results, N_{Si}, N_{CNT}, G_{Si} and G_{CNT} were statistically tested against the null hypothesis that no difference existed between the two fractal regimes. Figure 4-9 shows boxplots of all four parameters for the two regimes. No significance was detected in N_{Si} and G_{Si}. There was significance between both N_{CNT} and G_{CNT} parameters with P-Values equal to 0.006 and 6.6×10^{-5} respectively. It was concluded that the high regime arose not by having more glial cells on Si, but by putting very few on the CNT electrodes. The depletion in N_{CNT} and G_{CNT} for the high regime was linked in the sense that samples with low G_{CNT} values also had low N_{CNT} [Figure 4-10]. No differences in the general conditions of the samples in the two regimes were detected based on fabrication, culture or seeding cell density.

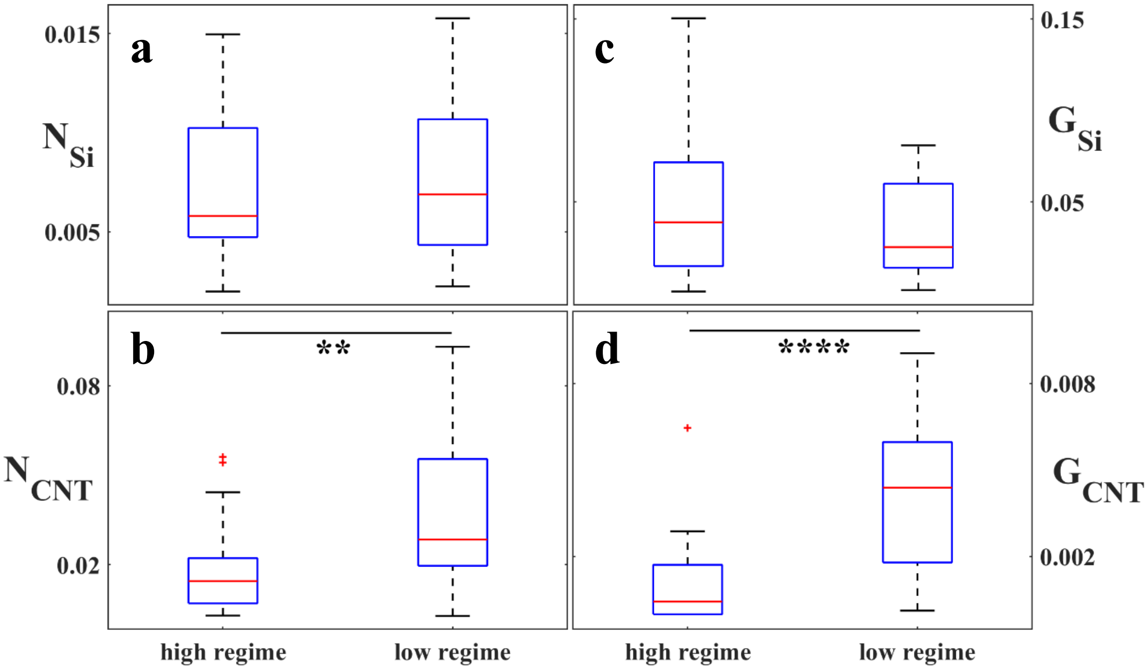

Figure 4-9. Comparison between the low and high regime fractal groups. a) N_{Si}, b) N_{CNT}, c) G_{Si} and d) G_{CNT} boxplots for the high and low regime fractal comparison. No significance was observed in N_{Si} and G_{Si} between the two groups. Stars in (b) and (d) determine the degree of significance. ** denotes $0.001 < P \leq 0.01$ and **** denotes $P \leq 0.0001$.

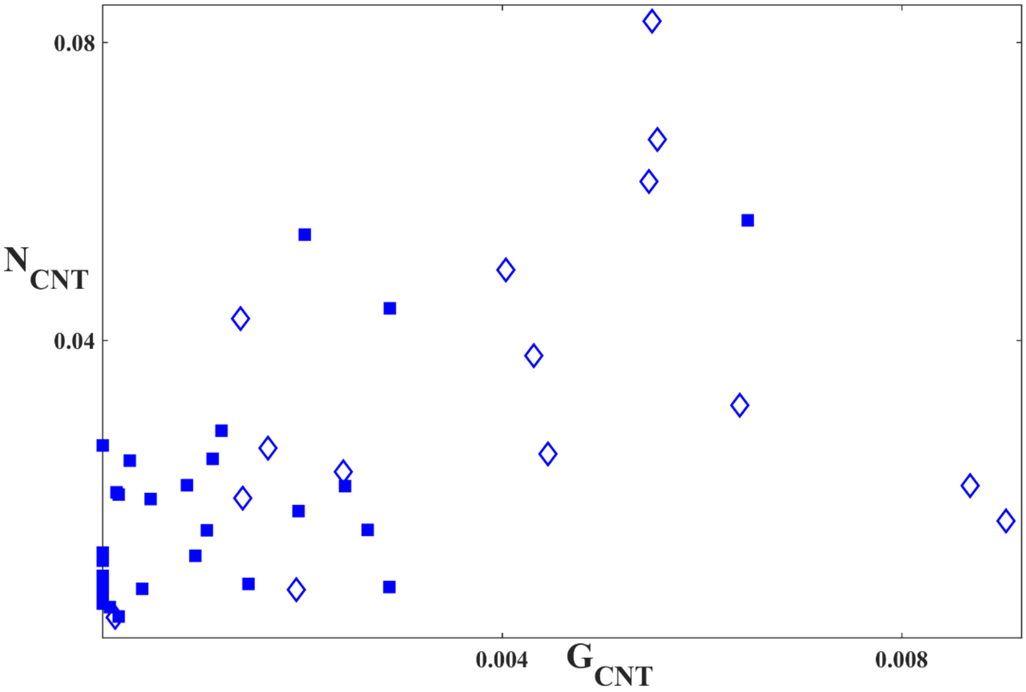

Figure 4-10. Scatterplot of N_{CNT} vs G_{CNT} for the high and low regime fractal groups.

4-3. Discussion

In sections 4-1 and 4-2, the outperformance of the fractal electrodes over Euclidean ones was qualitatively and quantitatively studied. It was shown that fractal electrodes were able to reach G values beyond access of the Euclidean ones. The two fractal regimes (low versus high) were defined based on their performance in glial herding onto the desired surfaces. The low regime fractal samples had high performance in neuron herding compared to Euclidean and the high regime samples [Figure 4-8 b] but behaved similar to the Euclidean samples regarding glial herding. High regime fractals, on the other hand, had high performance in glial herding, but had similar N values as the Euclidean group [Figure 4-6 d]. This section focuses on explaining the hypotheses behind the observed behavior for the two geometries based on their geometric properties and possible effects on the evolution of small-world networks discussed in Chapter III.

4-3.1. The Presence of Patterned Materials on Substrate Can Affect Neural Network Status

In chapter III, the development of a small-world network of cells on an unpatterned substrate was discussed. The role of adhesion forces between cell-substrate and tension forces exerted through processes was explained. This section focuses on explaining the effect of micron-scale patterned substrates on neural network development. Physical modification of substrates with micron-scale geometries has been long used as scaffolds to control cell attachment and pattern neuronal networks.[108,116,126,146,147] From the perspective of the small-world network, the shape of the network and its degree of connectivity can be influenced by introducing cell-substrate adhesion forces with different strengths. Figure 4-11 shows a schematic of how the presence of a CNT-Si boundary could affect the location and size of clusters formed on Si either attached to or close to a CNT edge. It was assumed based on the hypotheses discussed in Chapter III that the cell-CNT adhesion force (green arrow) is stronger than the cell-Si adhesion (yellow arrow) and the cell-cell tension forces (purple arrow) along the processes. In addition, the cluster is assumed to be stationary and cells 1 and 2 are at equal distances from it.

Individual cells 1 and 2 in Figure 4-11 a, connected to the cluster on Si, experienced the same tension forces, but different cell-substrate adhesion forces. A net force (black arrow) was exerted on cell 2. Therefore, it started migrating along the process connecting it to the cluster and eventually joined the cluster [Figure 4-11 b]. In contrast, cell 1 was strongly attached to the CNT sidewall and the tension force from the cluster was not large enough to displace it to join the cluster.

Cells 3 and 4 experienced the same adhesion cell-substrate adhesion and the same cell-cell tension forces along the processes connecting them to cell 5. Assuming that the tension forces were larger than the adhesion forces, they both started migrating towards cell 5 and joined it to form a small cluster on the CNT sidewall [Figure 4-11 b].

The frequency of the occurrence of either of the two cases described above and the role they play in creating the boundary, small-world and desert regions, depends on the closeness and accessibility of CNT edges. For example, if there were another CNT edge close to cells 3 and 4, they could have migrated towards it and adhered. Therefore, no cluster on the sidewall would have been formed.

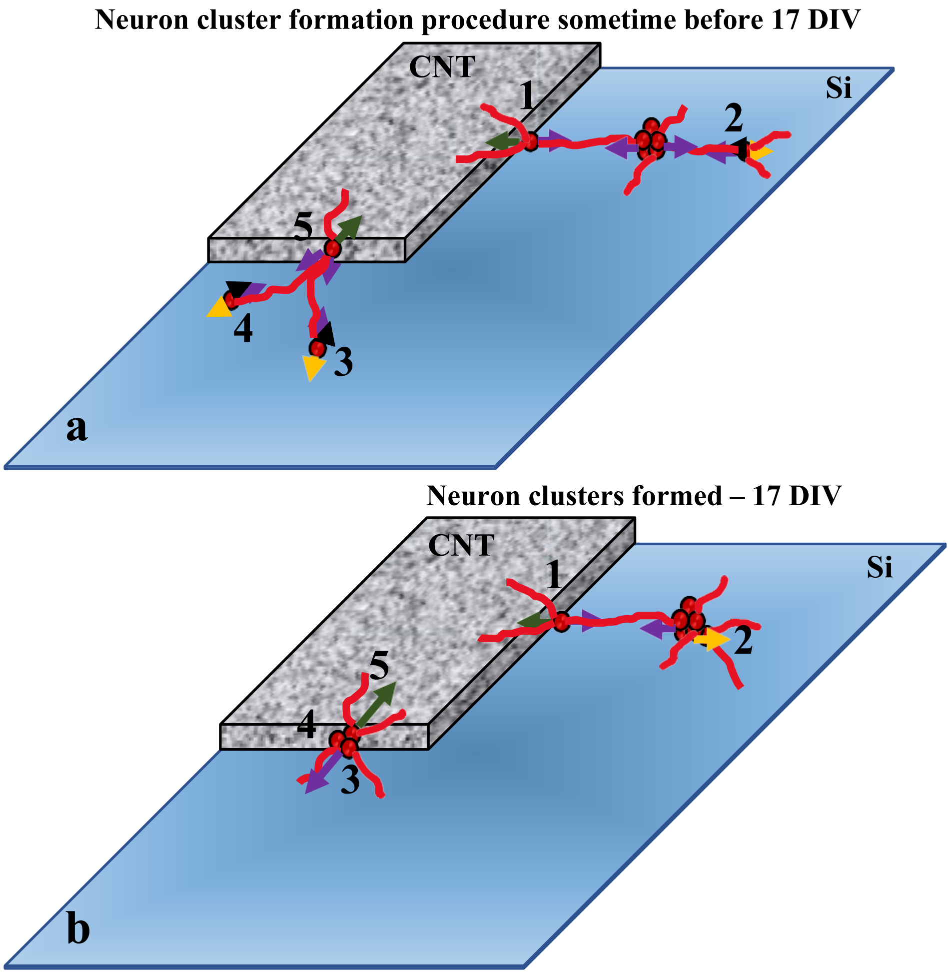

Figure 4-11. Schematic of interactions between individual neurons and clusters close to a CNT-Si edge. a) Sometime between 7 and 17 DIV, when the network is at its maximum connectivity. b) At 17 DIV, when the network optimization phase has presumably finished.

All samples were initially seeded uniformly. This uniformity was disturbed by 17 DIV, showing the ability of cells to migrate on the smooth Si surface. Neurons explored their environment searching for chemical and physical cues from other cells and from the substrate by sending out a leading process in search of strong anchorage points. Once the leading process formed a strong enough adhesion to the anchor, the translocation of the cell body along the process was initiated.[148] Various studies have shown that neurons travel with average speeds of 10-20 μm/h on smooth surfaces and cover distances as far as hundreds of microns, especially in the first few weeks of culture. [129,130,148,149,150,151] Neurons that initially landed in proximity to the CNT electrodes had higher chances of finding the CNT edges during the first few hours of the culture. For these neurons, stronger cell-CNT adhesion forces slowed down neuron aggregation and the cluster formation process, resulting in the formation of the boundary regions. Neurons that landed further away from CNT edges had to migrate longer distances in order to find anchor points in the form of either other cells or rough impurities on the surface. For these regions, neurons had a higher tendency for aggregation and followed the rules of small-world network formation as was previously described in Chapter III.

Desert regions were formed and expanded gradually throughout the culture time due to neuron-neuron, glia-glia and neuron-glia chemical and mechanical signaling. Neurons on the CNT top surfaces or attached to the sidewalls were not able to migrate and leave the surface. They gradually attracted neurons on the Si towards the electrodes by sending chemical cues and encouraging migration towards the electrodes to form potentially stronger connections. This process left the Si surfaces furthest away from CNTs almost empty of cells. Glial cells started proliferating on Si after 7 DIV as a support system for the neurons. They followed neuronal cues and started migrating towards and proliferating close to the electrodes. Emergence of more glial cells enhanced neuronal migration along their fibers[142,151] towards the CNTs especially on lower D fractals and therefore expanded the desert areas even further. Our observations agreed with other studies on smooth surfaces showing that in a glial and neuronal patterned co-culture, glia dictated neuronal patterning fate by directing neurons to glial proliferation regions.[49] Together, neurons and glia on both CNT and Si surfaces formed local interconnected networks.

The next section focuses on defining parameters for fractal geometries that allow a more quantitative analysis of the emergence of the different types of regions on Si surfaces and their effect on neuron and glial parameters.

4-3.2. Mathematical Characteristics of Fractals

Several geometric parameters were calculated for fractals with X_L and w_f equal to 6262 μm and 20 μm respectively. The fractal dimension D was varied from 1.1 to 2 in 0.1 increments for N_f = 7, 9 and 11 (corresponding to 4, 5 and 6 iterations). Fractals with D and N_f values that resulted in overlapping branches based on the chosen X_L and w_f were excluded from the analysis.

The normalized edge length, E, was calculated by dividing the total edge length by the length of the pattern. Figure 4-13 d shows the plot of E vs D for 4,5 and 6 iteration fractals.

$$\mathrm{E} = {}^{\mathrm{E}_f}\!/_{\mathrm{X}_L}$$

In order to calculate the mean tortuosity (T) of each pattern, first all tortuosity values were calculated by dividing the pathlength from the center to the endpoint of a final branch by all possible displacements from the center to the endpoint of a final branch [Figure 4-12]. T was the average of all calculated values and was then plotted vs D in Figure 4-14 e.

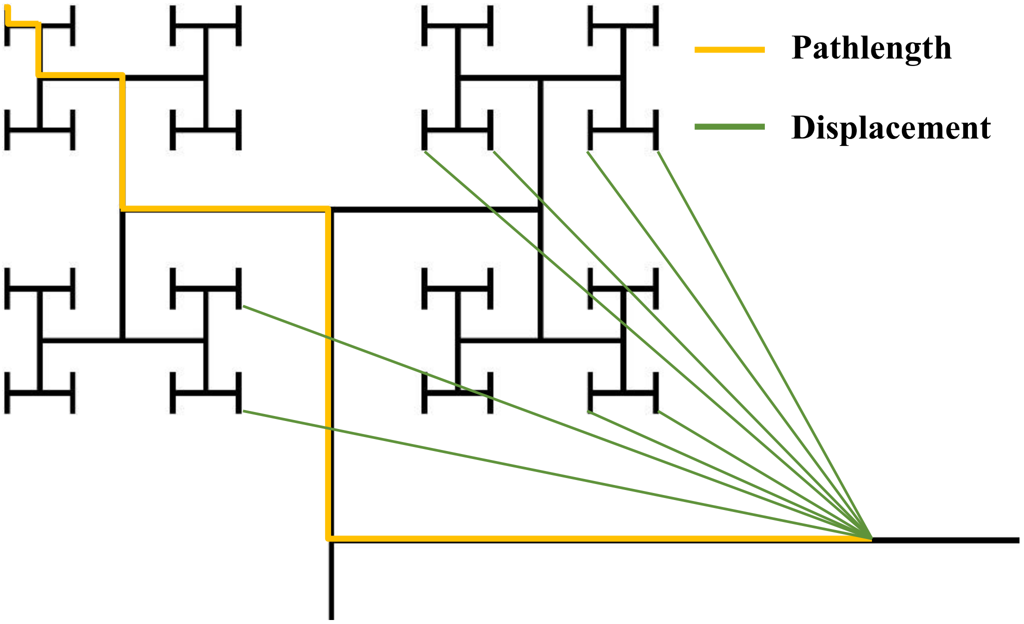

Figure 4-12. Schematic representation of the tortuosity calculation for a fractal. The yellow line is the pathlength from the center to the end of a final branch and is the same for all endpoints. The green lines are example displacements from the center of the fractal to the endpoints of final branches. For clarity, the figure does not show all possible displacements.

The mean proximity P was calculated using the binary masks previously generated for fabrication purposes. Figure 4-13 shows the process of converting a binary mask into a proximity heat map. Figure 4-13 a shows a matrix representing a binary mask. The distance between each pixel to its nearest CNT pixel was calculated [Figure 4-13 b]. The proximity matrix was created by assigning the equivalent 1/(minimum distance) to each Si pixel [Figure 4-13 c]. P was then calculated by averaging over all matrix elements and was plotted vs D [Figure 4-14 f]. The matrix was used to generate the heat maps in Figure 4-14 a, b and c.

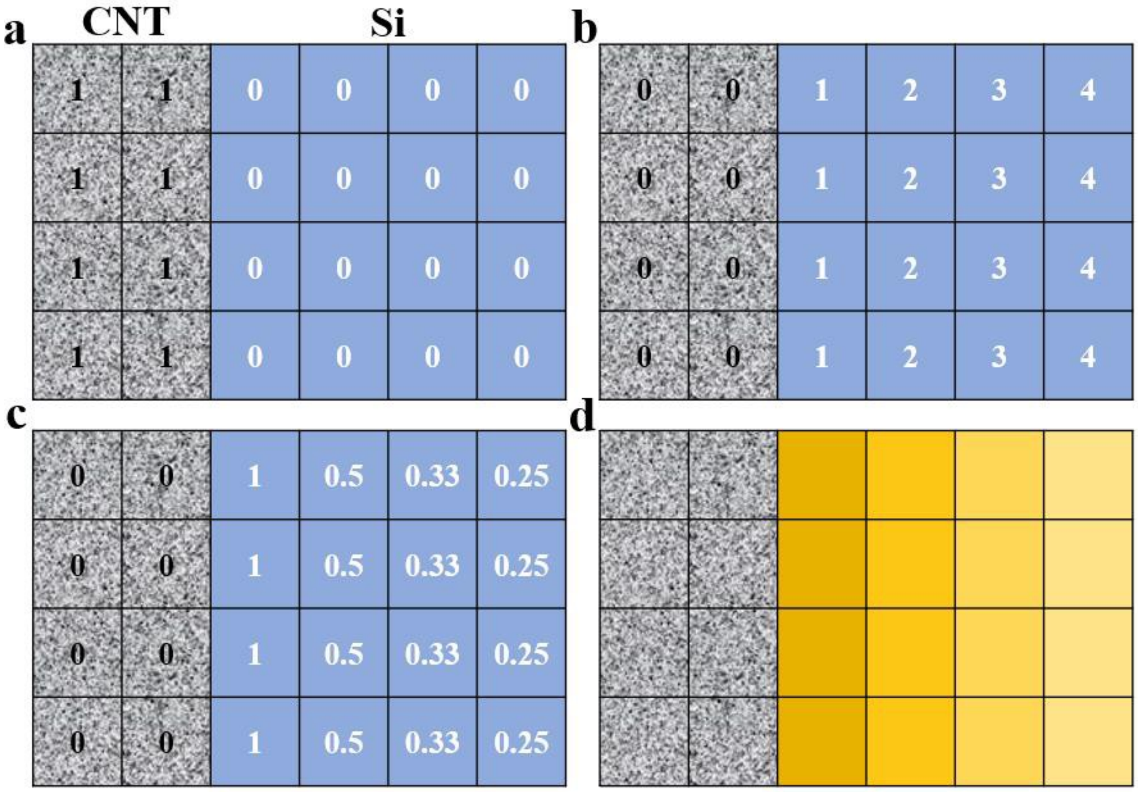

a

1	1	0	0	0	0
1	1	0	0	0	0
1	1	0	0	0	0
1	1	0	0	0	0

b

0	0	1	2	3	4
0	0	1	2	3	4
0	0	1	2	3	4
0	0	1	2	3	4

c

0	0	1	0.5	0.33	0.25
0	0	1	0.5	0.33	0.25
0	0	1	0.5	0.33	0.25
0	0	1	0.5	0.33	0.25

Figure 4-13. Schematic of converting a binary mask to a proximity heat map. a) Matrix representation of a binary mask. b) Each pixel value was substituted with minimum distance from a CNT pixel. c) Pixel values in (b) were replaced by their inverse. d) Colors in the schematic heat map represented closeness to the CNT pixels.

$\mathrm{A_r}$, was calculated as the ratio of the largest (bounded red areas in Figure 4-14 a, b and c) to the smallest (filled red boxes in Figure 4-14 a, b and c shown with arrows) Si areas within a fractal pattern. These areas were defined such that they were confined by the electrode branches without any intersection or interruption. $\mathrm{A_r}$ was then plotted versus D for 4, 5 and 6 iteration fractals [Figure 4-14 g].

$$\mathrm{A_r} = {}^{\mathrm{A_{max}}}/_{\mathrm{A_{min}}}$$

$\mathrm{A_c}$, the normalized connected area was calculated as the ratio of the largest connected area within the fractal that is not interrupted or cut off by any electrode branch, A (calculated in Chapter II, the light gray areas in Figure 4-14 a, b and c), to the bounding area, assuming the fractal was bound inside a box. A_c was then plotted vs D [Figure 4-14 h].

$$A_c = 2^{\frac{1}{D}} \times {}^{A}/_{{X_L}^2}$$

E quantifies the edge length available, T and P characterize the accessibility of the edges and the closeness of the Si areas to the CNT electrodes. Larger edge lengths provide more CNT sidewalls as anchor points for cells on the Si to adhere to, survive and grow processes along. Fractals with higher tortuosity distribute Si and CNT areas more uniformly with respect to each other. Larger average proximity values ensure shorter travel distances for cells on Si to find a CNT edge. Large T and P values ensure shorter migration distances. Increasing D and the number of iterations either separately or together would increase the normalized edge length, tortuosity and average proximity of the pattern.

A_r and A_c characterize the freedom of movement and openness of the patterns. Large A_r values show a drastic difference in size of the Si regions between the first and final iterations of the fractal (A_{max} vs A_{min}). This could be interpreted as a low resistance towards cell migration from one Si region to its neighbors. Large connected areas provide a large enough space for glial cells to proliferate without facing interruptions by the CNT branches. As D or the number of iterations increase both A_r and A_c decrease.

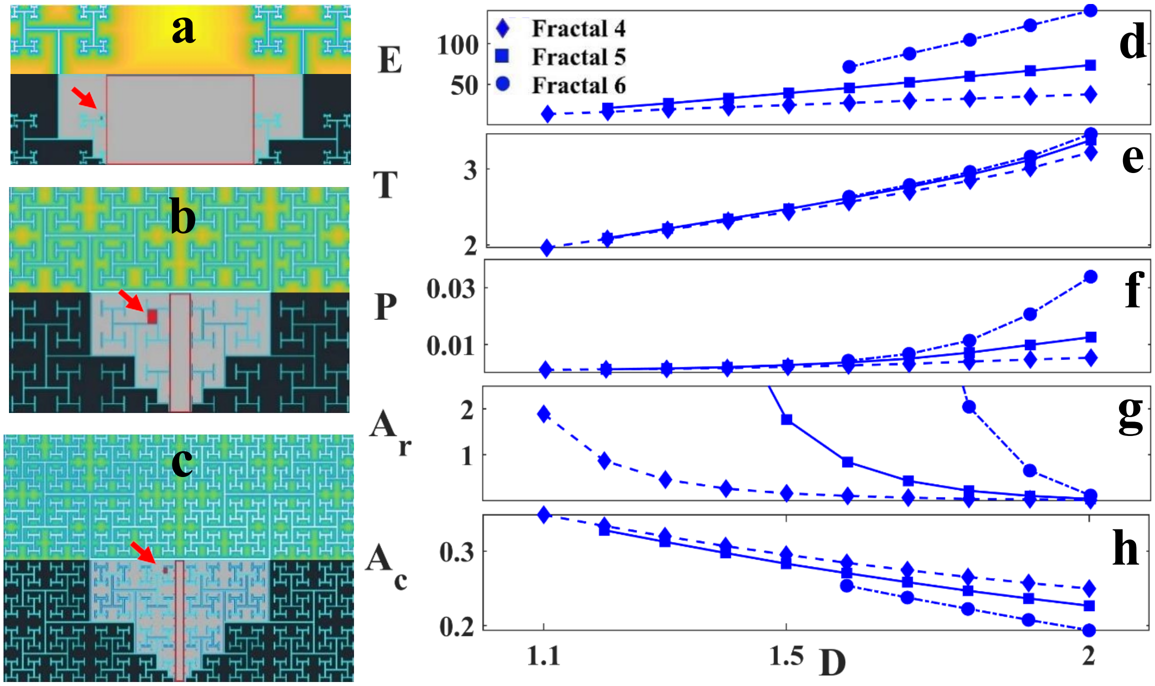

Figure 4-14. Schematics of fractals and their proximity heat maps, plus plots of fractal characteristics vs D. a), b) and c) top and bottom half represent the proximity heat map and the schematic for the 1.1, 2-4 and 2-5 fractals respectively. The largest (bounded red boxes), smallest (red rectangles) and largest connected Si (light gray) areas are marked accordingly. d) Normalized edge length, e) mean tortuosity, f) mean proximity, g) Area ratio (y axis multiplied by 10^5) and h) normalized connected area plotted vs D for 4, 5 and 6 iteration fractals.

Fractals with low E, T and P values combined with high A_r and A_c produce vast empty Si areas far away from electrode branches that would eventually become desert regions. On the other hand, high D or high iterations fractals provide high E, high tortuosity and therefore high proximity between CNT and Si regions, but low A_r and A_c. These characteristics would mostly create boundary regions. Desert areas would vanish in these patterns since no large enough Si area away from CNT electrodes would exist.

4-3.3. Fractal Electrodes Support More Glial Proliferation, i.e. Larger G_{Si}

The interconnected multi-scaled character of the Si regions in the fractal electrodes characterized by A_r and A_c gave the glia the freedom to migrate and proliferate while keeping close proximity to neurons on the Si and on the CNT electrodes. On the other hand, the single-scale one dimensional nature of the Si regions in the Euclidean electrodes, combined with no tortuosity did not encourage much proliferation. The 2-6 fractals collapsed into the Euclidean regime in the sense that they started losing the interconnected multi-scaled characteristic of a fractal structure (low A_r and A_c). Therefore, they hindered glial proliferation on Si in the same manner as the Euclidean samples.

If only considering the effect of A_r and A_c on glial proliferation, it would be reasonable to expect that the 1.1 fractals should have the highest glial proliferation among all of the samples. However, as seen in Figure 4-7, on average they did not perform as well as 1.5, 2-4 and 2-5 fractal samples. This was due to the fact that the 1.1 fractals have low E, T and P magnitudes that combined with high A_r and A_c values, produce desert areas almost empty of neuron processes. Therefore, no glial cells would be needed as a life support system.

Based on the plot in Figure 4-7, fractals with intermediate to high D values and 4 to 5 iterations provided sufficiently large interconnected Si spaces for glial proliferation and close proximity to neurons on the CNT electrodes by having large enough E, T and P values.

In summary, the 1.1 fractals were too “open”, and the 2-6 fractal and Euclidean geometries had small disconnected gaps. In this spectrum, the 1.5, 2-4 and 2-5 appeared to have the optimal balance of large and small interconnected areas and provided close proximity between neurons and glia on Si to neurons on CNT.

4-3.4. The Effect of G_{Si} on N_{Si} and N_{CNT}

4-3.4.1. The Euclidean Electrodes Supported More Neuronal Growth on Si Surfaces

As discussed before, the total edge length (E) and closeness to the CNT edges (T and P) directly affect the type of neural network formed on Si surface. For the Euclidean geometries, neurons landing inside the Si areas in the most extreme case had to migrate a maximum distance of 50 µm in the R100 samples to reach a CNT edge and anchor to it. For fractals, this maximum distance was not constant and varied with the geometrical characteristics of the patterns. On Euclidean geometries and the 2-6 fractals, mostly boundary regions existed with more processes connecting the clusters and individual cells together. In these regions, the pruning of neuron processes did not take place as effectively as in the small-world regions due to the strong anchorage of cells and clusters to the CNT sidewalls. The other fractals (i.e. not the 2-6 fractals) had a combination of desert, small-world and boundary regions depending on their D values. In addition, proximity to glial proliferations increased the occurrence of small-world regions by facilitating neuronal migration and aggregation. This phenomenon played a role in decreasing N_{Si} for the fractals compared to the Euclidean geometries. Low D fractals that supported more desert or small-world regions had lower N_{Si}, and therefore were located on the left of the histogram in Figure 4-8 a inset. As D and iterations increased, desert areas gradually disappeared. Small-world and boundary regions became more prevalent, so increasing the number and length of neuron processes gradually (i.e. generating larger N_{Si}).

4-3.4.2. Neural Networks on Si Surfaces Support Neuronal Growth on the CNT Electrodes

Fractal electrodes that supported more boundary regions, i.e. high D and high iterations fractals, had more clusters either close to or attached to the sidewalls. These clusters grew neuron processes on both the CNT and Si surfaces as seen in Figure 4-1 a and d. In addition, these electrodes provided more edge length for processes to follow. Therefore, increases in D and the number of iterations caused an increase in N_{CNT} as previously seen in Figure 4-8 b inset.

The slight improvement of the average behavior of the high regime fractals over the Euclidean samples in terms of herding neurons onto the electrodes [Figure 4-8 b] was, as stated previously, related to the fact that high regime fractals had lower N_{Si} values compared to the Euclidean groups while having the same range of N_{CNT} values. This could again be tied to the differences in geometrical characteristics of fractals vs Euclidean discussed in section 4-3.4.1.

4-3.5. Time Evolution of Fractal Electrodes with Respect to All DIV Euclidean Electrodes

Thus far, it’s known that the fractal electrodes perform better than the 17 DIV Euclidean electrodes in terms of herding glial cells into the Si regions and having more processes on the CNT electrodes. To compare where the fractals stand with respect to all

Euclidean samples, scatterplots of N_{CNT} vs N_{Si} [Figure 4-15 a], G_{Si} vs G_{CNT} [Figure 4-14 b], N_{Si} vs G_{Si} [Figure 4-15 c] and N_{CNT} vs G_{CNT} [Figure 4-15 d] for fractals and all Euclidean samples separated based on DIV were plotted. Solid blue, green, yellow and red lines were fits to fractals, 3 DIV, 7 DIV and 17 DIV Euclidean groups respectively.

For the fractal samples, the neural network on Si has developed further towards an optimized state vs Euclidean samples at all DIVs. As seen in Figure 4-15 a, the N_{Si} range for fractals was even smaller than the N_{Si} range for 3 DIV Euclidean group, meaning that the neural networks were optimized through pruning and joining clusters to a degree that the 17 DIV Euclidean samples were not able to reach. And therefore, for roughly the same range of N_{CNT} between all groups, the fractal electrodes were more successful in herding neurons by speeding up the evolution of the neural networks on Si towards an optimized state. This phenomenon goes hand in hand with supporting more glial proliferations compared to all DIV Euclidean samples. An inverse relationship exists between N_{Si} and G_{Si}. As previously discussed, glial proliferations support neuronal migration towards forming a more optimized network in which fewer processes were needed to keep the network connected. Figure 4-15 c confirmed these results for all culture durations and all geometry types. A decrease in slope of the fit lines from 3 DIV Euclidean towards fractals was observed.

Figure 4-15 b confirmed the already known results that fractal electrodes outperformed the 17 DIV and consequently the 3 and 7 DIV Euclidean electrodes in terms of herding glial cells into the Si regions. Once again, an ordered gradual change in the slope of fit lines from 3 DIV Euclidean towards the fractal state was observed.

Figure 4-15 d was interpreted as the gradual evolution of the neural network on the CNT surfaces towards an optimized small-world network. The comparable slopes of the 17 DIV and fractal fit lines confirmed that on the CNT electrodes, neurons behaved similarly irrespective of the widths available to them.

Based on all these observations, it was hypothesized that fractal electrodes at 17 DIV evolve the culture system to a state further optimized compared to the Euclidean electrodes from the same culture duration. In this sense, fractal cultures could be considered the equivalent to a Euclidean electrode that was kept in culture for longer than 17 DIV in terms of neural network evolution. Yet, it cannot be claimed that 17 DIV fractals were at the final stable state in both neuronal and glial development. Longer cultures would be needed to test the status of the networks formed.

As a final check, unpatterned Si substrates were used for 3, 7 and 17 DIV cultures. Normalized total neuron length, N_{Si}, and normalized total glial area, G_{Si}, were calculated for each DIV. G_{Si} and N_{Si} median trends vs culture time were plotted for the Si control, Euclidean and fractal samples [Figure 4-16 a, b]. These plots confirmed previously found results and hypotheses that the presence of patterned materials in interaction with neurons and glial cells affects the degree of optimization of the network formed. As seen in Figure 4-16 a, up to 7 DIV there was no difference between the Euclidean samples and the control Si samples in terms of glial area. At 17 DIV, glial proliferation on the control Si surpassed both fractal and Euclidean groups with the fractals winning over Euclidean group.

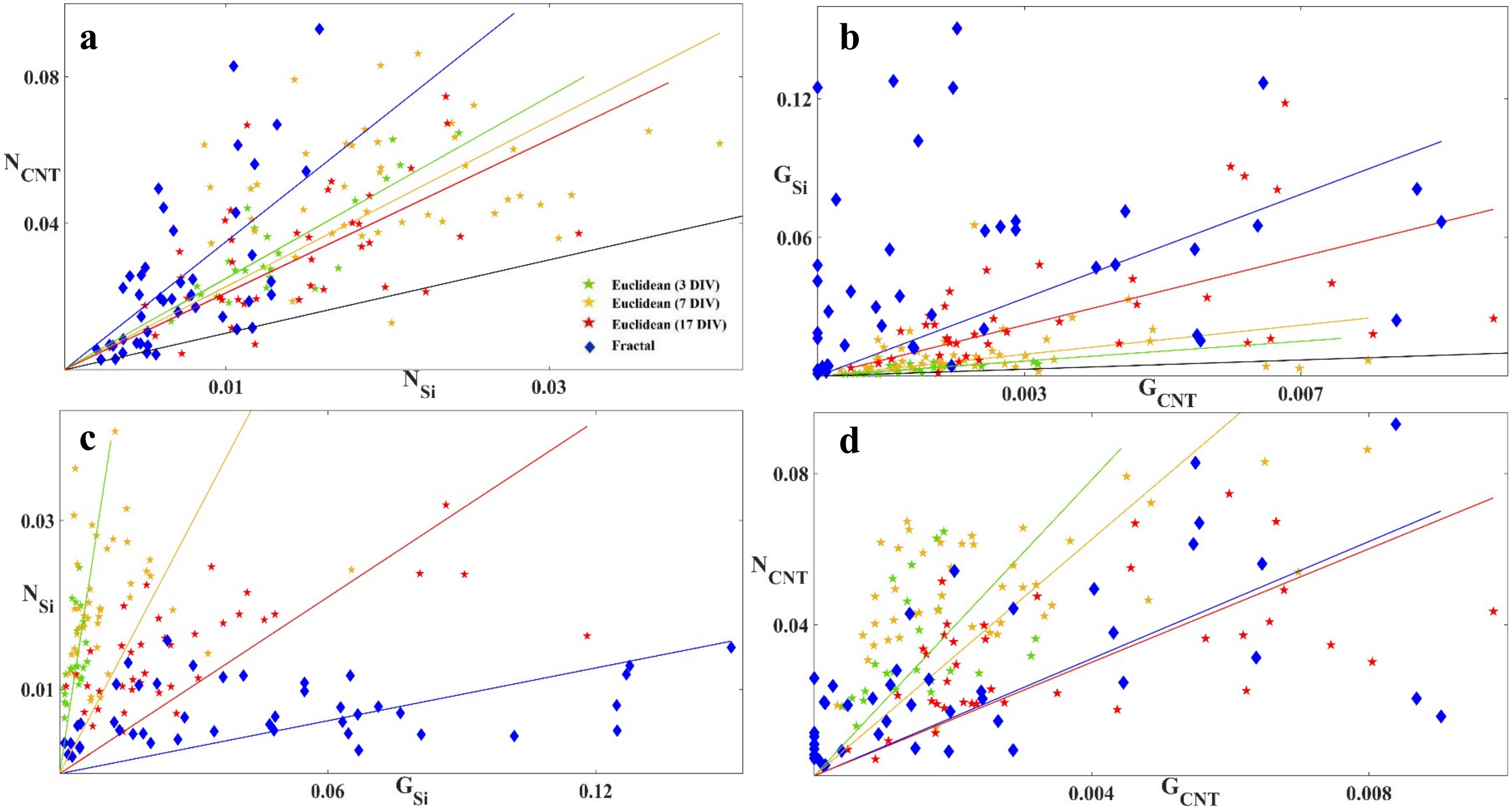

Figure 4-15. Time evolution of fractal and Euclidean samples. Scatterplots of a) N_{CNT} vs N_{Si}, b) G_{Si} vs G_{CNT}, c) N_{Si} vs G_{Si} and d) N_{CNT} vs G_{CNT} for the 3 DIV (green pentagram), 7 DIV (yellow pentagram), 17 DIV (red pentagram) Euclidean and fractal samples (blue diamonds). The Solid blue, green, yellow and red lines are linear fits that pass through 0 for the fractals, 3, 7 and 17 DIV Euclidean samples respectively. The solid black line in (a) and (b) are the herding lines.

N_{Si}, on the other hand, was much lower for the Si control samples than the fractal and Euclidean samples at all culture durations. At 17 DIV, the order in which N_{Si} increased between groups was reversed compared to G_{Si}, showing an inverse relation between the amount of glia and neuron processes on smooth surfaces and the direct effect of the existence and closeness of the edges of electrodes on the evolution of the neural networks.

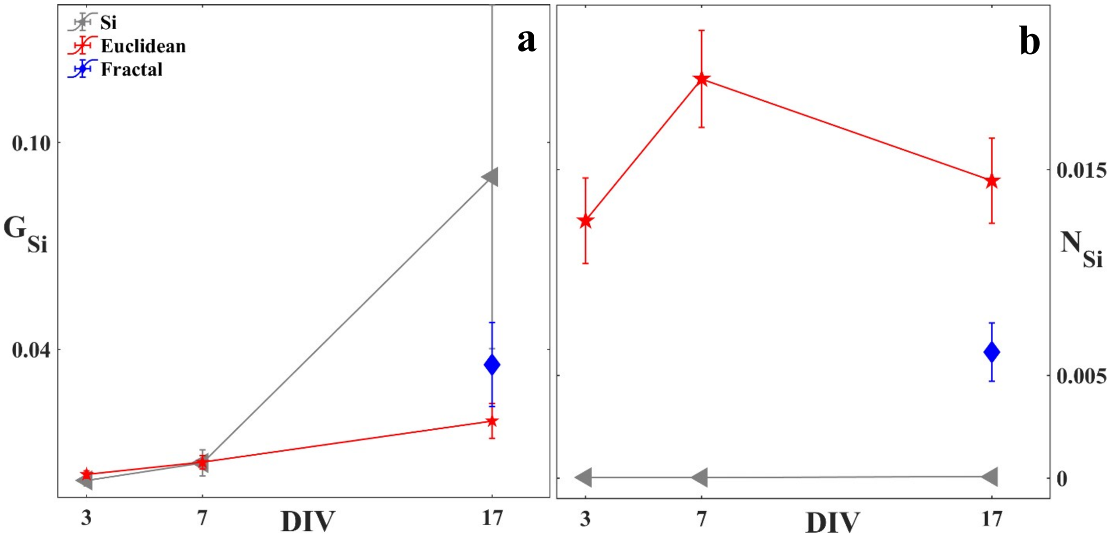

Figure 4-16. Comparison between Euclidean, fractal and Si control samples. a) G_{Si} and b) N_{Si} median trends vs DIV for Euclidean, fractal and control Si groups.

4-4. Conclusion

The inherent geometrical properties of fractals give them an advantage over Euclidean geometries. The large edge lengths of the electrodes intertwined with the multi-scaled interconnected smooth regions between the electrode branches creates a tortuous structure that provides a suitable scaffold for neurons to adhere to and grow processes on while supporting glial survival and proliferation inside the smooth regions in close proximity to the neurons.

The fractal dimension, D, and the number of iterations determine fractal properties such as total edge length, tortuosity, proximity of electrode branches to smooth surfaces and the distribution and scaling of those areas. These parameters directly impact the status of a neural network by affecting the degree of aggregation of the neurons into clusters and the pruning of processes connecting them. They also determine the freedom that glial cells would face while proliferating inside smooth regions.

Based on the data provided and due to the low number of samples, it was difficult to identify a particular fractal with a specific D or number of iterations as the winner. Theoretically though, it is known that fractals with high D and iterations support neuronal growth because they have larger edge lengths and more tortuous structures, but at the same time they inhibit glial proliferation since they lose the interconnected multi-scaled characteristic of the smooth Si regions. Low D and low iteration fractals act the opposite. They do not have enough edge length and they lose the proximity between the electrodes and the smooth regions because they have large interconnected areas between the branches. Therefore, they fail in supporting neuronal growth, but would potentially give glial cells enough space to proliferate. Choosing a mid to high D fractal with low number of iterations would create a balance between the two cases by supporting glial proliferation without restriction inside the gaps, having large enough proximity between the electrodes and the smooth regions to avoid the creation of desert areas and providing enough edge length to enhance neuron process outgrowth.

CHAPTER V

FUTURE WORK AND CONCLUSIONS

This chapter covers near future plans for comparing fractals to more Euclidean geometries and takes a brief look at the fractal resonance concept as well as the conclusions from this work and their application.

5-1. Comparison Between Fractal, Grid and Square CNT Electrodes

In the previous chapter, the advantages of fractal geometries over Euclidean rows in terms of interacting with retinal neurons and glial cells were discussed. It could be argued that other connected Euclidean geometries can compete with fractals depending on their geometrical properties. To further test the superiority of fractals over other Euclidean electrodes, they were theoretically compared with grids made of square chambers. For a grid with length X_L, width w_g, and number of chambers in a row, M, the following parameters were calculated: total length, total covering area, total edge length and length of a single chamber were calculated:

$$L_g(X_L, M) = X_L(M-1)\left(\frac{1+\sqrt{2}}{\sqrt{2}}\right)$$

$$A_g(X_L, M, w_g) = w_g[L_g - (M-1)^2 w_g]$$

$$E_g(X_L, M, w_g) = \frac{2A_g}{w_g} + 4(M-1)w_g$$

$$\mathrm{U}_g(X_L, M, w_g) = \frac{X_L - (M-1)w_g}{M}$$

The equations for the fractals were previously mentioned in Chapter II. The bounding and covering areas and line widths of the grids were set equal to those of the D = 2 fractals with 3, 4, 5 and 6 iterations. The step function in Figure 5-1 represents A_f vs number of iterations for D = 2 fractals. The horizontal red lines represent various grids with covering areas approximately equal to those of the specific fractals. The Si area of a single grid chamber, a_g, was then compared to the A_{min} of the fractals [Figure 5-1 inset]. For scaling reasons, the log of a_g and A_{min} were plotted for all four pairs of fractals and grids. All grids contained much larger unit chambers compared to their equivalent fractals with the same covering and bounding areas. As an example, a grid with bounding and covering areas equal to a 2-6 fractal (solid line in Figure 5-1) provided a unit chamber size that was ~9 times larger than the A_{min} for the 2-6 fractal. This ratio decreased as the number of iterations in the fractal decreased.

It is hypothesized that depending on the unit chamber size, the probability of having small-world or desert regions formed inside them could potentially increase. This then plays back into having fewer neuron clusters and processes close to the CNT edges and less communication between the Si and CNT neurons meaning decreasing the amount of neuron processes on CNT surfaces. As the size of the chamber decreases, the probability of having more chambers with no glial cells in them would increase. This could in turn affect survivability and synaptic efficacy of the neurons. In addition, the grid chambers are disconnected from each other. Glial proliferations inside one chamber cannot migrate to its neighbors and therefore empty chambers would remain as they were. Once again, it seems that the interconnectivity of the fractal electrode provides an advantage over the grid structures.

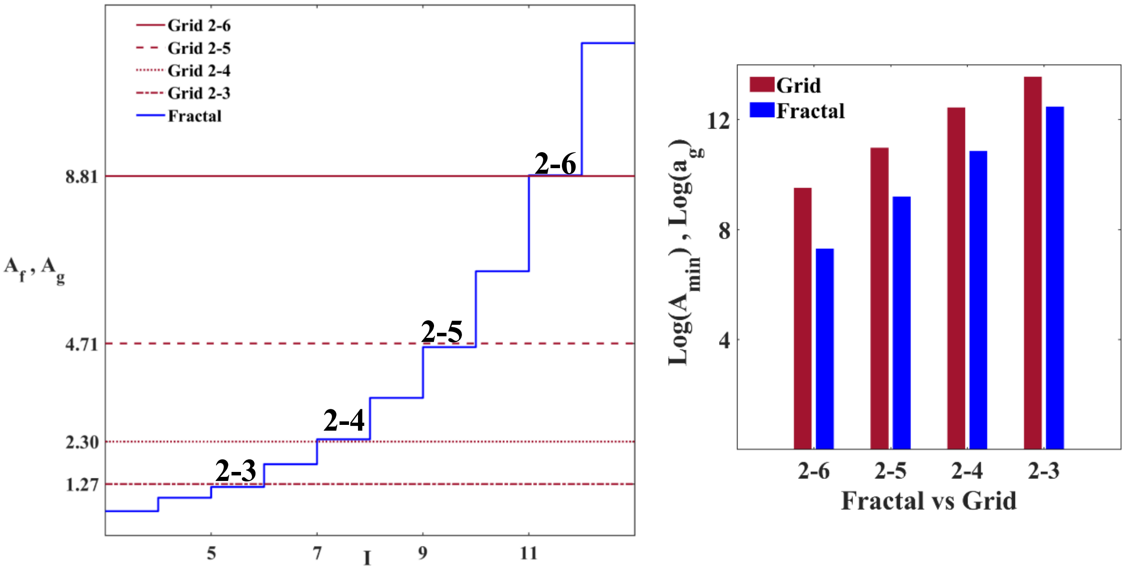

Figure 5-1. Covering area of D = 2 fractals plotted versus number of iterations. Covering areas of equivalent grids with different unit chamber sizes were plotted as lines for comparison. The inset shows a bar plot of the log of chamber areas of grids vs A_{min} of the fractals. In all instances, a_g is greater than A_{min}.

To test the predictions made so far, the 2-5 fractals were compared with grids and squares featuring the same covering areas. Grids were chosen as a connected Euclidean electrode that contains empty areas within them to house glial cells. It also provides a large number of edges to support neuronal growth. The width of the grid lines and fractal branches were set to be equal. The condition of having the same bounding area for the grid and fractal was not applied. Instead, the unit chamber length in the grid was set equal to d_v for 2-5 fractals (~ 61.2 µm). Thus, chamber areas in the grid were ~ 2.6 times smaller than the A_{min} of the 2-5 fractals. The grids had a length of 3507 µm and 43 chambers in a row. Squares were also included as typical electrode shapes used in commercial implants. CNT squares with length = 2144 µm were fabricated. The fabrication procedure, CNT synthesis and characterization were performed as described previously for the fractals in Chapter II.

Dissociated retinal cells were cultured for 7 and 17 DIV on all three electrode types. Fixing, immunohistochemistry and imaging were performed as previously described.

Preliminary visual observations of fluorescence microscopy images confirmed that the grid unit chambers restricted glial proliferation and prevented their migration to other areas within the electrode [Figure 5-2 a]. In contrast, glial proliferations in the smallest regions of the 2-5 fractals had the opportunity to proliferate into other areas through the interconnected space [Figure 5-2 b]. Glial cells on the CNT electrodes followed the shape of the electrode making 90° turns when reaching an intersection of CNTs [Figure 5-2 c]. Outside the grid boundaries, glial proliferations were prevalent and accompanied small-world neural networks. Processes from clusters that formed outside the patterned area extended and reached those on the electrodes [Figure 5-2 d]. At 7 DIV, large neuron clusters were formed inside the grid chambers, directly in contact with a sidewall in most cases. Neuron processes on the CNT electrodes followed the top and bottom edges of the electrode [Figure 5-2 e]. Based on observations, it was hard to determine if the grids outperformed the fractals in terms of supporting neurons on the CNT electrodes, but fractals definitely outperform grids in terms of herding glial cells onto Si surfaces.

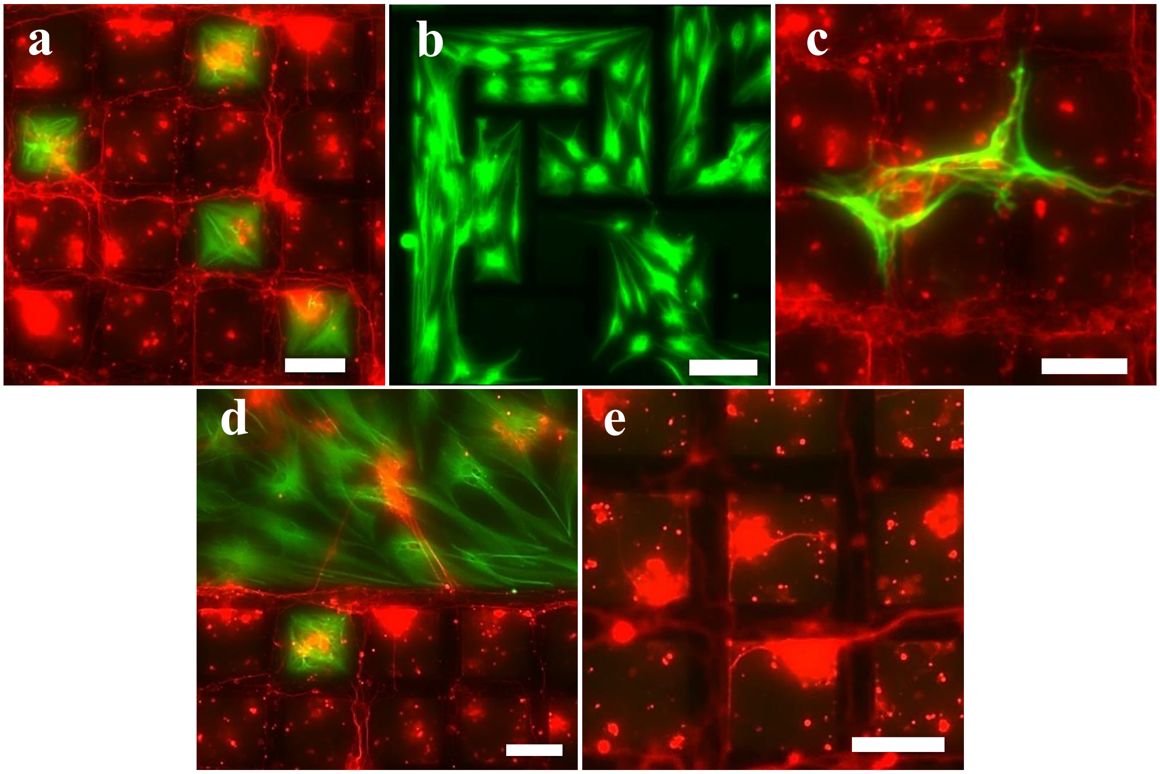

Figure 5-2. Examples of neuron and glial behavior on grid and fractal electrodes. a) Merged fluorescence images of glia and neurons on a grid at 17 DIV showing glial proliferations trapped inside grid chambers unable to bridge over CNT electrodes and neuron processes following CNT electrodes closely. b) Fluorescence image of glial proliferation inside the interconnected Si areas of a 2-5 fractal. c) Merged fluorescence images of glia and neurons on a grid at 17 DIV showing glial cells landing on CNT electrodes and following the electrode. d) Merged fluorescence images of glia and neurons on the side of a grid at 17 DIV showing processes from small-world network clusters outside the patterned region connecting to processes on CNT electrodes. e) Fluorescence image of neurons on a grid at 7 DIV showing processes on Si inside grid chambers following the bottom edges of the electrode. Scale bars in (a), (c), (d) and (e) are 50 µm. Scale bar in (b) is 100 µm.

Future work will focus on the quantitative comparisons of all three electrode types. Normalized total neuron process length and glial area for grids and squares will be calculated. The effect of culture time, the interconnected multi-scaled vs disconnected Si areas for the fractals versus grids, the edge length accessible to the neurons and the proximity between the Si and CNT areas on the behavior of retinal cells will be studied.

5-2. Conclusions

Current implants that interact with various parts of the nervous system face problems regarding efficient stimulation and recording. Many studies have focused on making improvements to implants by studying electrode materials with enhanced electrical and mechanical properties. Yet, there are unresolved issues, especially considering stimulating neurons, since the interactions between the biological tissue and the artificial surface of an electrode are not fully understood. One major problem that still stands when inserting an implant into the nervous system is the reactive gliosis response from glial cells towards any injury. Multiple studies have focused on finding chemical or mechanical solutions to hinder the glial response.

The work done in this thesis offers a potential answer to the glial scarring problem while focusing at the same time on improvement of the interactions between the electrode's surface and neuronal tissue. A system of materials with specific topographies and stiffnesses combined with micron-scale patterning was used to reduce glial cells reaction on the electrode surface and confine their proliferation to specific regions of the chip while encouraging neuronal adhesion and process elongation on the electrode surface. Euclidean and fractal electrodes made of vertically aligned carbon nanotube forests were synthesized on a Si substrate. The effect of geometric characteristics of the electrodes on mouse retinal cells in 3, 7 and 17 DIV cultures was studied.

Chapter II covered the design and fabrication procedure of both Euclidean and H-tree fractal samples. The synthesis and characterization of CNT forests, dissociated retinal cell cultures, immunohistochemistry, fluorescence and SEM microscopy, image processing and statistical analysis of the data was explained.

In Chapter III, a simple Euclidean geometry of rows of CNT forests separated by Si rows with varying widths was used to understand the fundamental behavior of retinal neurons and glia in contact with mechanical cues in the culture environment. It was discovered that the nanoroughness and lower rigidity of the CNT surfaces was ideal for neuronal survival, adhesion and process growth, but not a suitable medium for glial cells. Neuron processes followed the edges of the rows when reaching them. Glial cell proliferation was hindered on the CNT surfaces due to the lack of motility. On Si surfaces on the other hand, neurons survived through aggregation and clustering, and hence neural networks that were formed did not have as many processes as the ones on CNT surfaces. The smooth and rigid surface of Si enhanced glial proliferation. CNTs in these experiments did not go through any type of functionalization to make them hydrophilic and yet they were still able to support cell adhesion and survival. A simple system was created that successfully hindered glial growth on the surface of the electrode and improved neuronal growth while keeping glia inside Si areas in close contact with neurons on both surfaces.

Chapter IV focused on comparing Euclidean geometries with more complex fractal ones. The same general results were observed within the fractal geometries. They confined the glial scarring to their Si regions. It was discussed that the multi-scaled interconnected Si space had the ability to enhance glial proliferation to a level that was beyond reach of Euclidean geometries for the same culture times. It was also shown that the total edge length, tortuosity and average proximity of CNT electrodes to Si areas combined with the interconnectivity of the space play an important role in the formation, evolution and optimization status of the neural networks formed on the smooth Si surfaces. As a result, total neuron process length on the Si surfaces was affected. At the same time, interactions between neural networks formed on the Si and CNT surfaces was influenced by changing distances of the aggregated cells on the Si from the CNT electrodes.

In summary, fractal geometries combined with a textured material such as CNT forests appear to be a fundamental, permanent solution for preventing glial scars from covering the electrodes and improving neuron-electrode connectivity while keeping glia close to neurons on both surfaces. Results obtained here are not restricted to subretinal implant electrodes and their interactions with neurons and glia. They could be generalized to implants that interface with other parts of the central nervous system. However, experiments are needed to extend the findings presented here to other neuron types since various types of neurons and glia respond differently when exposed to the same environment.

The size of the electrodes suggested in this research were too large to function as a single pixel in retinal implants. Future work will focus on reducing the size of the electrodes to a 40 µm × 40 µm area in a multi-electrode array (MEA) structure. Exact and randomized H-tree fractals as well as traced patterns of neuron processes obtained from cultures on CNT squares will be used as potential patterns for CNT electrodes for *in vitro* and *in vivo* experiments. CNT squares will be used as controls. 40 µm × 40 µm FOVs of neurons previously cultured on uniform CNT mats for 17 DIV will be selected, their processes will be traced through the neuron process length algorithm. Using the box counting method, their fractal dimensions will be calculated. The chosen D values for H-tree fractals will match those of the statistical ones obtained from the traces. The total covering area of fractal electrodes and the thickness of the electrode lines will be the same. Applying the findings of the current research, the neurons are expected to attach to and follow the CNT branches while glial cells will accumulate and proliferate in the empty areas between the electrode pixels. No extra distance due to glial scarring is created between the electrode's surface and neurons. To further improve the connectivity between the neurons and these smaller electrodes, the fractal resonance hypothesis will be tested. As mentioned before neurons are statistical fractals. Various types of neurons have different fractal dimensions that are potentially related to their functionality and connectivity to other cells. The hypothesis of fractal resonance claims that by using a statistical fractal electrode with a D and geometric properties that mimic that of targeted neurons, the electrode will be treated as part of the biological system and its integration into the neuronal tissue would be further improved. Figure 5-3 shows schematic arrays of micro photodiode electrodes with exact and statistical fractal electrodes. Glial cells are shown to proliferate in the smooth areas between the pixels and neurons are connected to the fractal electrodes that match their fractal dimensions.

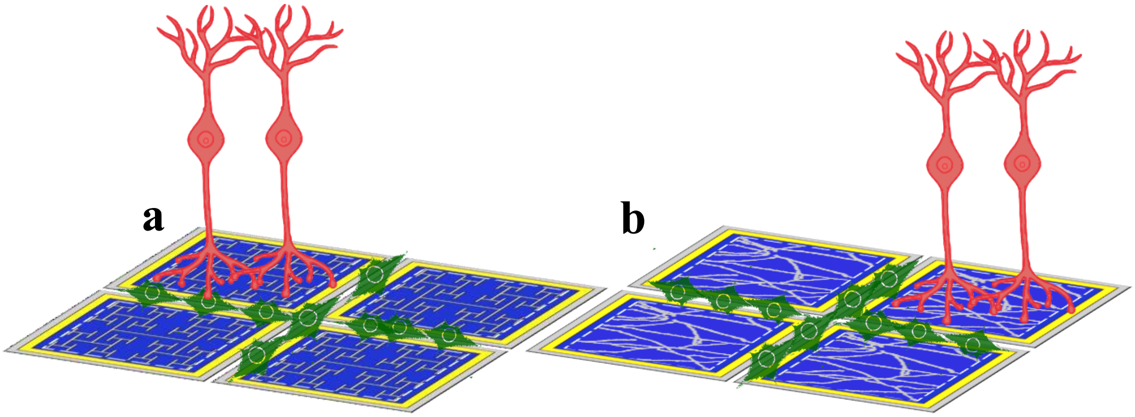

Figure 5-3. Fractal resonance and herding results applied to the design of implant electrodes. Micro photodiode arrays with a) exact H-tree and b) statistical fractal electrodes. Statistical fractals are actual traces of neuron processes cultured on uniform CNT mats. Each pixel is 40 µm × 40 µm. Conductive electrodes, the insulator and photodiode parts are shown in grey, yellow and blue respectively. The glial cells (green) accumulate the smooth areas between pixels and bipolar neurons (pink) adhere to and follow the fractal branches.

Finally, it should be mentioned that the *in vitro* cell cultures are simplified two-dimensional models of the three-dimensional biological tissue scaffolds. They are the necessary first step for studying complex behaviors of cells and their interactions with the environment. Future studies of explants and *in vivo* implants as three-dimensional structures will be more realistic representations of the interactions of neuronal tissue with artificial scaffolds.

REFERENCES CITED

1. The global burden of neurological disorders - The Lancet Neurology. https://www.thelancet.com/journals/laneur/article/PIIS1474-4422(19)30029-8/fulltext?rss=yes.

2. World Alzheimer Report 2018 - The state of the art of dementia research: New frontiers. *NEW Front.* 48.

3. Alzheimer's Facts and Figures Report | Alzheimer's Association. https://www.alz.org/alzheimers-dementia/facts-figures.

4. Parkinson's Foundation: Better Lives. Together. https://www.parkinson.org/Understanding-Parkinsons/Statistics.

5. 15 Limb Loss Statistics that May Surprise You - Access Prosthetics. https://accessprosthetics.com/15-limb-loss-statistics-may-surprise/.

6. Global Neurostimulation Devices Market | Industry Report, 2019-2026. https://www.grandviewresearch.com/industry-analysis/neurostimulation-devices-industry?utm_source=google&utm_medium=cpc&utm_campaign=AdWords_Neurostimulation-Devices Market_Type2_Healthcare&gclid=Cj0KCQiAuefvBRDXARIsAFEOQ9GR-7EUmZHc7x3EMslvb3iCfy-FiFobuG6OiNtd3T0o6ipAam_Kr9caAghoEALw_wcB.

7. Retinal Implant Market Size, Share | Industry Trends Report, 2018-2025. https://www.grandviewresearch.com/industry-analysis/retinal-implant-market.

8. Age-Related Macular Degeneration: Facts & Figures | BrightFocus Foundation. https://www.brightfocus.org/macular/article/age-related-macular-facts-figures.

9. Age-Related Macular Degeneration (AMD) Data and Statistics | National Eye Institute. https://www.nei.nih.gov/learn-about-eye-health/resources-for-health-educators/eye-health-data-and-statistics/age-related-macular-degeneration-amd-data-and-statistics.

10. Retinitis pigmentosa - The Lancet. https://www.thelancet.com/journals/lancet/article/PIIS0140-6736(06)69740-7/fulltext.

11. Antiangiogenic Drugs Are Stopping Neovascularization in Wet Macular Degeneration – Living Well With Low Vision. https://lowvision.preventblindness.org/2012/09/27/antiangiogenic-drugs-are-stopping-neovascularization-in-wet-macular-degeneration/.

12. Artificial vision: needs, functioning, and testing of a retinal electronic prosthesis. - PubMed - NCBI. https://www.ncbi.nlm.nih.gov/pubmed/19660665.

13. Retina Prosthesis - EyeWiki. https://eyewiki.aao.org/Retina_Prosthesis.

14. Argus II: the life-changing retinitis pigmentosa treatment. https://www.secondsight.com/discover-argus/.

15. Subretinal Visual Implant Alpha IMS – Clinical trial interim report - ScienceDirect. https://www.sciencedirect.com/science/article/pii/S0042698915000784.

16. PIXIUM VISION - Vision restoration systems, bionic vision , regaining vision. https://www.pixium-vision.com/en/clinical-trial/overview.

17. Subretinal electronic chips allow blind patients to read letters and combine them to words | Proceedings of the Royal Society B: Biological Sciences. https://royalsocietypublishing.org/doi/full/10.1098/rspb.2010.1747.

18. Photovoltaic retinal prosthesis: implant fabrication and performance. https://www.ncbi.nlm.nih.gov/pmc/articles/PMC3419261/.

19. Photovoltaic restoration of sight with high visual acuity | Nature Medicine. https://www.nature.com/articles/nm.3851.

20. Developments on the Boston 256-channel retinal implant. https://ieeexplore.ieee.org/document/6618445.

21. Diamond Devices for High Acuity Prosthetic Vision - Ahnood - 2017 - Advanced Biosystems - Wiley Online Library. https://onlinelibrary.wiley.com/doi/full/10.1002/adbi.201600003.

22. Kaneko, A. Physiological and morphological identification of horizontal, bipolar and amacrine cells in goldfish retina. *J. Physiol.* **207**, 623–633 (1970).

23. Retinal Neuron - an overview | ScienceDirect Topics. https://www.sciencedirect.com/topics/neuroscience/retinal-neuron.

24. GLIA: listening and talking to the synapse. - PubMed - NCBI. https://www.ncbi.nlm.nih.gov/pubmed/11256079.

25. Neuronal synchrony mediated by astrocytic glutamate through activation of extrasynaptic NMDA receptors. - PubMed - NCBI. https://www.ncbi.nlm.nih.gov/pubmed/15339653.

26. Hertz, L. & Zielke, H. R. Astrocytic control of glutamatergic activity: astrocytes as stars of the show. *Trends Neurosci.* **27**, 735–743 (2004).

27. Allen, N. J. & Barres, B. A. Signaling between glia and neurons: focus on synaptic plasticity. *Curr. Opin. Neurobiol.* **15**, 542–548 (2005).

28. Fields, R. D. & Stevens-Graham, B. New Insights into Neuron-Glia Communication. *Science* **298**, 556–562 (2002).

29. *Glial Neurobiology*. (John Wiley & Sons, Ltd, 2007). doi:10.1002/9780470517796.

30. O'Sullivan, M. L. *et al.* Astrocytes follow ganglion cell axons to establish an angiogenic template during retinal development. *Glia* **65**, 1697–1716 (2017).

31. Vecino, E., Rodriguez, F. D., Ruzafa, N., Pereiro, X. & Sharma, S. C. Glia-neuron interactions in the mammalian retina. *Prog. Retin. Eye Res.* **51**, 1–40 (2016).

32. Bringmann, A. *et al.* Müller cells in the healthy and diseased retina. *Prog. Retin. Eye Res.* **25**, 397–424 (2006).

33. Franze, K. *et al.* Müller cells are living optical fibers in the vertebrate retina. *Proc. Natl. Acad. Sci.* **104**, 8287–8292 (2007).

34. Ridet, J. L., Malhotra, S. K., Privat, A. & Gage, F. H. Reactive astrocytes: cellular and molecular cues to biological function. *Trends Neurosci.* **20**, 570–577 (1997).

35. Streit, W. J., Walter, S. A. & Pennell, N. A. Reactive microgliosis. *Prog. Neurobiol.* **57**, 563–581 (1999).

36. Unger, J. W. Glial reaction in aging and Alzheimer's disease. *Microsc. Res. Tech.* **43**, 24–28 (1998).

37. Dyer, M. A. & Cepko, C. L. Control of Müller glial cell proliferation and activation following retinal injury. *Nat. Neurosci.* **3**, 873–880 (2000).

38. Wilson, J. X. Antioxidant defense of the brain: a role for astrocytes. *Can. J. Physiol. Pharmacol.* **75**, 1149–1163 (1997).

39. Moshayedi, P. *et al.* The relationship between glial cell mechanosensitivity and foreign body reactions in the central nervous system. *Biomaterials* **35**, 3919–3925 (2014).

40. Biran, R., Martin, D. C. & Tresco, P. A. Neuronal cell loss accompanies the brain tissue response to chronically implanted silicon microelectrode arrays. *Exp. Neurol.* **195**, 115–126 (2005).

41. Eleftheriou, C. G. *et al.* Carbon nanotube electrodes for retinal implants: A study of structural and functional integration over time. *Biomaterials* **112**, 108–121 (2017).

42. Intracellular recording of action potentials by nanopillar electroporation | Nature Nanotechnology. https://www.nature.com/articles/nnano.2012.8.

43. Sorribas, H., Braun, D., Leder, L., Sonderegger, P. & Tiefenauer, L. Adhesion proteins for a tight neuron-electrode contact. *J. Neurosci. Methods* **104**, 133–141 (2001).

44. Shein, M. *et al.* Engineered neuronal circuits shaped and interfaced with carbon nanotube microelectrode arrays. *Biomed. Microdevices* **11**, 495–501 (2009).

45. Spatially controlled co-culture of neurons and glial cells - Yang - 2005 - Journal of Biomedical Materials Research Part A - Wiley Online Library. https://onlinelibrary.wiley.com/doi/epdf/10.1002/jbm.a.30509.

46. Kam, L., Shain, W., Turner, J. N. & Bizios, R. Correlation of astroglial cell function on micro-patterned surfaces with specific geometric parameters. *Biomaterials* **20**, 2343–2350 (1999).

47. Shi, M. *et al.* Glia co-culture with neurons in microfluidic platforms promotes the formation and stabilization of synaptic contacts. *Lab. Chip* **13**, 3008–3021 (2013).

48. Kidambi, S., Lee, I. & Chan, C. Primary Neuron/Astrocyte Co-Culture on Polyelectrolyte Multilayer Films: A Template for Studying Astrocyte-Mediated Oxidative Stress in Neurons. *Adv. Funct. Mater.* **18**, 294–301 (2008).

49. Delivopoulos, E. & Murray, A. F. Controlled Adhesion and Growth of Long Term Glial and Neuronal Cultures on Parylene-C. *PLOS ONE* **6**, e25411 (2011).

50. Zhong, Y. & Bellamkonda, R. V. Dexamethasone-coated neural probes elicit attenuated inflammatory response and neuronal loss compared to uncoated neural probes. *Brain Res.* **1148**, 15–27 (2007).

51. Kozai, T. D. Y. *et al.* Ultrasmall implantable composite microelectrodes with bioactive surfaces for chronic neural interfaces. *Nat. Mater.* **11**, 1065–1073 (2012).

52. Subbaroyan, J., Martin, D. C. & Kipke, D. R. A finite-element model of the mechanical effects of implantable microelectrodes in the cerebral cortex. *J. Neural Eng.* **2**, 103–113 (2005).

53. Minev, I. R. *et al.* Biomaterials. Electronic dura mater for long-term multimodal neural interfaces. *Science* **347**, 159–163 (2015).

54. Zhang, H. *et al.* Tissue-Compliant Neural Implants from Microfabricated Carbon Nanotube Multilayer Composite. *ACS Nano* **7**, 7619–7629 (2013).

55. Discher, D. E., Janmey, P. & Wang, Y.-L. Tissue cells feel and respond to the stiffness of their substrate. *Science* **310**, 1139–1143 (2005).

56. Lin, C.-M., Lee, Y.-T., Yeh, S.-R. & Fang, W. Flexible carbon nanotubes electrode for neural recording. *Biosens. Bioelectron.* **24**, 2791–2797 (2009).

57. Woerly, S., Doan, V. D., Sosa, N., de Vellis, J. & Espinosa-Jeffrey, A. Prevention of gliotic scar formation by NeuroGel allows partial endogenous repair of transected cat spinal cord. *J. Neurosci. Res.* **75**, 262–272 (2004).

58. Georges, P. C., Miller, W. J., Meaney, D. F., Sawyer, E. S. & Janmey, P. A. Matrices with Compliance Comparable to that of Brain Tissue Select Neuronal over Glial Growth in Mixed Cortical Cultures. *Biophys. J.* **90**, 3012–3018 (2006).

59. Butterwick, A. *et al.* Effect of shape and coating of a subretinal prosthesis on its integration with the retina. *Exp. Eye Res.* **88**, 22–29 (2009).

60. Piret, G., Perez, M.-T. & Prinz, C. N. Support of Neuronal Growth Over Glial Growth and Guidance of Optic Nerve Axons by Vertical Nanowire Arrays. *ACS Appl. Mater. Interfaces* **7**, 18944–18948 (2015).

61. He, J., Wang, X.-M., Spector, M. & Cui, F.-Z. Scaffolds for central nervous system tissue engineering. *Front. Mater. Sci.* **6**, 1–25 (2012).

62. Roach, P., Parker, T., Gadegaard, N. & Alexander, M. R. Surface strategies for control of neuronal cell adhesion: A review. *Surf. Sci. Rep.* **65**, 145–173 (2010).

63. Ahuja, A. K. *et al.* Factors Affecting Perceptual Threshold in Argus II Retinal Prosthesis Subjects. *Transl. Vis. Sci. Technol.* **2**, 1 (2013).

64. Mathieson, K. *et al.* Photovoltaic retinal prosthesis with high pixel density. *Nat. Photonics* **6**, 391–397 (2012).

65. Piret, G., Perez, M.-T. & Prinz, C. N. Neurite outgrowth and synaptophysin expression of postnatal CNS neurons on GaP nanowire arrays in long-term retinal cell culture. *Biomaterials* **34**, 875–887 (2013).

66. Harris, P. J. F. Carbon Nanotube Science: Synthesis, Properties and Applications. 315.

67. Charlier, J.-C., Blase, X. & Roche, S. Electronic and transport properties of nanotubes. *Rev. Mod. Phys.* **79**, 677–732 (2007).

68. Gao, G., Çagin, T. & Goddard, W. A. Energetics, structure, mechanical and vibrational properties of single-walled carbon nanotubes. *Nanotechnology* **9**, 184–191 (1998).

69. Hu, H., Ni, Y., Montana, V., Haddon, R. C. & Parpura, V. Chemically Functionalized Carbon Nanotubes as Substrates for Neuronal Growth. *Nano Lett.* **4**, 507–511 (2004).

70. Bareket-Keren, L. & Hanein, Y. Carbon nanotube-based multi electrode arrays for neuronal interfacing: progress and prospects. *Front. Neural Circuits* **6**, (2013).

71. Gabay, T. *et al.* Electro-chemical and biological properties of carbon nanotube based multi-electrode arrays. *Nanotechnology* **18**, 035201 (2007).

72. Cisnal, A., R Ihmig, F., Fraile, J.-C., Pérez-Turiel, J. & Muñoz-Martinez, V. Application of a Novel Measurement Setup for Characterization of Graphene Microelectrodes and a Comparative Study of Variables Influencing Charge Injection Limits of Implantable Microelectrodes. *Sensors* **19**, (2019).

73. Harris, A. R. *et al.* Correlation of the impedance and effective electrode area of doped PEDOT modified electrodes for brain–machine interfaces. *Analyst* **140**, 3164–3174 (2015).

74. Sorkin, R. *et al.* Process entanglement as a neuronal anchorage mechanism to rough surfaces. *Nanotechnology* **20**, 015101 (2009).

75. Ni, Y. *et al.* Chemically Functionalized Water Soluble Single-Walled Carbon Nanotubes Modulate Neurite Outgrowth. *J. Nanosci. Nanotechnol.* **5**, 1707–1712 (2005).

76. Shim, M., Shi Kam, N. W., Chen, R. J., Li, Y. & Dai, H. Functionalization of Carbon Nanotubes for Biocompatibility and Biomolecular Recognition. *Nano Lett.* **2**, 285–288 (2002).

77. Bianco, A., Kostarelos, K. & Prato, M. Making carbon nanotubes biocompatible and biodegradable. *Chem. Commun. Camb. Engl.* **47**, 10182–10188 (2011).

78. Bioavailability of Nickel in Single-Wall Carbon Nanotubes - Liu - 2007 - Advanced Materials - Wiley Online Library. https://onlinelibrary.wiley.com/doi/abs/10.1002/adma.200602696.

79. Tian, F., Cui, D., Schwarz, H., Estrada, G. G. & Kobayashi, H. Cytotoxicity of single-wall carbon nanotubes on human fibroblasts. *Toxicol. Vitro Int. J. Publ. Assoc. BIBRA* **20**, 1202–1212 (2006).

80. Yamashita, K. *et al.* Carbon nanotubes elicit DNA damage and inflammatory response relative to their size and shape. *Inflammation* **33**, 276–280 (2010).

81. Nagai, H. *et al.* Diameter and rigidity of multiwalled carbon nanotubes are critical factors in mesothelial injury and carcinogenesis. *Proc. Natl. Acad. Sci. U. S. A.* **108**, E1330-1338 (2011).

82. Wick, P. *et al.* The degree and kind of agglomeration affect carbon nanotube cytotoxicity. *Toxicol. Lett.* **168**, 121–131 (2007).

83. Belyanskaya, L. *et al.* Effects of carbon nanotubes on primary neurons and glial cells. *NeuroToxicology* **30**, 702–711 (2009).

84. Mattson, M. P., Haddon, R. C. & Rao, A. M. Molecular functionalization of carbon nanotubes and use as substrates for neuronal growth. *J. Mol. Neurosci.* **14**, 175–182 (2000).

85. Bronikowski, M. J. CVD growth of carbon nanotube bundle arrays. *Carbon* **44**, 2822–2832 (2006).

86. Yunyu, W., Li, B., Ho, P., Yao, Z. & Shi, L. Effect of supporting layer on growth of carbon nanotubes by thermal chemical vapor deposition. *Appl. Phys. Lett.* **89**, 183113–183113 (2006).

87. Zhao, B. *et al.* Exploring Advantages of Diverse Carbon Nanotube Forests with Tailored Structures Synthesized by Supergrowth from Engineered Catalysts. *ACS Nano* **3**, 108–114 (2009).

88. Hoffman-Kim, D., Mitchel, J. A. & Bellamkonda, R. V. Topography, Cell Response, and Nerve Regeneration. *Annu. Rev. Biomed. Eng.* **12**, 203–231 (2010).

89. Zhang, X. *et al.* Guided neurite growth on patterned carbon nanotubes. *Sens. Actuators B Chem.* **106**, 843–850 (2005).

90. David-Pur, M., Bareket-Keren, L., Beit-Yaakov, G., Raz-Prag, D. & Hanein, Y. All-carbon-nanotube flexible multi-electrode array for neuronal recording and stimulation. *Biomed. Microdevices* **16**, 43–53 (2014).

91. Chen, Y.-C. *et al.* An active, flexible carbon nanotube microelectrode array for recording electrocorticograms. *J. Neural Eng.* **8**, 034001 (2011).

92. Carbon nanotube coating improves neuronal recordings | Nature Nanotechnology. https://www.nature.com/articles/nnano.2008.174.

93. Zhou, H., Cheng, X., Rao, L., Li, T. & Duan, Y. Y. Poly(3,4-ethylenedioxythiophene)/multiwall carbon nanotube composite coatings for improving the stability of microelectrodes in neural prostheses applications. *Acta Biomater.* **9**, 6439–6449 (2013).

94. Fabbro, A., Bosi, S., Ballerini, L. & Prato, M. Carbon Nanotubes: Artificial Nanomaterials to Engineer Single Neurons and Neuronal Networks. *ACS Chem. Neurosci.* **3**, 611–618 (2012).

95. Voge, C. M. & Stegemann, J. Carbon nanotubes in neural interfacing applications. *J. Neural Eng.* **8**, 011001 (2011).

96. Roberts, M. J. *et al.* Growth of primary motor neurons on horizontally aligned carbon nanotube thin films and striped patterns. *J. Neural Eng.* **11**, 036013 (2014).

97. Nick, C., Yadav, S., Joshi, R., Thielemann, C. & Schneider, J. J. Growth and structural discrimination of cortical neurons on randomly oriented and vertically aligned dense carbon nanotube networks. *Beilstein J. Nanotechnol.* **5**, 1575–1579 (2014).

98. Liu, W. F. & Chen, C. S. Engineering biomaterials to control cell function. *Mater. Today* **8**, 28–35 (2005).

99. An atlas of nano-enabled neural interfaces | Nature Nanotechnology. https://www.nature.com/articles/s41565-019-0487-x.

100. Watterson, W. J., Montgomery, R. D. & Taylor, R. P. Fractal Electrodes as a Generic Interface for Stimulating Neurons. *Sci. Rep.* **7**, (2017).

101. Watterson, W. J., Montgomery, R. D. & Taylor, R. P. Modeling the Improved Visual Acuity Using Photodiode Based Retinal Implants Featuring Fractal Electrodes. *Front. Neurosci.* **12**, (2018).

102. Delzeit, L. *et al.* Multiwalled Carbon Nanotubes by Chemical Vapor Deposition Using Multilayered Metal Catalysts. *J. Phys. Chem. B* **106**, 5629–5635 (2002).

103. Bronikowski, M. J., Manohara, H. M. & Hunt, B. D. Growth of carbon nanotube bundle arrays on silicon surfaces. *J. Vac. Sci. Technol. Vac. Surf. Films* **24**, 1318–1322 (2006).

104. Xiang, M. Intrinsic control of mammalian retinogenesis. *Cell. Mol. Life Sci. CMLS* **70**, 2519–2532 (2013).

105. Sharma, R. K. & Netland, P. A. Early born lineage of retinal neurons express class III beta-tubulin isotype. *Brain Res.* **1176**, 11–17 (2007).

106. Wu, C., Schulte, J., Sepp, K. J., Littleton, J. T. & Hong, P. Automatic robust neurite detection and morphological analysis of neuronal cell cultures in high-content screening. *Neuroinformatics* **8**, 83–100 (2010).

107. Moore, S. W. & Sheetz, M. P. Biophysics of substrate interaction: influence on neural motility, differentiation and repair. *Dev. Neurobiol.* **71**, 1090–1101 (2011).

108. Khan, S. & Newaz, G. A comprehensive review of surface modification for neural cell adhesion and patterning. *J. Biomed. Mater. Res. A* **93A**, 1209–1224 (2010).

109. Sorkin, R. *et al.* Compact self-wiring in cultured neural networks. *J. Neural Eng.* **3**, 95–101 (2006).

110. Kim, M.-H., Park, M., Kang, K. & Choi, I. S. Neurons on nanometric topographies: insights into neuronal behaviors in vitro. *Biomater. Sci.* **2**, 148–155 (2013).

111. Mangione A, M. A. & Messina JC, B. L. Basic Research for Peripheral Neural Regeneration by CNTs, A Preliminary â€ œin vitroâ€ • Study. *J. Nanomedicine Nanotechnol.* **06**, (2015).

112. Fan, Y. W. *et al.* Culture of neural cells on silicon wafers with nano-scale surface topograph. *J. Neurosci. Methods* **120**, 17–23 (2002).

113. Brunetti, V. *et al.* Neurons sense nanoscale roughness with nanometer sensitivity. *Proc. Natl. Acad. Sci.* **107**, 6264–6269 (2010).

114. Flanagan, L. A., Ju, Y.-E., Marg, B., Osterfield, M. & Janmey, P. A. Neurite branching on deformable substrates. *Neuroreport* **13**, 2411–2415 (2002).

115. Koch, D., Rosoff, W. J., Jiang, J., Geller, H. M. & Urbach, J. S. Strength in the Periphery: Growth Cone Biomechanics and Substrate Rigidity Response in Peripheral and Central Nervous System Neurons. *Biophys. J.* **102**, 452–460 (2012).

116. Gabay, T. *et al.* Carbon nanotube based neuro-chip for engineering, recording and stimulation of cultured networks. in *The 13th International Conference on Solid-State Sensors, Actuators and Microsystems, 2005. Digest of Technical Papers. TRANSDUCERS '05.* vol. 2 1226-1229 Vol. 2 (2005).

117. Latora, V. & Marchiori, M. Economic small-world behavior in weighted networks. *Eur. Phys. J. B - Condens. Matter Complex Syst.* **32**, 249–263 (2003).

118. Achard, S. & Bullmore, E. Efficiency and cost of economical brain functional networks. *PLoS Comput. Biol.* **3**, e17 (2007).

119. Santos-Sierra, D. de *et al.* Emergence of Small-World Anatomical Networks in Self-Organizing Clustered Neuronal Cultures. *PLOS ONE* **9**, e85828 (2014).

120. Woiterski, L., Claudepierre, T., Luxenhofer, R., Jordan, R. & Käs, J. A. Stages of neuronal network formation. *New J. Phys.* **15**, 025029 (2013).

121. Anava, S., Greenbaum, A., Ben-Jacob, E., Hanein, Y. & Ayali, A. The Regulative Role of Neurite Mechanical Tension in Network Development. *Biophys. J.* **96**, 1661–70 (2009).

122. Liu, J. *et al.* Control of neuronal network organization by chemical surface functionalization of multi-walled carbon nanotube arrays. *Nanotechnology* **22**, 195101 (2011).

123. Luo, L. & O'Leary, D. D. M. Axon retraction and degeneration in development and disease. *Annu. Rev. Neurosci.* **28**, 127–156 (2005).

124. Shefi, O., Golding, I., Segev, R., Ben-Jacob, E. & Ayali, A. Morphological characterization of in vitro neuronal networks. *Phys. Rev. E* **66**, 021905 (2002).

125. Fan, Y. W. *et al.* Adhesion of neural cells on silicon wafer with nano-topographic surface. *Appl. Surf. Sci.* **187**, 313–318 (2002).

126. Ben-Jacob, E. & Hanein, Y. Carbon nanotube micro-electrodes for neuronal interfacing. *J. Mater. Chem.* **18**, 5181 (2008).

127. Chen, H. *et al.* Controlled growth and modification of vertically-aligned carbon nanotubes for multifunctional applications. *Mater. Sci. Eng. R Rep.* **70**, 63–91 (2010).

128. Machado, M. M., Lobo, A. O., Marciano, F. R., Corat, E. J. & Corat, M. A. F. Analysis of cellular adhesion on superhydrophobic and superhydrophilic vertically aligned carbon nanotube scaffolds. *Mater. Sci. Eng. C* **48**, 365–371 (2015).

129. Xie, C. *et al.* Noninvasive Neuron Pinning with Nanopillar Arrays. *Nano Lett.* **10**, 4020–4024 (2010).

130. Nichols, A. J., Carney, L. H. & Olson, E. C. Comparison of slow and fast neocortical neuron migration using a new in vitro model. *BMC Neurosci.* **9**, 50 (2008).

131. Persson, H. *et al.* Fibroblasts Cultured on Nanowires Exhibit Low Motility, Impaired Cell Division, and DNA Damage. *Small Weinh. Bergstr. Ger.* **9**, 4006–4016 (2013).

132. Textural guidance cues for controlling process outgrowth of mammalian neurons - Lab on a Chip (RSC Publishing). https://pubs.rsc.org/en/content/articlelanding/2009/LC/B803595D#!divAbstract.

133. Smeal, R. M., Rabbitt, R., Biran, R. & Tresco, P. A. Substrate Curvature Influences the Direction of Nerve Outgrowth. *Ann. Biomed. Eng.* **33**, 376–382 (2005).

134. Smeal, R. M. & Tresco, P. A. The influence of substrate curvature on neurite outgrowth is cell type dependent. *Exp. Neurol.* **213**, 281–292 (2008).

135. Turner, J. N. *et al.* Cerebral Astrocyte Response to Micromachined Silicon Implants. *Exp. Neurol.* **156**, 33–49 (1999).

136. Edell, D. J., Toi, V. V., McNeil, V. M. & Clark, L. D. Factors influencing the biocompatibility of insertable silicon microshafts in cerebral cortex. *IEEE Trans. Biomed. Eng.* **39**, 635–643 (1992).

137. McKenzie, J. L., Waid, M. C., Shi, R. & Webster, T. J. Decreased functions of astrocytes on carbon nanofiber materials. *Biomaterials* **25**, 1309–1317 (2004).

138. Gottipati, M. K., Kalinina, I., Bekyarova, E., Haddon, R. C. & Parpura, V. Chemically Functionalized Water-Soluble Single-Walled Carbon Nanotubes Modulate Morpho-Functional Characteristics of Astrocytes. *Nano Lett.* **12**, 4742–4747 (2012).

139. Bollmann, L. *et al.* Microglia mechanics: immune activation alters traction forces and durotaxis. *Front. Cell. Neurosci.* **9**, (2015).

140. Lu, Y.-B. *et al.* Viscoelastic properties of individual glial cells and neurons in the CNS. *Proc. Natl. Acad. Sci. U. S. A.* **103**, 17759–17764 (2006).

141. Moeendarbary, E. *et al.* The soft mechanical signature of glial scars in the central nervous system. *Nat. Commun.* **8**, (2017).

142. Hatten, M. E. & Mason, C. A. Mechanisms of glial-guided neuronal migration in vitro and in vivo. 11 (1990).

143. Ullian, E. M., Sapperstein, S. K., Christopherson, K. S. & Barres, B. A. Control of Synapse Number by Glia. *Science* **291**, 657–661 (2001).

144. Yang, Y. *et al.* Contribution of astrocytes to hippocampal long-term potentiation through release of d-serine. *Proc. Natl. Acad. Sci.* **100**, 15194–15199 (2003).

145. Piret, G., Perez, M.-T. & N. Prinz, C. Substrate porosity induces phenotypic alterations in retinal cells cultured on silicon nanowires. *RSC Adv.* **4**, 27888–27897 (2014).

146. Gautam, V. *et al.* Engineering Highly Interconnected Neuronal Networks on Nanowire Scaffolds. *Nano Lett.* (2017) doi:10.1021/acs.nanolett.6b05288.

147. Gabay, T., Jakobs, E., Ben-Jacob, E. & Hanein, Y. Engineered self-organization of neural networks using carbon nanotube clusters. *Phys. Stat. Mech. Its Appl.* **350**, 611–621 (2005).

148. Schaar, B. T. & McConnell, S. K. Cytoskeletal coordination during neuronal migration. *Proc. Natl. Acad. Sci.* **102**, 13652–13657 (2005).

149. Komuro, H. & Rakic, P. Modulation of neuronal migration by NMDA receptors. *Science* **260**, 95–97 (1993).

150. Edmondson, J. C. & Hatten, M. E. Glial-guided granule neuron migration in vitro: a high-resolution time-lapse video microscopic study. *J. Neurosci. Off. J. Soc. Neurosci.* **7**, 1928–1934 (1987).

151. Fishell, G. & Hatten, M. E. Astrotactin provides a receptor system for CNS neuronal migration. *Development* **113**, 755–765 (1991).